

6-8-2021

# Numerical Techniques and Simulations for Studying Various High Power Optical Fiber Amplifiers, Particularly for Ytterbium ( $\text{Yb}^{+3}$ ), and Thulium ( $\text{Tm}^{+3}$ ) Doped Fibers

Tathagata Goswami  
*Portland State University*

Follow this and additional works at: [https://pdxscholar.library.pdx.edu/open\\_access\\_etds](https://pdxscholar.library.pdx.edu/open_access_etds)



Part of the [Mathematics Commons](#)

Let us know how access to this document benefits you.

---

## Recommended Citation

Goswami, Tathagata, "Numerical Techniques and Simulations for Studying Various High Power Optical Fiber Amplifiers, Particularly for Ytterbium ( $\text{Yb}^{+3}$ ), and Thulium ( $\text{Tm}^{+3}$ ) Doped Fibers" (2021). *Dissertations and Theses*. Paper 5709.  
<https://doi.org/10.15760/etd.7581>

This Dissertation is brought to you for free and open access. It has been accepted for inclusion in Dissertations and Theses by an authorized administrator of PDXScholar. Please contact us if we can make this document more accessible: [pdxscholar@pdx.edu](mailto:pdxscholar@pdx.edu).

Numerical Techniques and Simulations for Studying Various High Power Optical Fiber  
Amplifiers, Particularly for Ytterbium ( $\text{Yb}^{+3}$ ), and Thulium ( $\text{Tm}^{+3}$ ) Doped Fibers

by

Tathagata Goswami

A dissertation submitted in partial fulfillment of the  
requirements for the degree of

Doctor of Philosophy  
in  
Mathematical Sciences

Dissertation Committee:  
Jay Gopalakrishnan, Chair  
Jacob Grosek  
Jeff Oval  
Panayot Vassilevski  
Erik Sanchez

Portland State University  
2021

© 2021 Tathagata Goswami

## Abstract

In this dissertation we present a simplified scalar numerical model, derived from Maxwell's field equations, for the fiber laser amplifier simulations. Maxwell's equations are reduced using a technique called Coupled Mode Theory (CMT).

The reduced model is made more efficient through a new scale model, referred to as an equivalent short fiber, which captures some of the essential characteristics of a longer fiber. The equivalent short fiber can be viewed as a fiber made using artificial (nonphysical) material properties that in some sense compensates for its reduced length. The computations can be accelerated by a factor approximately equal to the ratio of the original length to the reduced length of the equivalent fiber. Computations using models of two commercially available fibers – one doped with ytterbium, and the other with thulium-show the practical utility of the concept. Extensive numerical studies are conducted to assess when the equivalent short fiber model is useful and when it is not.

Fiber quantum defect heating is included in the model. We solve the heat equation coupled with our CMT equation to get the solution. Transverse Mode Instability (TMI) is observed in both ytterbium and thulium doped fibers. Various power thresholds are presented for TMI. Also, to find the root cause of TMI and to investigate how to mitigate this chaotic process, we have experimented with different refractive index gratings. A few gratings are presented with numerical results which show promises.

Finally this dissertation uses numerical simulations of a thulium-doped optical fiber amplifier to predict various performance characteristics such as peak temperatures, expected output powers and efficiencies, presence of Amplified Spontaneous Emission (ASE), et cetera. Single- and two-tone configurations are studied. In the latter case, the two laser sources are separated in frequency by the amount that corresponds to the peak Raman gain,

and a few seed ratios at various total seed powers are examined.

To reduce the excessive computational time and resources needed to simulate the CMT equations and also to study TMI efficiently after sufficient number of time-steps, the code is parallelized using both shared and distributed memory configurations. The techniques employed in this strategy give linear speedup as we increase the number of time-steps for a fixed number of nodes.

## Acknowledgments

Foremost, I would like to express my sincere gratitude to my advisor Dr. Jay Gopalakrishnan for the continuous support of my Ph.D study and research, for his patience, motivation, enthusiasm, and immense knowledge. His guidance helped me all throughout my research efforts. His knowledge of programming has inspired me greatly to learn and gain a deeper understanding of computer simulations. There were many times when I felt depressed or frustrated, it was his guidance and support that helped me to get back on the track every time.

I want to thank the members of my dissertation committee - not only for their time and extreme patience, but for their intellectual contributions to my development as a mathematician. I am indebted to Dr. Jacob Grosek, who shaped my thinking as a researcher, assisted me in debugging my code many times, and also patiently taught me and helped me improve my writing as a researcher. Without his expertise about the domain this dissertation would not have been achievable. I want to thank Dr. Jeff Ovall for helping me understand Finite Element Analysis on a profound level. I want to thank Dr. Panayot Vassilevski and Dr. Erik Sanchez for their timely suggestions with kindness and enthusiasm in the journey of my doctoral study.

I want to thank Dr. Leszek Demkowicz at the university of Texas, Austin and his students and collaborators: Dr. Stefan Henneking, Dr. Sriram Nagaraj, and Dr. Socratis Petrides for their work and contribution on our fiber laser amplifier research.

I want to thank my old and present colleagues: Dr. Paulina Sepulveda, Dr. Ammar Harb, Dow Drake, Ben Parker, and Pieter Vandenberghe for helping me in teaching undergraduate courses, assisting me with coding difficulties, providing useful input on my dissertation, and most importantly supporting me during my low times, throughout my

doctoral career. In particular I want to thank Dow Drake for assisting me to understand and learn many concepts of programming. His immense patience while explaining me difficult concepts step by step has really rewired my brain as a programmer. I also want to thank all of them for their enormous contribution to the programming of fiber amplifier simulations.

Finally, I deeply thank my parents, for their unconditional trust, timely encouragement, and endless patience. It was their love that raised me up again when I got weary. Despite the long distance between us, they were always there for me with their love and encouragement.

This work was partially supported by the Air Force Office of Scientific Research (AFOSR) grants no. FA9550-19-1-0237 and 18RDCOR018.

# Table of Contents

<b>Abstract</b>	<b>i</b>
<b>Acknowledgements</b>	<b>iii</b>
<b>List of Tables</b>	<b>viii</b>
<b>List of Figures</b>	<b>x</b>
<b>List of Acronyms</b>	<b>xv</b>
<b>List of Abbreviations</b>	<b>xvi</b>
<b>List of Symbols</b>	<b>xvii</b>
<b>1 Introduction</b>	<b>1</b>
1.1 Brief History of Optical Fiber Amplifiers . . . . .	3
1.2 Light Guiding and Amplification Mechanism . . . . .	7
1.3 Motivation and Objectives . . . . .	9
1.4 Dissertation Outline . . . . .	10
<b>2 Numerical modeling of light propagation</b>	<b>12</b>
2.1 Maxwell's equations . . . . .	12
2.1.1 Maxwell's wave equation . . . . .	15
2.2 Electric Polarizations ( $\mathbf{P}_\ell$ ) and Propagation Model . . . . .	16
2.2.1 Background Polarization . . . . .	18
2.2.2 Linear Loss . . . . .	18
2.2.3 Active Laser Gain . . . . .	19



2.2.3.1	Tm-dopant ion dynamics . . . . .	19
2.2.3.2	Yb-dopant ion dynamics . . . . .	23
2.2.4	Passive Raman Gain . . . . .	24
2.2.5	Thermal Effects . . . . .	25
2.2.6	Propagation Model . . . . .	28
2.3	Coupled Mode Theory . . . . .	29
2.3.1	Optical fiber Modes . . . . .	30
2.3.1.1	Mode Equations, and its exact solutions . . . . .	30
2.3.1.2	Mode Cutoff and number of Modes . . . . .	34
2.3.1.3	Hybrid Mode Theory . . . . .	35
2.3.2	CMT ansatz . . . . .	37
2.3.3	Governing Equations . . . . .	37
2.3.3.1	Governing equation for pump light . . . . .	38
2.3.3.2	Full CMT model . . . . .	40
2.4	Two-tone, Raman hybrid laser amplifier model . . . . .	41
2.4.1	Governing equations . . . . .	42
<b>3</b>	<b>Fiber amplifier code implementation and parallelization</b>	<b>46</b>
3.1	Distributed Memory Parallelization . . . . .	47
3.1.1	General Attributes . . . . .	47
3.1.2	Advantages and disadvantages . . . . .	48
3.1.3	Hybrid Distributed-Shared memory parallelism . . . . .	48
3.2	Parallelism Utilization . . . . .	49
3.2.1	Amdahl's law and Strong scaling . . . . .	50
3.2.2	Gustafson's law and weak scaling . . . . .	51
3.3	Scaling of the fiber amplifier model . . . . .	53
3.3.1	Time independent simulation . . . . .	56
3.3.2	Time dependent simulation . . . . .	58
3.3.2.1	Speed-up of the fiber amplifier model . . . . .	59
3.3.2.2	Features of the fiber amplifier model . . . . .	60
<b>4</b>	<b>Tm- and Yb-doped Equivalent Fibers</b>	<b>68</b>
4.1	A Scaled Fiber Amplifier Model . . . . .	69




4.2	Simulation Results . . . . .	76
4.2.1	Computation With Physical Fiber . . . . .	76
4.3	Computations of Equivalent Fibers . . . . .	79
4.3.1	Realizing the equivalent short fiber for the Tm-doped case . . . . .	80
4.3.2	Realizing the equivalent short fiber for the Yb-doped case . . . . .	83
4.3.3	Increase of error with respect to some parameters . . . . .	85
<b>5</b>	<b>TMI in Tm-doped Single-, and Two-tone Fibers</b>	<b>88</b>
5.1	Transverse Mode Instability . . . . .	88
5.2	Numerical formulation of the heat equation . . . . .	89
5.3	Simulation of the onset of TMI . . . . .	90
<b>6</b>	<b>Tm-doped Two-tone fibers and ASE</b>	<b>94</b>
6.1	Simulation results . . . . .	100
6.1.1	Thermally dependent mode-bend-loss . . . . .	101
6.1.2	Single- and two-tone output signal power comparisons . . . . .	102
6.1.3	Effects of the dopant concentration . . . . .	103
6.1.4	Onset of ASE based on seed conditions . . . . .	113
<b>7</b>	<b>Propagation of light in the presence of artificial gratings</b>	<b>117</b>
7.1	Long Period Bragg Grating and Mode Coupling . . . . .	118
7.2	An autonomous system for Power . . . . .	119
7.3	Simulation Results . . . . .	126
7.4	Experiments with different grating functions and perturbation regions . . .	127
<b>8</b>	<b>Conclusion</b>	<b>137</b>
8.1	Future work . . . . .	138
	<b>References</b>	<b>140</b>

## List of Tables

4.1	Parameters used in Yb-doped fiber simulation . . . . .	77
4.2	Parameters used in Tm-doped fiber simulation . . . . .	77
5.1	Launched pump power TMI threshold interval, with its corresponding output signal amplification efficiencies and maximum total ASE power range, for a straight Tm-doped amplifier with a 2110 nm signal wavelength, and a 100 W total seed power. . . . .	91
6.1	Important emission ranges of different rare-earth ions [50] . . . . .	94
7.1	Mode coupling due to symmetric perturbation . . . . .	128
7.2	Mode coupling due to asymmetric perturbation . . . . .	129
7.3	The change in FM output power is shown as the value of $\delta n_0$ changes, the grating region here is an annulus . . . . .	132
7.4	The table shows at what distance the fundamental mode reaches its maximum power as we change the initial input seed power injected in the FM, the grating region here is an annulus . . . . .	132
7.5	The change in FM output power is shown as the value of $\delta n_0$ changes, the grating region here is the complement of an elliptic region inside the fibercore	134
7.6	The table shows at what distance the fundamental mode reaches its maximum power as we change the initial input seed power injected in the FM, the grating region here is the complement of an elliptic region inside the fibercore . . . . .	134


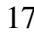

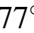


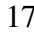

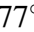

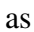


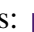
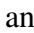

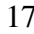

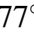


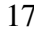



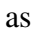

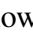
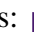
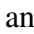
7.7 The table shows at what distance the fundamental mode reaches its maximum power as we change the initial input seed power injected in the FM, the grating region here is the complement of a hyperbolic region inside the fibercore . . . . . 135

## List of Figures

1.1	A typical step-index transverse cross-section, not drawn to scale . . . . .	2
1.2	Step-index Fiber, drawn to scale . . . . .	4
1.3	Light guidance in a step-index optical fiber . . . . .	8
2.1	Simplified diagram of Tm energy levels . . . . .	20
2.2	A simplified diagram of two Yb energy levels . . . . .	22
2.3	Experimentally measured normalized bulk Raman gain coefficient (normalized $g_R$ ) as the offset frequency between any two operating wavelengths inside the fiber [40]. . . . .	24
2.4	A visual representation of basic configuration of an optical fiber amplifier .	29
2.5	Transverse intensity profiles of different fiber modes . . . . .	36
3.1	Amdahl's Law . . . . .	51
3.2	Gustafson's Law . . . . .	52
3.3	$N$ equally divided parts of the fiber . . . . .	55
3.4	Each part of the fiber assigned to an individual node . . . . .	55
3.5	Flow of solving the governing problem using $N$ nodes . . . . .	56
3.6	Initial stage of the simulation,  : the associated job is done,  : the associated job has all the resources to start the job but did not start yet,  : the associated job is waiting for resources to start, solid arrow shows the flow of the ODE solver, dashed arrow shows the flow of the heat solver, and the dash-dotted arrow shows the MPI interactions. . . . .	63

3.7	Simulation continuation, —: the associated job is done, —: the associated job has all the resources to start the job but did not start yet, —: the associated job is waiting for resources to start, solid arrow shows the flow of the ODE solver, dashed arrow shows the flow of the heat solver, and the dash-dotted arrow shows the MPI interactions. . . . .	64
3.8	Simulation continuation, —: the associated job is done, —: the associated job has all the resources to start the job but did not start yet, —: the associated job is waiting for resources to start, solid arrow shows the flow of the ODE solver, dashed arrow shows the flow of the heat solver, and the dash-dotted arrow shows the MPI interactions. . . . .	65
3.9	Simulation continuation, —: the associated job is done, —: the associated job has all the resources to start the job but did not start yet, —: the associated job is waiting for resources to start, solid arrow shows the flow of the ODE solver, dashed arrow shows the flow of the heat solver, and the dash-dotted arrow shows the MPI interactions. . . . .	66
3.10	Last step of the simulation, —: the associated job is done, —: the associated job has all the resources to start the job but did not start yet, —: the associated job is waiting for resources to start, solid arrow shows the flow of the ODE solver, dashed arrow shows the flow of the heat solver, and the dash-dotted arrow shows the MPI interactions. . . . .	67
4.1	The simulated distribution of powers along the Tm-doped (left) and the Yb-doped (right) fiber amplifier. The pump power $P_p$ and the signal power $P_s$ , as defined in (4.5), are shown. The black dotted line plots $P_s + P_p$ . . . . .	79
4.2	A Tm-doped amplifier comparison between a real-length fiber and its equivalent short counterpart. The upper left panel shows the case where the input signal power was wholly contained in the $LP_{01}$ mode, while the upper right panel shows the case where it was equally distributed between the two modes- $LP_{01}$ , and $LP_{11}$ . The power difference along the fiber is plotted below for each case. The oscillations we see is due to the phase difference between the physical and equivalent fiber model. . . . .	82

4.3	A Yb-doped amplifier comparison between a real-length fiber and its equivalent short counterpart. The upper left panel shows the case where the input signal power was wholly contained in the LP <sub>01</sub> mode, while the upper right panel shows the case where it was equally distributed between the four modes-LP <sub>01</sub> , LP <sub>21</sub> , and LP <sub>02</sub> . The power difference along the fiber is plotted below for each case. The oscillations we see is due to the phase difference between the physical and equivalent fiber model. . . . .	84
4.4	Maximal relative power differences between a 10 m long real fiber and equivalent short fibers of various lengths $\tilde{L}$ , for various initial pump powers $P_p^0$ . The Tm case is shown on the left and Yb case on the right. . . . .	86
5.1	Change in temperature at the fiber center comparison between single- and two-tone coiled fiber at 2110 nm after 0.01 seconds. . . . .	92
5.2	Output signal mode powers for the single-tone configured straight amplifier operating either below (a) or above (b) the TMI threshold. . . . .	93
5.3	Output signal mode powers for the two-tone configured straight amplifier (1:1 seed ratio) operating either below (a) or above (b) the TMI threshold. . . . .	93
6.1	Absorption and emission cross-section spectra of the thulium dopant [65]. . . . .	95
6.2	Atmospheric transmittance in the wavelength range 2.1-2.2 $\mu\text{m}$ . . . . .	96
6.3	Simplified thulium electron energy level diagram. . . . .	97
6.4	Mode-bend-loss behavior under three different temperature profiles. . . . .	101
6.5	Straight amplifier performances. The color-codes indicate a range of ratios of output tone power to output signal power: — <0.01, — 0.01-0.1, — 0.1-0.5, — 0.5-1.0, and — >1.0. . . . .	104
6.6	Coiled amplifier performances. The color-codes indicate a range of ratios of output tone power to output signal power: — <0.01, — 0.01-0.1, — 0.1-0.5, — 0.5-1.0, and — >1.0. . . . .	105

6.7	Peak change in temperature in a straight fiber throughout the core region as a function of launched pump power and dopant concentration. Color bands relate to peak change in temperature ranges (core region) as follows:  17°C-77°C,  77°C-177°C,  177°C-277°C,  277°C-377°C, and  377°C-427°C. . . . .	107
6.8	Peak change in temperature in a straight fiber throughout the core region as a function of launched pump power and dopant concentration. Color bands relate to peak change in temperature ranges (core region) as follows:  17°C-77°C,  77°C-177°C,  177°C-277°C,  277°C-377°C, and  377°C-427°C. . . . .	108
6.9	Peak change in temperature in a straight fiber throughout the polymer coating region as a function of launched pump power and dopant concentration. Color bands relate to peak change in temperature ranges (polymer region) as follows:  17°C-27°C,  27°C-47°C,  47°C-57°C,  57°C-67°C, and  67°C-77°C. . . . .	109
6.10	Peak change in temperature in a coiled fiber throughout the core region as a function of launched pump power and dopant concentration. Color bands relate to peak change in temperature ranges (core region) as follows:  17°C-77°C,  77°C-177°C,  177°C-277°C,  277°C-377°C, and  377°C-427°C. . . . .	110
6.11	Peak change in temperature in a coiled fiber throughout the core region as a function of launched pump power and dopant concentration. Color bands relate to peak change in temperature ranges (core region) as follows:  17°C-77°C,  77°C-177°C,  177°C-277°C,  277°C-377°C, and  377°C-427°C. . . . .	111
6.12	Peak change in temperature in a coiled fiber throughout the polymer coating region as a function of launched pump power and dopant concentration. Color bands relate to peak change in temperature ranges (polymer region) as follows:  17°C-27°C,  27°C-47°C,  47°C-57°C,  57°C-67°C, and  67°C-77°C. . . . .	112
6.13	Maximum total ASE power levels in a straight fiber. . . . .	114
6.14	ASE power levels when $\lambda_s = 2110$ nm using total seed power of 5 W. . . . .	116



6.15	ASE power levels when $\lambda_s = 2133$ nm using total seed power of 5 W. . . .	116
6.16	ASE power levels when $\lambda_s = 2170$ nm using total seed power of 5 W. . . .	116
7.1	Initial seed equally distributed. . . . .	133
7.2	FM receives 60% of the seed power. . . . .	133
7.3	Initial seed equally distributed. . . . .	135
7.4	FM receives 60% of the seed power. . . . .	135
7.5	Initial seed equally distributed. . . . .	136
7.6	FM receives 60% of the seed power. . . . .	136

## List of Acronyms

ASE	Amplified Spontaneous Emission.
CMT	Coupled Mode Theory.
FWM	Four-wave mixing.
LED	Light Emitting Diode.
LMA	Large Mode Area.
LP	Linearly Polarized.
NA	Numerical Aperture.
ODE	Ordinary Differential Equation.
SBS	Stimulated Brillouin Scattering.
SRS	Stimulated Raman scattering.
TE	Transverse Electric.
TM	Transverse Magnetic.
TMI	Transverse Mode Instability.

## List of Abbreviations

2d	two dimensions.
3d	three dimensions.
EMF	Electromotive force.
FBG	Fiber bragg grating.
FM	Fundamental mode.
HOM	Higher order mode.
HPC	High performance computing.
LPBG	Long period bragg grating.
MPI	Message passing interface.
OFA	Optical fiber amplifier.
SOA	Semiconductor optical amplifier.

## List of Symbols

Notation	Description
$A_l^s$	Amplitude of the $m^{\text{th}}$ mode corresponding to the signal wavelength.
$A_m^\ell$	Amplitude of the $m^{\text{th}}$ mode corresponding to $\ell^{\text{th}}$ wavelength.
$C$	Specific heat of the glass.
$I_j$	Irradiance of the $j^{\text{th}}$ wavelength.
$K_{lm}^\ell$	Coupling coefficient between the $l^{\text{th}}$ , and the $m^{\text{th}}$ modes, corresponding to the $\ell^{\text{th}}$ wavelength.
$M_\ell$	Total number of guided modes present in the fiber corresponding to the $\ell^{\text{th}}$ wavelength.
$P_l^s(z)$	Power contained in $l^{\text{th}}$ guided mode at longitudinal point $z$ of the signal wavelength.
$Q$	Total heat-load inside the fiber.
$U$	$x$ -component of the Scalar electric field.
$U_\ell$	$x$ -component of the Scalar electric field of the $\ell^{\text{th}}$ wavelength.
$\mathcal{B}$	Magnetic flux density.
$\mathcal{D}$	Electric flux density.
$\Delta$	$\frac{\partial^2}{\partial x^2} + \frac{\partial^2}{\partial y^2} + \frac{\partial^2}{\partial z^2}$ .
$\Delta_{xy}$	$\left( \frac{\partial^2}{\partial x^2} + \frac{\partial^2}{\partial y^2} \right)$ .
$\mathcal{E}$	Real, time-harmonic electric field vector.
$\mathcal{H}$	Real, time-harmonic magnetic field vector.
$\mathcal{J}$	Current density vector.
$\mathcal{M}$	Magnetic polarization.
$\Omega_z$	Fiber cross-sectional region at longitudinal point 'z'.
$\mathcal{P}$	Electric polarization.

Notation	Description
$\Upsilon_\ell^R$	Raman coupling coefficient.
$\alpha_\ell$	Attenuation constant of the fiber.
$\mathbf{E}$	Complex, time-independent electric field vector.
$\mathbf{H}$	Complex, time-independent magnetic field vector.
$\mathbf{P}$	Electric polarization corresponding to $\mathbf{E}$ .
$\beta_m^\ell$	Propagation constant of the $m^{\text{th}}$ mode corresponding to $\ell^{\text{th}}$ wavelength.
$\cdot$	Dot product.
$\chi_\ell^{(j)}$	$j^{\text{th}}$ order electric susceptibility of the $\ell^{\text{th}}$ .
$\partial\Omega_z$	Boundary of $\Omega_z$ .
$\delta n$	Perturbation in refractive index profile.
$\ell$	Wavelength index in fiber.
$\epsilon_0$	Vacuum permittivity.
$\gamma_\ell$	Laser gain function of the $\ell^{\text{th}}$ wavelength.
$\hat{e}_x$	Unit vector in $x$ -direction.
$\hbar$	Planck's constant.
$i$	$= \sqrt{-1}$ .
$\int_{\Omega_z}$	Integration over the fiber cross-sectional area $\Omega_z$ .
$\kappa_{\text{therm}}$	Thermal conductivity of the glass.
$\lambda_\ell$	$\ell$ indexed wavelength in the fiber.
$\Im(\cdot)$	Imaginary part of a complex number.
$\mathcal{M}$	Total number of wavelengths present in the fiber.
$\Re(\cdot)$	Real part of a complex number.
$\mu_0$	Vacuum permeability.
$\nabla$	$\left(\frac{\partial}{\partial x}, \frac{\partial}{\partial y}, \frac{\partial}{\partial z}\right)$ .
$\omega$	Angular frequency.
$\pi$	Pi.
$\rho_0$	Density of glass.
$\rho_f$	Charge density.

<b>Notation</b>	<b>Description</b>
$\times$	Cross product.
$\Phi_m^\ell$	Transverse mode profile of the $m^{\text{th}}$ mode corresponding to $\ell^{\text{th}}$ wavelength.
$c$	Speed of light.
$g_\ell$	Active laser gain function of the $\ell^{\text{th}}$ wavelength.
$g_R$	Bulk Raman gain coefficient.
$k$	Angular wavenumber.
$k_0$	Angular wavenumber of vacuum.
$k_\ell$	Angular wavenumber of the $\ell^{\text{th}}$ wavelength.
$m_\ell$	The perturbation to the Helmholtz system corresponding to the $\ell^{\text{th}}$ wavelength.
$n_{\text{clad}}$	Cladding refractive index of an optical fiber.
$n_{\text{core}}$	Core refractive index of an optical fiber.
$r, \phi, z$	Cylindrical coordinates where $r$ denotes the radial distance from the fiber center, $\phi$ denote the azimuthal angle, and $z$ denote the longitudinal distance.
$r_{\text{clad}}$	Cladding-radius of an optical fiber.
$r_{\text{core}}$	Core-radius of an optical fiber.
$u_\ell$	Radial component of $U_\ell$ .
$x, y, z$	Cartesian coordinates where $z$ denotes the longitudinal axis of the fiber and $x$ , and $y$ accounts for the transverse axes.

## **Chapter 1**

### **Introduction**

The term optical fiber refers to very thin, flexible, highly transparent strands/pipes of dielectric material that carry light along their lengths. In 1970, Corning Glass researchers Robert Maurer, Donald Keck, and Peter Schultz invented fiber optic wire or "Optical Wave-guide Fibers" capable of carrying 65000 times more information than copper wire, through which information carried by a pattern of light waves could be decoded at the other end of the fiber even a thousand miles away [39]. Since then the field of optical fibers has grown so much that the modern day life is pretty much surrounded by fiber optics applications. Starting from telecommunication and networking, optical fibers are now used in healthcare, TV broadcasting, information technology, industrial applications, sound navigation and ranging (SONAR), et cetera [2]. Typically, long optical fibers may need to have their signal light amplified else intrinsic losses may reduce the signal to be unusable. An optical amplifier is a device that amplifies an optical signal directly, without the need to first convert it to an electrical signal. They operate on the same principle as a LASER (Light Amplification by Stimulated Emission of Radiation). The main difference between these two is that there is no feedback mechanism to induce a resonant wavelength in an optical amplifier as there is for a LASER device. American physicist Gordon Gould coined the word LASER

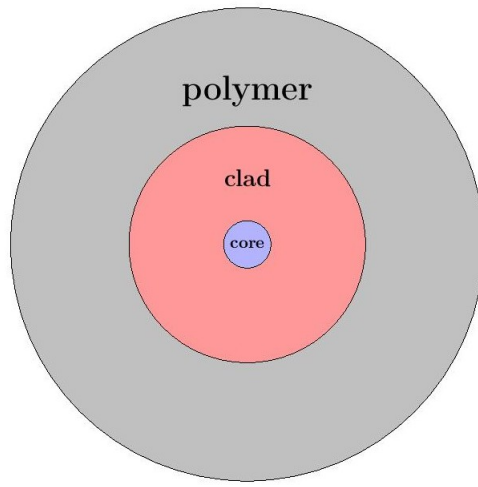


Figure 1.1: A typical step-index transverse cross-section, not drawn to scale

and patented optically pumped and discharge excited laser amplifiers [21, 20]. In modern times, LASER has been adopted as its own word that may refer to either laser light (i.e. coherent light) or a laser device (i.e. a device that makes laser light). Gould also has major contributions on laser uses and fiber optic communications that help power the internet of today. Fiber amplifiers are used in welding, cutting, remote sensing, surgery, anti-missile weapons, particle acceleration, confinement of nuclear fusion et cetera. For laser amplifiers, rare-earth ion doped step-index fibers are good candidates. Figure 1.1 shows the cross-section of a typical step-index fiber. It has a core region (or gain region) doped by rare earth ions like ytterbium ( $\text{Yb}^{3+}$ ), thulium ( $\text{Tm}^{3+}$ ), erbium ( $\text{Er}^{3+}$ ), etc, surrounded by a transparent cladding medium with slightly lower refractive index than core, which helps keep the light inside the core region, and finally a polymer coating around the cladding to protect the fiber.



## 1.1 Brief History of Optical Fiber Amplifiers

The importance of fiber amplifiers in enabling our current world of long-distance fiber optics and submarine telecommunications cannot be overlooked [10]. High power fiber amplifiers also have many other uses, for example, as defensive speed-of-light weapons. High output powers have been achieved by solid-state optical fiber laser amplifiers [31]. Numerical modeling of these optical devices has also been effectively used by many [32, 47, 59, 66]. The transmission loss of the light passing through optical fiber is very small, less than 0.2 dB per km with a light wavelength in the 1550 nm band. However, when the length of the optical fiber is a distance as long as 10 km or 100 km, that transmission loss cannot be ignored. When the light (signal) propagating along a long-distance optical fiber becomes extremely weak, it is necessary to amplify the light using an optical amplifier.

An optical amplifier amplifies light as it is without converting the optical signal to an electrical signal, and is an extremely important device that supports the long-distance optical communication networks of today. There are two main categories of optical amplifiers, optical fiber amplifiers or OFAs, and semiconductor optical amplifiers or SOAs. This dissertation mainly focuses on step-index OFAs. The most common types of optical amplifiers include Erbium doped fiber amplifier or EDFA, Ytterbium doped fiber amplifier or YDFA, Raman fiber amplifier or RFA, et cetera.

Erbium-doped fiber amplifiers are by far the most widely used fiber amplifiers in the context of long-range optical fiber communications; they can efficiently amplify light in the 1.5  $\mu\text{m}$  wavelength region because telecommunication fibers have minimal loss in this wavelength regime. A fiber amplifier distinguishes itself from a mere fiber waveguide by having small amounts of rare-earth dopants (e.g., lanthanide metals), which are chosen to provide laser amplification via stimulated emission when it is optically pumped with other

light injected into the fiber. The basic structure of an EDFA consists of a length of Erbium-doped fiber, a pump laser, and a wavelength division multiplexer (WDM) combiner. The WDM combiner is for combining the signal and pump wavelength so that they can propagate simultaneously through the amplifier. In the case of an EDFA, the optical signal, such as a 1550 nm signal, enters the amplifier from the input. The 1550 nm signal is combined with a 980 nm pump laser with a WDM device. The signal and the pump laser pass through a length of fiber doped with Erbium ions as EDFA uses the erbium-doped fiber as an optical amplification medium. The 1550 nm signal is amplified through interaction with the doping Erbium ions. This action amplifies a weak optical signal to a higher power, effecting a boost in the signal strength. The EDFA was first demonstrated by Professor David N Payne and his team at Southampton University (UK) [41], later investigated in [49, 43].

The core region of a step-index optical fiber amplifier is usually very small compared to its surrounding cladding region. Figure 1.2 shows an example of a step-index fiber amplifier

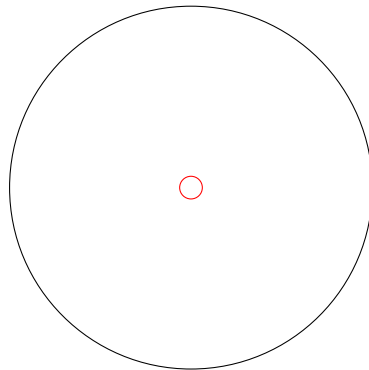


Figure 1.2: Step-index Fiber, drawn to scale

cross-section, drawn to scale. The core region is shown using the red circle at the center. Due to the very small core area, initially most of the optical fibers, as the power contained is increased, the power density became high enough to induce non-linear effects and/or fiber damage. In order to reduce the power density while maintaining the same amount of

power, the fibers are fabricated with larger core mode areas. For many applications, one still wants near-single mode operation, which can, in part, be accomplished by simultaneously reducing the core numerical aperture or Numerical Aperture (NA) of the fiber (within the limits of what can be fabricated realistically). This core NA of a fiber is defined as the sine of the largest angle an incident ray can have for total internal reflection in the core. This reduction of power density means that higher powers can be handled before non-linear effects occur. Hence it is desirable to use optical fibers with particularly large effective mode areas or Large Mode Area (LMA) fibers - often still with near single-mode guidance. Fibers with larger core diameters usually support more than just one single guided mode, namely the fundamental mode. Such fibers are usually called LMA fibers and/or few-mode fibers. Due to the reduced optical intensities, such fibers effectively have lower non-linear power thresholds and a higher damage threshold, which makes them more suitable for any application that requires handling higher power levels. Whereas standard single-mode fibers have an effective mode area below  $100 \mu\text{m}^2$ , LMA fibers reach values of hundreds or even thousands of  $\mu\text{m}^2$ . For a large mode area, one requires a large fiber core. However, large-core fibers do not necessarily have large modes, if they are strongly multi-mode; at least the fundamental mode area may then be much smaller than the core area [50, 37].

Fiber laser systems are usually insensitive to changes in the environment. Their efficiency in term of energy use is comparatively higher and their maintenance cost comparatively lower than other alternatives available currently. Also, the countless applications it has today have made it one of the most discussed and hot topic in the laser community. As we have discussed earlier, the core of a fiber laser amplifier is very small (usually of order  $10^{-5}$  m) compared to its length (usually in the neighborhood of 10 m ). This distinction favors the non-linear effects in the core of the fiber that can significantly degrade the signal

quality. As researchers achieved higher powers in fiber amplifiers, they were inhibited by optical nonlinearities (especially stimulated Brillouin scattering). In order to suppress the optical nonlinearities they started using fibers with larger core sizes (LMA fibers), which reduced the irradiance by spreading the power out over a larger area. However, a larger core contains more dopant, which absorbs the pump light faster, allowing for shorter fibers that deposit more heat per unit length. This impacted the average and the peak power of a fiber laser system significantly. Consequently, with power the heat-load of the system also increased which resulted the onset of thermal effects in active fibers. Transverse mode instability or TMI is one of the major manifestations of these thermal effects [33].

In the context of OFAs, LMA fibers are of great interest since they permit greater light amplification per unit length and help mitigate the onset of other detrimental optical nonlinearities. Unfortunately, they are also more susceptible to the transverse mode instability (TMI). The TMI is characterized by a rapid and chaotic exchange of power between the guided core modes both along the fiber and in time. This energy exchange is driven by a thermally-induced refractive index grating that naturally forms during the operation of the fiber amplifier. We believe that numerical modeling is essential for investigating TMI and other non-linearities like active laser gain during propagation, thermal load with time, etc, that arise inside fiber amplifiers. The current difficulty in using numerical models is the excessive memory requirements that force away the computation from laptops and workstations and onto supercomputers with parallelization to distribute the memory: indeed any numerical technique used must be able to solve for the electromagnetic field within a long fiber a vast number of times. Given the great computational burden of capturing length scales as small as  $10\ \mu\text{m}$ , and time scales as small as  $10\ \mu\text{sec}$  (for the thermal problem), techniques that further accelerate the numerical simulations have the potential to signifi-

cantly enhance the ability for computer modeling to inform experimental designs and configurations in a timely manner. There are other, even more reduced-physics TMI modeling approaches out there [61, 60], but they compromise the accuracy and predictability of the resulting model. We feel that the CMT approach offers the right balance of maintaining important physical processes, while still making justifiable approximations for the fiber amplifier problem. It is thus the intent of this dissertation to contribute such an acceleration technique by developing a scaled model.

## **1.2 Light Guiding and Amplification Mechanism**

Step-index fibers work on the principle of total internal reflection. Light reaching the interface boundary at a particular angle between two materials is reflected such that it never leaves the first material. In the case of fiber optics, light is reflected from the optical fiber core-cladding interface in such a way that it propagates down the core of the fiber. This can be explained by a brief discussion of Snell's law of refraction and law of reflection, and a physical quantity known as index of bottom material. According to Snell's law, the light will be bent from its original path to a larger angle in the second material. As the incoming, or incident angle increases, so does the refracted angle. For the properly chosen materials, the incident angle can be increased to the point that the ray is refracted at 90 degrees and never escapes the first medium. The equation can be solved to give the incoming, or incident, angle which will result in a refracted angle of 90 degrees. Light hitting the boundary or interface at angles greater than or equal to this value, as measured from the unit normal of the interface, would never pass into the second material, but would rather undergo total internal reflection. Now change the model slightly so that the higher index material is sandwiched between two lower index layers (see Figure 1.3. Light enters the higher index

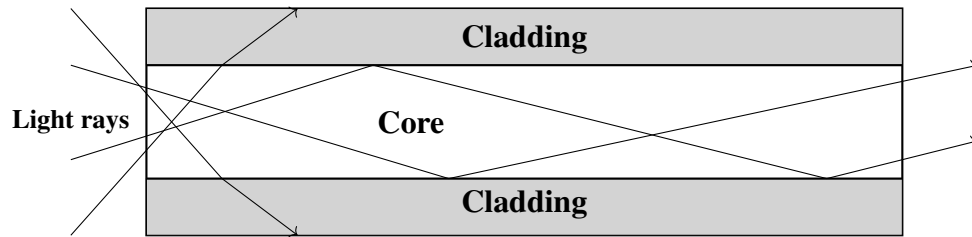


Figure 1.3: Light guidance in a step-index optical fiber

material, hits the upper interface and is reflected downward, then hits the second interface and is reflected back upward, and so on. Like a marble bouncing off rails, light will make its way down the waveguide as shown in Figure 1.3. Light introduced to the fiber at the critical angle will be guided in the inner (higher index) material by total internal reflection, and propagate down the fiber.

Though some propagating light may experience absorption or scattering due to interactions with the fiber medium, these loss processes are almost always negligible for the applications that we'll be exploring later in this dissertation.

Laser light amplification is achieved by stealing energy from another source of light, called the pump light, converting it into more of the signal (laser) light. Pump light is usually incoherent (or at least less coherent). This energy exchange between the pump light and the signal light is mediated through the active dopant in the fiber core region (e.g., a lanthanide metal). The active dopant naturally absorbs the pump light, but is then forced to emit that absorbed energy as laser light, coherent with the signal light, through a process known as stimulated emission (also called laser gain). If the fiber amplifier was not seeded with a coherent laser signal, or if this seed was too weak, then much of the absorbed energy from the pump light would be spontaneously emitted in all directions and over a variety of wavelengths incoherently. It is possible for spontaneous emission to become trapped

(guided) in the core region, and then later amplified by this same process, thus becoming amplified spontaneous emission (ASE), which is usually undesirable.

### **1.3 Motivation and Objectives**

Simulation of full length fibers remains cumbersome and far from being routine. This is because of the long simulation times and the large computational resources required. Simulations using the full Maxwell system are too expensive [27] since there are millions of wavelengths within any realistically long fiber. An example, consider the full Maxwell simulation of Raman gain attempted in [48]: more than five million degrees of freedom was needed to simulate an extremely short fiber containing 80 wavelengths (less than 0.0001 m). Although a full Maxwell model of a realistically long (10 m) fiber can be written out, its numerical solution is beyond the reach of today's simulation capabilities. The main objective of this dissertation is provide the field with a scaled model which uses less numerical resources and also computationally inexpensive. The ability of solid-state fiber laser amplifiers to deliver high output power has been exploited and studied over the last few decades [31]. "Scale models" are ubiquitous in fields such as fluid dynamics. They are physical or numerical models that preserve some of the important properties of an object being modeled while not preserving the original dimensions of the object. One area of investigation has been to formulate and study a miniature scale model of an optical fiber laser amplifier. Our scale model reduces fiber length to increase computational efficiency. While unable to preserve all properties of the original electromagnetic solution, our numerical scale model is able to approximately replicate the original fiber's power distribution, as we shall see in later sections. After this introductory section, we will begin by describing a simplified model of beam propagation in fibers. This model will then be used to derive,

justify, and verify the scale model.

So, the primary objectives of my Ph.D. research are as follows,

- Re-create the AFRL's CMT TMI fiber model, but with a finite element discretization for the transverse domain, allowing this new model to better investigate fibers with complex boundaries in their transverse domain. Write new thermal solver within this model appropriate for the FE discretization.
- Include further model improvements that will make it feasible to use the model on a local workstation rather than a full supercomputer.
- Develop, justify, and verify the fiber scale model called the equivalent short fiber. Compare results with more complete CMT TMI fiber model.
- Apply the model to realistic high-power fiber laser amplifier problems. Include physics for Yb-doped or Tm-doped gain media, Raman gain, multi-tone seeding configurations, ASE effects, thermal lensing, and a basic (over-simplified) inclusion of fiber coiling effects.
- Study the exchange of energy between core guided modes (akin to the TMI phenomenon) by introducing artificial refractive index gratings in the fiber.

#### **1.4 Dissertation Outline**

Following is an outline of this dissertation,

- In chapter 2 the mathematical model of the wave propagation problem is discussed in detail. It also introduces modes of step-index optical fibers, different electric polarizations, and the numerical methods used.



- Chapter 3 gives details about our amplifier code implementations and the distributed memory parallelization techniques used in the code.
- In chapter 4 we discuss a new scale model, referred to as an equivalent short fiber, which captures some of the essential characteristics of a longer fiber using significantly less computational resources.
- Chapter 5 introduces transverse mode instability and presents results regarding TMI thresholds.
- Chapter 6 presents numerical simulations of a thulium-doped optical fiber amplifier to predict various performance characteristics such as peak temperatures, expected output powers and efficiencies, presence of amplified spontaneous emission (ASE) in single- and multi-tone optical fiber configurations.
- Finally, in chapter 7 we show experiments with Bragg grating and some artificial refractive index gratings applied to different regions in the fiber core.

## **Chapter 2**

### **Numerical modeling of light propagation**

James Clerk Maxwell (1831–1879) is regarded as the greatest theoretical physicist of the nineteenth-century. Although he died young, Maxwell not only formulated a complete electromagnetic theory, represented by Maxwell's equations, he also developed the kinetic theory of gases and made significant contributions to the understanding of color vision and the nature of Saturn's rings. Maxwell brought together all the work that had been done by brilliant physicists such as Oersted, Coulomb, Gauss, and Faraday, and added his own insights to develop the overarching theory of electromagnetism. He had developed a theory that explained the relationship between electricity and magnetism, and correctly predicted that visible light consists of electromagnetic waves.

#### **2.1 Maxwell's equations**

Like all electromagnetic phenomena, light propagation through optical fibers is governed by Maxwell's equations. The Maxwell's equations are a set of fundamental relationships which govern how electric and magnetic fields interact. The equations also explain their relationship to charge and current. They form the backbone of much of modern electrical and telecommunication technology and are often quoted as being the most important

equations of all time. The equations consist of a set of four - Gauss's Electric Field Law, Gauss's Magnetic Field Law, Faraday's Law and the Ampere Maxwell Law. The system can be written as follows,

$$\nabla \times \mathcal{E} = -\frac{\partial \mathcal{B}}{\partial t}, \quad (\text{Faraday's law}) \quad (2.1a)$$

$$\nabla \times \mathcal{H} = \mathcal{J} + \frac{\partial \mathcal{D}}{\partial t}, \quad (\text{Ampere Maxwell law}) \quad (2.1b)$$

$$\nabla \cdot \mathcal{D} = \rho_f, \quad (\text{Gauss's law for electric field}) \quad (2.1c)$$

$$\nabla \cdot \mathcal{B} = 0, \quad (\text{Gauss's law for magnetism}) \quad (2.1d)$$

where  $\mathcal{E}$  and  $\mathcal{H}$  are electric and magnetic field vectors respectively and  $t$  denotes time.  $\mathcal{D}$  and  $\mathcal{B}$  are corresponding electric and magnetic flux densities. The current density vector  $\mathcal{J}$  and the charge density  $\rho_f$  represent the sources for the electromagnetic field.  $\nabla$  denotes the divergence vector  $\left(\frac{\partial}{\partial x}, \frac{\partial}{\partial y}, \frac{\partial}{\partial z}\right)$ . Also, the flux densities  $\mathcal{D}$  and  $\mathcal{B}$  which arise in response to the electric and magnetic fields  $\mathcal{E}$  and  $\mathcal{H}$  propagating inside the medium, are related by,

$$\mathcal{D} = \varepsilon_0 \mathcal{E} + \mathcal{P},$$

$$\mathcal{B} = \mu_0 \mathcal{H} + \mathcal{M},$$

where  $\varepsilon_0$  is the vacuum permittivity and  $\mu_0$  is the vacuum permeability.  $\mathcal{P}$  and  $\mathcal{M}$  are the induced electric and magnetic polarizations. We use the usual Cartesian coordinate system, where the  $z$ -direction is the longitudinal direction of the fiber and the fiber cross-section is represented by the  $xy$ -plane.

Gauss's law (equation (2.1c)) describes the relation between an electric charge and the electric field it produces. This is often pictured in terms of electric field lines originating

from positive charges and terminating on negative charges, and indicating the direction of the electric field at each point in space. For magnetism (equation (2.1d)) it states that the magnetic field flux through any closed surface is zero. Any magnetic field line entering the region enclosed by the surface must also leave it. No magnetic monopoles, where magnetic field lines would terminate, are known to exist. Faraday's law (equation (2.1a)) says that a changing magnetic field induces an electromotive force (EMF) and, hence, an electric field. The direction of the EMF opposes the change. This third of Maxwell's equations is Faraday's law of induction and includes Lenz's law. The electric field from a changing magnetic field has field lines that form closed loops, without any beginning or end. Finally, magnetic fields are generated by moving charges or by changing electric fields. This fourth of Maxwell's equations, encompasses Ampère's law and adds another source of magnetic fields (equation (2.1b), namely changing electric fields.

Media like optical fibers are non-magnetic and free of free charges, which makes the quantities  $\mathcal{M} = 0$ ,  $\mathcal{J} = 0$ , and  $\rho_f = 0$ . Also, we get  $\mathcal{B} = \mu_0 \mathcal{H}$ . Hence equation (2.1) can be re-written as,

$$\nabla \times \mathcal{E} = -\mu_0 \frac{\partial \mathcal{H}}{\partial t}, \quad (\text{Faraday's law}) \quad (2.3a)$$

$$\nabla \times \mathcal{H} = \varepsilon_0 \frac{\partial \mathcal{E}}{\partial t} + \frac{\partial \mathcal{P}}{\partial t}, \quad (\text{Ampere Maxwell law}) \quad (2.3b)$$

$$\nabla \cdot \mathcal{D} = 0, \quad (\text{Gauss's law for electric field}) \quad (2.3c)$$

$$\nabla \cdot \mathcal{B} = 0. \quad (\text{Gauss's law for magnetism}) \quad (2.3d)$$

Now, solving equation (2.3) for a 3d, 10 meter long optical fiber, which is the usual length of a physical fiber amplifier, requires a lot of computational resources and is very time consuming. The following sub-section attempts to simplify equation (2.3) by using some

standard assumptions from optical physics.

### 2.1.1 Maxwell's wave equation

The analysis of Maxwell's equations can be greatly simplified by assuming the fields to be time harmonic, or sinusoidal. A method called the phasor technique [36], often used by electrical engineers, is used here. We assume that the electric field  $\mathcal{E}$  and the magnetic field  $\mathcal{H}$  are time harmonic signals of frequency  $\omega$  as follows

$$\begin{aligned}\mathcal{E}(x, y, z, t) &= \Re\left[\mathbf{E}(x, y, z)e^{i\omega t}\right], \\ \mathcal{H}(x, y, z, t) &= \Re\left[\mathbf{H}(x, y, z)e^{i\omega t}\right],\end{aligned}$$

where  $\Re(\cdot)$  denotes the real part of the field.  $\mathbf{E}$  and  $\mathbf{H}$  respectively denote the complex electric and magnetic field. The variables  $x, y, z$  denote the usual Cartesian coordinates;  $e$ , and  $i$  respectively denote the math exponential and the complex imaginary number  $\sqrt{-1}$ . Hence, the field equations (2.3a) and (2.3b) can be written as

$$\nabla \times \mathbf{E} = -\mu_0 \frac{\partial \mathbf{H}}{\partial t}, \quad (2.5a)$$

$$\nabla \times \mathbf{H} = \varepsilon_0 \frac{\partial \mathbf{E}}{\partial t} + \frac{\partial \mathbf{P}}{\partial t}. \quad (2.5b)$$

Both the fields  $\mathbf{E}$  and  $\mathbf{H}$  are assumed to satisfy Maxwell's equation independently, but are coupled through the corresponding electric polarization term  $\mathbf{P}$ . Finally, after eliminating the magnetic field term  $\mathbf{H}$  from equation (2.5), we have,

$$\nabla \times \nabla \times \mathbf{E} - \omega^2 \varepsilon_0 \mu_0 \mathbf{E} = \omega^2 \mu_0 \mathbf{P}. \quad (2.6)$$

Further, we may write  $\frac{1}{\epsilon_0\mu_0} = c^2$ , where  $c$  is the speed of light, and  $\frac{\omega^2}{c^2} = k^2$ , where  $k$  is the wave number of the propagating field. Also,  $\nabla \times \nabla \times \mathbf{E} = -\Delta\mathbf{E} + \nabla(\nabla \cdot \mathbf{E})$  where  $\Delta$  denotes the 3d Laplacian operator ( $\Delta = \frac{\partial^2}{\partial x^2} + \frac{\partial^2}{\partial y^2} + \frac{\partial^2}{\partial z^2}$ ). The electric field is linearly polarized in a fixed transverse direction. Furthermore, since the field has high frequency oscillations along the  $z$ -direction, its variations along the transverse directions may be considered negligible. It is therefore standard in optics to neglect  $\nabla(\nabla \cdot \mathbf{E})$ , hence, equation (2.6) takes the form of a wave equation and can be written as

$$\Delta\mathbf{E} + k^2\left(\mathbf{E} + \frac{1}{\epsilon_0}\mathbf{P}\right) = 0. \quad (2.7)$$

During fiber amplifier operation, multiple lights of different wavelengths can be present inside the fiber at any given moment. All the individual fields satisfy (2.7) independently. So assuming that there are  $\mathfrak{M}$  number of total wavelengths present inside the fiber at any given moment, for each wavelength  $\lambda_\ell$  the electric field wave equation (2.7) is written as,

$$\Delta\mathbf{E}_\ell + k_\ell^2\left(\mathbf{E}_\ell + \frac{1}{\epsilon_0}\mathbf{P}_\ell\right) = 0, \quad \text{where } \ell = 1, \dots, \mathfrak{M}. \quad (2.8)$$

where  $\mathbf{E}_\ell$ ,  $k_\ell$ , and  $\mathbf{P}_\ell$  respectively denote the electric field, wave-number, and the polarization field of the light of wavelength  $\lambda_\ell$ .

## 2.2 Electric Polarizations ( $\mathbf{P}_\ell$ ) and Propagation Model

All the interactions between the propagation material and the electric field occur through the electric polarization. Electric polarization refers to the separation of the center of positive charge and the center of negative charge in a material. The separation can be caused by a sufficiently high-magnitude electric field. The polarization model used in this dis-

sertation [22] accounts for linear background material interaction, background linear loss, active laser gain, passive Raman gain, and thermal effects. The polarization model takes the form,

$$\mathbf{P}_\ell = \mathbf{P}_\ell^{\text{background}} + \mathbf{P}_\ell^{\text{linear loss}} + \mathbf{P}_\ell^{\text{active gain}} + \mathbf{P}_\ell^{\text{optical non-linearity}} + \mathbf{P}_\ell^{\text{thermal}}. \quad (2.9)$$

Another way to express electric polarization is through electric susceptibility,

$$\mathbf{P}_\ell = \varepsilon_0 \left( \chi_\ell^{(1)} \cdot \mathbf{E}_\ell + \chi_\ell^{(2)} : \mathbf{E}_\ell \mathbf{E}_\ell + \chi_\ell^{(3)} :: \mathbf{E}_\ell \mathbf{E}_\ell \mathbf{E}_\ell + \dots \right), \quad (2.10)$$

where  $\chi_\ell^{(j)}$  is the  $j^{\text{th}}$  order electric susceptibility, which is given by a tensor of rank  $j + 1$ . The index  $\ell$  denotes the corresponding wavelength of the optical field. Electric susceptibility is a dimensionless proportionality constant that indicates the extent or degree of polarization of a dielectric material in response to an applied electric field. For most linear dielectric materials, the polarization is directly proportional to the average electric field strength, with a constant proportionality ratio of two. The greater the electric susceptibility, the greater the ability of a material to polarize in response to the field, and thereby reduce the total electric field inside the material (and store energy) [9, 8]. A medium made of material whose molecular geometry has inversion symmetry in it, like  $\text{SiO}_2$  in optical fibers, has negligible second order susceptibilities. All of the polarizations mentioned above derive from the first order susceptibility term  $\chi^{(1)}$  except the Raman optical non-linearity, which derives from the third order susceptibility term  $\chi^{(3)}$ . The different polarizations considered in our model are discussed in the following subsections.

### 2.2.1 Background Polarization

The electric permittivity of a dielectric medium can be expressed as

$$\epsilon_\ell = \epsilon_0 \left( 1 + \chi_\ell^{(1)} \right).$$

The real part of the electric permittivity is linked to the refractive index of the fiber material through the relation  $n^2 = \Re\left(\frac{\epsilon}{\epsilon_0}\right)$ . Thus,  $\Re\left(\chi_\ell^{(1)}\right) = n^2 - 1$ . Finally, the polarization due to background material interaction in terms of the real component of the first order susceptibility is given by  $\epsilon_0 \left( \Re\left(\chi_\ell^{(1)}\right) \mathbf{E}_\ell \right)$ . Therefore

$$\mathbf{P}_\ell^{\text{background}} \approx \epsilon_0 \left( n^2 - 1 \right) \mathbf{E}_\ell. \quad (2.11)$$

### 2.2.2 Linear Loss

The laser gain or loss in the fiber is accounted for by the imaginary component of the first-order susceptibility given by  $\left( -\frac{n\gamma_\ell}{k_\ell} \right)$  [64], where  $\gamma_\ell$  denotes the gain function of the  $\ell^{\text{th}}$  wavelength. The polarization quantity can be approximated by  $\epsilon_0 \left( i \Im\left(\chi^{(1)}\right) \mathbf{E}_\ell \right)$ , where  $\Im(\cdot)$  denotes the imaginary part of the number. Linear or optical loss causes the optical fiber to lose energy so the linear loss quantity can be thought of as a negative gain and thus can be denoted by  $\gamma_\ell = -\alpha_\ell$  with  $\alpha_\ell \in \mathbb{R}^+$ . Therefore,

$$\mathbf{P}_\ell^{\text{linear loss}} \approx \frac{i\epsilon_0 n}{k_\ell} \alpha_\ell \mathbf{E}_\ell. \quad (2.12)$$

The value  $\alpha_\ell$  is often called the attenuation constant of the fiber.



### 2.2.3 Active Laser Gain

The active laser gain, or just active gain, is the most important quantity behind the amplification of the signal. Similar to section 2.2.2, the polarization term is derived from the imaginary part of the first order susceptibility. We denote the active laser gain function by  $\gamma_\ell = g_\ell$ . Therefore,

$$\mathbf{P}_\ell^{\text{active gain}} \approx -\frac{i\varepsilon_0 n}{k_\ell} g_\ell \mathbf{E}_\ell. \quad (2.13)$$

The core of an active fiber amplifier is usually doped with lanthanide rare-earth elements like Ytterbium (Yb), Thulium (Tm), Erbium (Er), or Holmium (Ho). In this dissertation we will discuss only Yb- and Tm-doped fibers.

#### 2.2.3.1 Tm-dopant ion dynamics

The Tm ion population dynamics are schematically represented in Figure 2.1. The model involves four manifolds. The total number of Tm ions (per volume) is

$$N_{\text{total}} = N_0(x, y, z, t) + N_1(x, y, z, t) + N_2(x, y, z, t) + N_3(x, y, z, t) \quad (2.14)$$

where  $N_0$  represents the ground state (manifold 0) ion-population concentration, while  $N_1$ ,  $N_2$ , and  $N_3$  denote ion concentrations at excitation manifolds 1, 2, and 3, respectively. What we have named energy manifolds 0, 1, 2, and 3, represent Tm energy levels usually written as  ${}^3H_6$ ,  ${}^3F_4$ ,  ${}^3H_5$  and  ${}^3H_4$ , respectively. Pump light of frequency between 790 nm and 793 nm excites the Tm ground state ions into higher energy manifolds, thus depleting manifold 0 at the rate  $f_p \sigma^{\text{abs}}(\omega_p) N_0$  while increasing the excited manifold  $j$  at the rate  $f_p \sigma^{\text{ems}}(\omega_p) N_j$ , where  $\sigma^{\text{abs}}$  and  $\sigma^{\text{ems}}$  represent measurable absorption and emission cross sections of Tm [1], and  $f_\ell = \frac{I_\ell}{\hbar \omega_\ell}$ ,  $\ell \in \{s, p\}$  represents the flux of photons of frequency  $\omega_\ell$ ,

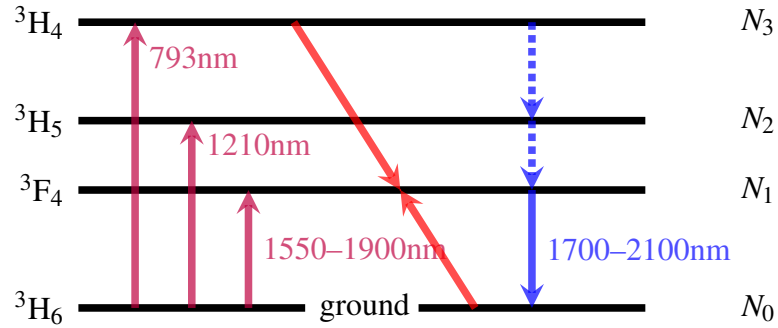


Figure 2.1: Simplified diagram of Tm energy levels

where  $\hbar$  is the Planck's constant. We must also take into account the fact that an excited ion in manifold  $j$  can decay spontaneously to a lower energy manifold  $k$  at the rate  $1/\tau_{jk}$ . An excited ion in manifold  $j$  can also decay non-radiatively to the next lower energy manifold at the rate  $\Gamma_j$ . Finally, two nearby Tm ions may exchange energy with one another through a process called cross-relaxation, wherein one Tm ion has an electron in the highest energy manifold of the four that have been mentioned; this electron drops to an intermediate energy level by giving some of its energy to an electron in the ground state of other Tm ion, also raising it to an intermediate energy level. Cross-relaxation is represented by the slanted arrows in Figure 2.1, while the other processes are represented by up/down arrows. The rate constant for the cross-relaxation is denoted by  $\kappa_R$ , which is directly proportional to the total dopant concentration. Higher concentrations put more Tm ions near one another, thus increasing the probability of the cross-relaxation event. The cross-relaxation, which creates two excited Tm ions for every pump photon (a two-for-one process), increases the amplifier efficiency (while upconversions, which are neglected in our model, decrease fiber

efficiency). Following [40], these processes are modeled by

$$\partial_t N_3 = \psi_p^{\text{abs}} N_0 - \left( \psi_p^{\text{ems}} \nu_p + \frac{1}{\tau_{32}} + \frac{1}{\tau_{31}} + \frac{1}{\tau_{30}} + \Gamma_3 + \kappa_R N_0 \right) N_3 \quad (2.15a)$$

$$\partial_t N_2 = \left( \frac{1}{\tau_{32}} + \Gamma_3 \right) N_3 - \left( \frac{1}{\tau_{21}} + \frac{1}{\tau_{20}} + \Gamma_2 \right) N_2 \quad (2.15b)$$

$$\partial_t N_1 = \psi_s^{\text{abs}} N_0 + \left( \frac{1}{\tau_{21}} + \Gamma_2 \right) N_2 + \left( \frac{1}{\tau_{31}} + 2\kappa_R N_0 \right) N_3 - \left( \frac{1}{\tau_{10}} + \Gamma_1 + \psi_s^{\text{ems}} \right) N_1 \quad (2.15c)$$

$$N_{\text{total}} = N_0 + N_1 + N_2 + N_3 \quad (2.15d)$$

where

$$\psi_\ell^{\text{abs}} = \sigma^{\text{abs}}(\omega_\ell) f_\ell, \quad \psi_\ell^{\text{ems}} = \sigma^{\text{ems}}(\omega_\ell) f_\ell, \quad \ell \in \{s, p\}.$$

Next, we make the simplifying assumption that all the time derivatives  $\partial_t$  in (2.15) may be neglected. By doing so, we are neglecting the time variations in the ion populations that occur at an extremely small time scale of around  $10^{-8}$  s.

$$0 = \psi_p^{\text{abs}} N_0 - \left( \psi_p^{\text{ems}} \nu_p + \frac{1}{\tau_{32}} + \frac{1}{\tau_{31}} + \frac{1}{\tau_{30}} + \Gamma_3 + \kappa_R N_0 \right) N_3 \quad (2.16a)$$

$$0 = \left( \frac{1}{\tau_{32}} + \Gamma_3 \right) N_3 - \left( \frac{1}{\tau_{21}} + \frac{1}{\tau_{20}} + \Gamma_2 \right) N_2 \quad (2.16b)$$

$$0 = \psi_s^{\text{abs}} N_0 + \left( \frac{1}{\tau_{21}} + \Gamma_2 \right) N_2 + \left( \frac{1}{\tau_{31}} + 2\kappa_R N_0 \right) N_3 - \left( \frac{1}{\tau_{10}} + \Gamma_1 + \psi_s^{\text{ems}} \right) N_1 \quad (2.16c)$$

Equations (2.15a)–(2.15c) after setting  $\partial_t = 0$  immediately yield  $N_1, N_2, N_3$  in terms of  $N_0$ . The last equation (2.15d) then gives a quadratic equation for  $N_0$ . To express this solution,

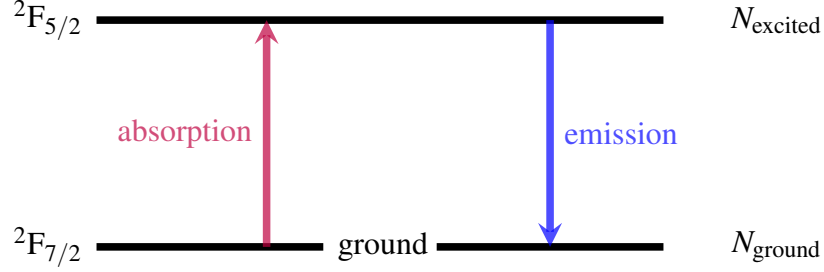


Figure 2.2: A simplified diagram of two Yb energy levels

first define

$$\delta_i = \sum_{j=0}^{i-1} \tau_{ij} + \Gamma_i, \quad \gamma_0 = \frac{1}{\psi_p^{\text{ems}} + \delta_3}, \quad \gamma_1 = \psi_p^{\text{abs}} \gamma_0, \quad \gamma_2 = \frac{\tau_{32}^{-1} + \Gamma_3}{\delta_2},$$

$$\gamma_3 = \frac{\tau_{31}^{-1} + \gamma_2(\tau_{21}^{-1} + \Gamma_2) + \gamma_1^{-1} \psi_s^{\text{abs}}}{\psi_s^{\text{ems}} + \delta_1}, \quad \gamma_4 = \frac{2\psi_p^{\text{abs}} + \psi_s^{\text{abs}}}{\psi_p^{\text{abs}}(\psi_s^{\text{ems}} + \delta_1)}.$$

Then, the steady-state solution is given explicitly by

$$N_0 = \frac{\gamma_0 \kappa_R N_{\text{total}} - \gamma_1 (1 + \gamma_2 + \gamma_3) - 1}{2\kappa_R (\gamma_0 + \gamma_1 \gamma_4)} + \frac{\sqrt{(1 - \gamma_0 \kappa_R N_{\text{total}} + \gamma_1 (1 + \gamma_2 + \gamma_3))^2 + 4(\gamma_0 + \gamma_1 \gamma_4) \kappa_R N_{\text{total}}}}{2\kappa_R (\gamma_0 + \gamma_1 \gamma_4)}, \quad (2.17a)$$

$$N_1 = \frac{(\gamma_3 + \gamma_4 \kappa_R N_0) \gamma_1 N_0}{1 + \gamma_0 \kappa_R N_0}, \quad N_2 = \frac{\gamma_2 \gamma_1 N_0}{1 + \gamma_0 \kappa_R N_0}, \quad N_3 = \frac{\gamma_1 N_0}{1 + \gamma_0 \kappa_R N_0}. \quad (2.17b)$$

Using this, we set the gain expressions by

$$g_s = \sigma^{\text{ems}}(\omega_s) N_1 - \sigma^{\text{abs}}(\omega_s) N_0 \quad (2.18)$$

$$g_p = \sigma^{\text{ems}}(\omega_p) N_3 - \sigma^{\text{abs}}(\omega_p) N_0. \quad (2.19)$$

### 2.2.3.2 Yb-dopant ion dynamics

The model for population dynamics of Yb ions is simpler as it can be modeled using only two energy states, the ground state and one excited state manifold, as shown in Figure 2.2. Hence, instead of (2.14), we now have

$$N_{\text{total}} = N_{\text{ground}}(x, y, z, t) + N_{\text{excited}}(x, y, z, t)$$

where  $N_{\text{total}}$  denotes the total population concentration in the fiber,  $N_{\text{ground}}$  represents the ground state ion-population (in  ${}^2F_{7/2}$ ) and  $N_{\text{excited}}$  denotes the excited state ion-population (in  ${}^2F_{5/2}$ ). The absorption and emission that model the two-state dynamics now result in

$$\frac{\partial N_{\text{excited}}}{\partial t} = \psi_s^{\text{abs}} N_{\text{ground}} - \psi_s^{\text{ems}} N_{\text{excited}} \quad (2.20a)$$

$$+ \psi_p^{\text{abs}} N_{\text{ground}} - \psi_p^{\text{ems}} N_{\text{excited}} - \frac{N_{\text{excited}}}{\tau},$$

$$N_{\text{total}} = N_{\text{ground}} + N_{\text{excited}}, \quad (2.20b)$$

where now we must use the absorption and emission cross section values [51] of Yb for  $\sigma^{\text{abs}}, \sigma^{\text{ems}}$  while computing  $\psi_s^{\text{abs}}, \psi_s^{\text{ems}}$ . The parameter  $\tau$  is the upper level radiative lifetime of the excited state. As in the Tm case, we assume that the system has already reached the steady-state solution. Putting the time derivative in (2.20) to zero, a simple calculation shows that

$$N_{\text{excited}} = N_{\text{total}} \frac{\psi_s^{\text{abs}} + \psi_p^{\text{abs}}}{\psi_s^{\text{abs}} + \psi_s^{\text{ems}} + \psi_p^{\text{abs}} + \psi_p^{\text{ems}} + \tau^{-1}}. \quad (2.21)$$

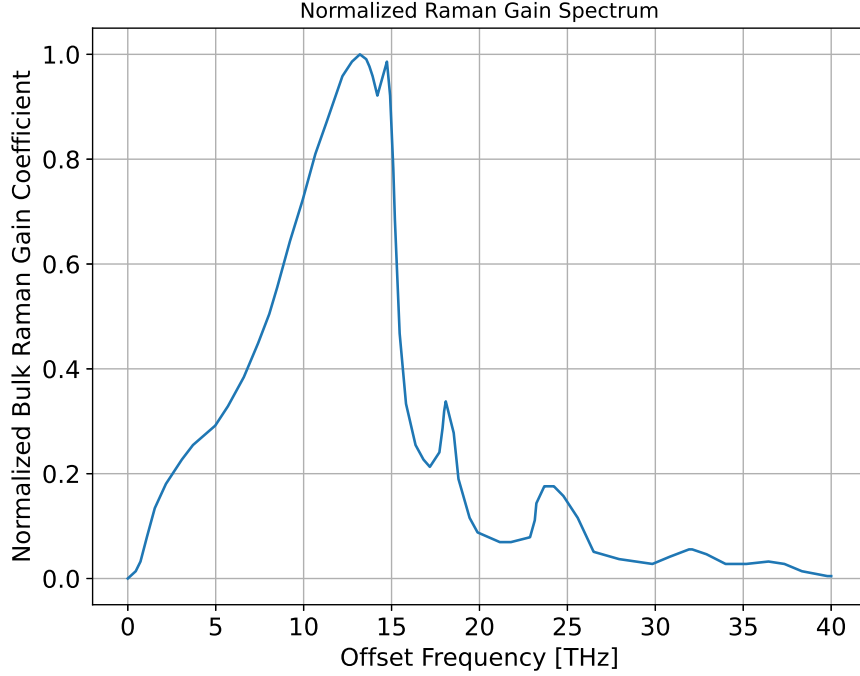


Figure 2.3: Experimentally measured normalized bulk Raman gain coefficient (normalized  $g_R$ ) as the offset frequency between any two operating wavelengths inside the fiber [40].

Finally, the active gain expressions are modeled in terms of the above  $N_{\text{ground}}$  and  $N_{\text{excited}}$  by

$$g_\ell = (\sigma_\ell^{\text{ems}} N_{\text{excited}} - \sigma_\ell^{\text{abs}} N_{\text{ground}}), \quad \text{for } \ell \in \{s, p\}. \quad (2.22)$$

#### 2.2.4 Passive Raman Gain

The stimulated Raman scattering or Stimulated Brillouin Scattering (SBS) is the only optical non-linear contribution used in this dissertation. SBS is derived from the real part of the third order susceptibility term and is given by  $\epsilon_0 \left( \Re \epsilon(\chi^{(3)}) \mathbf{E}_\ell \right)$ . The value of the Raman gain depends on the frequency offset between the operating wavelengths in the fiber. So if

$\lambda_\ell$  and  $\lambda_j$  are two wavelengths operating in the fiber, then the polarization quantity can be written as

$$\mathbf{P}_\ell^{\text{Raman}} \approx -\frac{i\epsilon_0 n}{k_\ell} \Upsilon_\ell^{\text{R}} g_{\text{R}} I_j \mathbf{E}_\ell, \quad (2.23)$$

where  $I_j (\propto |\mathbf{E}_j|^2)$  denotes the irradiance of the wavelength  $\lambda_j$ ,  $g_{\text{R}}$  is a constant which is called the bulk Raman gain coefficient, and  $\Upsilon_\ell^{\text{R}}$  is called the coupling coefficient.

### 2.2.5 Thermal Effects

Heat deposition in fiber laser amplifiers predominately occurs through quantum defect heating, where high energy photons are converted to lower energy photons through the population inversion of the active dopant. The energy lost during the process is referred as the defect. The interaction is modeled with the usual 2d time dependent heat equation given by

$$\rho_0 C \frac{\partial T}{\partial t} = \kappa_{\text{therm}} \Delta_{xy} T + Q(T), \quad (2.24)$$

where  $\rho_0$ ,  $C$ , and  $\kappa_{\text{therm}}$  respectively denote the density, the specific heat capacity, and the thermal conductivity of glass.  $T$  denotes the temperature and  $Q(T)$  accounts for the heat generation inside the fiber. The symbol  $\Delta_{xy}$  is the 2d Laplacian,  $\Delta_{xy} = \frac{\partial^2}{\partial x^2} + \frac{\partial^2}{\partial y^2}$ . Next, instead of modeling the absolute temperature value of the fiber, we take the difference of temperature between the fiber and the atmosphere and use that in (2.24). Then,

$$\rho_0 C \frac{\partial \delta T}{\partial t} = \kappa_{\text{therm}} \Delta_{xy} \delta T + Q(\delta T + T_{\text{atmosphere}}), \quad (2.25)$$

where  $\delta T = T_{\text{fiber}} - T_{\text{atmosphere}}$ . This form of the heat equation also allows one to take a zero Dirichlet boundary condition at the fiber boundary, which models the fact that the fiber sits

on an actively cooled spool that uniformly and efficiently conducts away the heat from the fiber. To simplify notation moving forward, we denote  $T = T(x, y, z, t)$  as the difference of temperature between fiber and its surroundings. Hence, the complete heat equation can be written as

$$\rho_0 C \frac{\partial T}{\partial t} = \kappa_{\text{therm}} \Delta_{xy} T + Q(T), \quad \text{in } \Omega_z \quad (2.26a)$$

$$T = 0, \quad \text{on } \partial\Omega_z \quad (2.26b)$$

where  $\Omega_z$  denotes the fiber cross-sectional area at the longitudinal point  $z$  and  $\partial\Omega_z$  is the boundary of  $\Omega_z$ . The complete weak formulation of equation (2.26) is as follows:

Find  $T \in H_0^1(\Omega_z)$  such that,

$$\left( \frac{dT}{dt}, v \right) + \frac{\kappa_{\text{therm}}}{\rho_0 C} \left( \nabla_{xy} T, \nabla_{xy} v \right) - \frac{1}{\rho_0 C} \left( Q(T), v \right) = 0, \quad (2.27)$$

for all  $v \in H_0^1(\Omega_z)$ . Here,  $H_0^1(\Omega_z) = \left\{ u \in L^2(\Omega_z) : \nabla u \in L^2(\Omega_z), \text{ and } u = 0 \text{ on } \partial\Omega_z \right\}$  and  $(u, v) = \int_{\Omega_z} u \cdot v \, dx \, dy$ .

Next, to determine the heat deposition in the fiber we estimate the energy lost along the fiber as the population inversion converts pump photons into signal photons. Mathematically, this is accomplished by tracking the *net irradiance flux* along the fiber:

$$Q(\mathbf{r}, t) \approx - \sum_{\ell=1}^N \frac{\partial I_{\ell}}{\partial z}(\mathbf{r}, t) \Big|_{\text{heat}}, \quad (2.28)$$

where  $\ell$  sums over the various frequencies within the fiber, assuming those frequencies are well-separated from one another [62]. Otherwise, the summation can be thought of as an integral envelope about the bandwidth of frequencies of interest. The partial derivative



in the longitudinal direction (2.28), in this case, only refers to changes in the irradiance that result in heat production. The main sources for heat deposition in the fiber include gain processes that ultimately result in the conversion of high frequency (energy) photons into lower frequency (energy) photons, or through loss mechanisms where the medium absorbs energy, such as intrinsic losses in the fused silica and/or hydroxide contamination. Rayleigh scattering and bend loss do not lead to heating. Thus, the net irradiance flux expression (2.28) can be written as

$$Q(\mathbf{r}, t) \approx - \sum_{\ell=1}^N \left[ g_{\ell}(\mathbf{r}, t) I_{\ell}(\mathbf{r}, t) + \Upsilon_{\text{R}}^{\ell} g_{\text{R}} I_{\ell}(\mathbf{r}, t) - \alpha_{\text{heat}}^{\ell} I_{\ell}(\mathbf{r}, t) \right]. \quad (2.29)$$

where  $\alpha_{\text{heat}}^{\ell}$  is comprised of any absorption losses.

Finally, the effect of thermal loading on electric polarization can be modeled through a simple perturbation model of the refractive index [47]. We write

$$\mathbf{P}_{\ell}^{\text{thermal}} \approx 2\epsilon_0 n \delta n \mathbf{E}_{\ell}. \quad (2.30)$$

where  $\delta n$  is the thermally induced perturbation to the refractive index and is modeled as  $\delta n = \frac{dn}{dT} T$ . We call  $\frac{dn}{dT}$  the thermo-optic coefficient of glass, a constant which is measured experimentally.

## 2.2.6 Propagation Model

Using (2.9) and all the polarization expressions from the previous subsections, we get

$$\begin{aligned}
\mathbf{P}_\ell &= \mathbf{P}_\ell^{\text{background}} + \mathbf{P}_\ell^{\text{linear loss}} + \mathbf{P}_\ell^{\text{active gain}} + \mathbf{P}_\ell^{\text{optical non-linearity}} + \mathbf{P}_\ell^{\text{thermal}} \\
&\approx \varepsilon_0 \left( n^2 - 1 \right) \mathbf{E}_\ell + \frac{i\varepsilon_0 n}{k_\ell} \alpha_\ell \mathbf{E}_\ell - \frac{i\varepsilon_0 n}{k_\ell} g_\ell \mathbf{E}_\ell - \frac{i\varepsilon_0 n}{k_\ell} \Upsilon_\ell^{\text{R}} g_{\text{R}} I_j \mathbf{E}_\ell + 2\varepsilon_0 n \delta n \mathbf{E}_\ell \\
&\approx \varepsilon_0 \left( n^2 - 1 + \frac{in}{k_\ell} \alpha_\ell - \frac{in}{k_\ell} g_\ell - \frac{in}{k_\ell} \Upsilon_\ell^{\text{R}} g_{\text{R}} I_j + 2n\delta n \right) \mathbf{E}_\ell.
\end{aligned}$$

Therefore, replacing  $\mathbf{P}_\ell$  in (2.7) yields the following

$$\left( \mathbf{E}_\ell + \frac{1}{\varepsilon_0} \mathbf{P}_\ell \right) \approx \left( n^2 + \frac{in}{k_\ell} \alpha_\ell - \frac{in}{k_\ell} g_\ell - \frac{in}{k_\ell} \Upsilon_\ell^{\text{R}} g_{\text{R}} I_j + 2n\delta n \right) \mathbf{E}_\ell. \quad (2.31)$$

Using (2.31) we rewrite (2.8) as

$$\Delta \mathbf{E}_\ell + k_\ell^2 n^2 \mathbf{E}_\ell + \left( ink_\ell \alpha_\ell - ink_\ell g_\ell - ink_\ell \Upsilon_\ell^{\text{R}} g_{\text{R}} I_j + 2n\delta n k_\ell^2 \right) \mathbf{E}_\ell = 0. \quad (2.32)$$

We denote the term  $\left( ink_\ell \alpha_\ell - ink_\ell g_\ell - ink_\ell \Upsilon_\ell^{\text{R}} g_{\text{R}} I_j + 2n\delta n k_\ell^2 \right)$  in equation (2.32) by  $m_\ell(x, y, z, t)$  and write the propagation model as a perturbed Helmholtz system as

$$\Delta \mathbf{E}_\ell + k_\ell^2 n^2 \mathbf{E}_\ell + m_\ell(x, y, z, t) \mathbf{E}_\ell = 0. \quad (2.33)$$

The step-index fibers used in this dissertation are all weakly guided. A step-index fiber is called weakly guiding when the difference of refractive index between the core and the clad is very small (usually less than 1%). A weakly guided fiber ensures the validity of the paraxial approximation in which the majority of the optical power propagates along the longitudinal fiber axis. In this dissertation we only use polarization maintaining fiber,

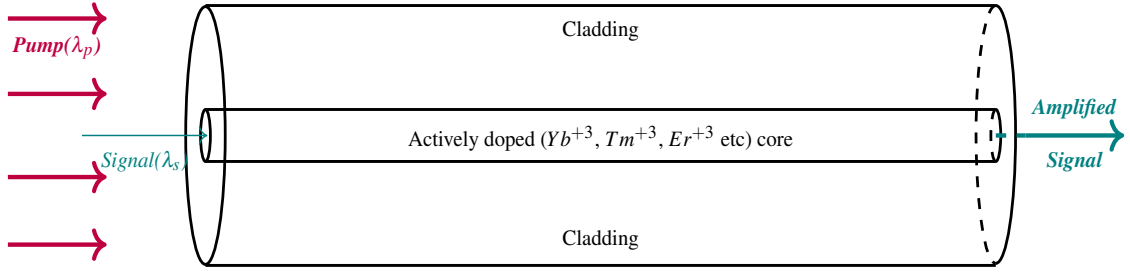


Figure 2.4: A visual representation of basic configuration of an optical fiber amplifier

thus for simplicity we assume that the light injected is polarized only in the direction of the  $x$ -axis. Consequently,  $\mathbf{E}_\ell^y$  and  $\mathbf{E}_\ell^z$  are negligible. The longitudinal component of the electric field ( $\mathbf{E}_\ell^x$ ) has a very high frequency oscillation in that direction. As a result, we assume  $U_\ell(x, y, z) = \mathbf{E}_\ell(x, y, z) \cdot \hat{e}_x$  and write the scalar form of equation (2.33) as follows:

$$\Delta U_\ell + k_\ell^2 n^2 U_\ell + m_\ell(x, y, z, t) U_\ell = 0. \quad (2.34)$$

### 2.3 Coupled Mode Theory

In guided wave-optics, CMT is a mathematical approach that approximates each optical field present in the fiber waveguide as a set of individually propagating transverse guided modes. This technique requires a separation of variables between the transverse directions  $(x, y)$  and the propagation direction  $(z)$ . CMT was first introduced in the literature in the early 1950's [52, 42]. Later Schelkunoff [54], and Haus [26] derived the detailed formulation of coupled mode equations. CMT was first applied to microwave oscillation and propagation. In addition, it was employed in the application of microwave traveling-wave tubes [52], and backward-wave oscillators [21]. CMT was introduced in guided wave

optics by Snyder [63], Marcuse [38], Yariv [68], and Kogelnik [35] in the early 1970's.

The electric field of a propagating light through a guided optical fiber can be thought of as a superposition of the individual guided mode fields. Guided modes are effectively orthogonal distributions of electric field amplitude where the intensity profile of the mode remains unchanged during propagation. Since, we are injecting a linearly polarized laser source, we use the linearly polarized or Linearly Polarized (LP) modes in this dissertation. These are discussed in more detail in the following subsection.

### **2.3.1 Optical fiber Modes**

Mathematically, discontinuous structures such as propagation index steps can be treated by imposing boundary conditions on the wave equations. In this section we examine the propagation of monochromatic light in step-index fibers using electromagnetic theory. We aim to determine the electric and magnetic fields of guided waves that satisfy Maxwell's equation and the boundary conditions imposed by the cylindrical dielectric core and cladding. As in all waveguides, say for wavelength  $\lambda_\ell$ , there are certain special solutions called modes. Each of which has a distinct propagation constant  $\beta_\ell$ , a characteristic field distribution in the transverse plane  $\varphi_\ell$  and two independent polarization states.

#### **2.3.1.1 Mode Equations, and its exact solutions**

We assume the domain to be the cross-section of a step-index optical fiber with core radius  $r_{\text{core}}$ , and cladding radius  $r_{\text{clad}}$ . Let  $n_{\text{core}}$  and  $n_{\text{clad}}$  be, respectively, the refractive indices of the core and the cladding region. The following derivation uses the cylindrical co-ordinate system with coordinates  $(r, \phi, z)$ . We know that each scalar component of the electric field

must satisfy the Helmholtz equation. So we write

$$\Delta U_\ell + n^2 k_0^2 U_\ell = 0, \quad (2.35)$$

where  $n = n_{\text{core}}$  in the core ( $r < r_{\text{core}}$ ) and  $n = n_{\text{clad}}$  in the cladding ( $r > r_{\text{core}}$ ) and  $k_\ell = 2\pi/\lambda_\ell$ . We assume that the radius  $r_{\text{clad}}$  of the cladding is sufficiently large so that it can safely be assumed to be infinite when examining guided light in the core and near the core-cladding boundary. In a cylindrical coordinate system equation (2.35) becomes,

$$\frac{\partial^2 U_\ell}{\partial r^2} + \frac{1}{r} \frac{\partial U_\ell}{\partial r} + \frac{1}{r^2} \frac{\partial^2 U_\ell}{\partial \phi^2} + \frac{\partial^2 U_\ell}{\partial z^2} + n^2 k_0^2 U_\ell = 0. \quad (2.36)$$

We are interested in solutions that take the form of waves traveling in the  $z$  direction with a propagation constant  $\beta$ , so that the  $z$ -dependence of  $U_\ell$  is of the form  $e^{-i\beta z}$ . Since  $U_\ell$  must be a periodic function of the angle  $\phi$  with period  $2\pi$ , we assume that the dependence on  $\phi$  is harmonic,  $e^{il\phi}$ , where  $l$  is an integer. Substituting,  $U_\ell(r, \phi, z) = u_\ell(r) e^{-il\phi} e^{-i\beta z}$  in (2.36), an ordinary differential equation for  $u_\ell(r)$  is obtained, which is given as follows

$$\frac{d^2 u_\ell(r)}{dr^2} + \frac{1}{r} \frac{du_\ell(r)}{dr} + \left( n^2 k_0^2 - \beta^2 - \frac{l^2}{r^2} \right) u_\ell(r) = 0. \quad (2.37)$$

Now a mode of a propagating wave is called guided (or bounded) if the ratio of the corresponding propagation constant and  $k_0$  is smaller than the core refractive index and greater than the cladding refractive index ( $n_{\text{core}} k_0 > \beta > n_{\text{clad}} k_0$ ). It is therefore convenient to define  $\kappa_T^2 = n_{\text{core}}^2 k_0^2 - \beta^2$  and  $\gamma^2 = \beta^2 - n_{\text{clad}}^2 k_0^2$ , so that for guided waves  $\kappa_T^2$  and  $\gamma^2$  are positive and  $\kappa_T$  and  $\gamma$  are real. Equation (2.37) may then be written separately for the core

and the cladding as follows:

$$\frac{d^2 u_\ell(r)}{dr^2} + \frac{1}{r} \frac{du_\ell(r)}{dr} + \left( \kappa_T^2 - \frac{l^2}{r^2} \right) u_\ell(r) = 0, \quad r < r_{\text{core}}, \quad (2.38a)$$

$$\frac{d^2 u_\ell(r)}{dr^2} + \frac{1}{r} \frac{du_\ell(r)}{dr} - \left( \gamma^2 + \frac{l^2}{r^2} \right) u_\ell(r) = 0, \quad r > r_{\text{core}}. \quad (2.38b)$$

The solutions for equations (2.38) are the family of Bessel functions. Excluding functions that approach  $\infty$  at  $r = 0$  in the core or as  $r \rightarrow \infty$  in the cladding, we obtain the bounded solutions,

$$u_\ell(r) = \begin{cases} A \mathcal{J}_l(\kappa_T r), & r < r_{\text{core}}, \\ B \mathcal{K}_l(\gamma r), & r > r_{\text{core}}, \end{cases} \quad (2.39)$$

where  $\mathcal{J}_l$  is the Bessel function of first-kind of order  $l$  and  $\mathcal{K}_l$  is the modified Bessel function of second-kind of order  $l$ . In the limit  $x \gg 1$ ,

$$\mathcal{J}_l(x) \approx \left( \frac{2}{\pi x} \right)^{1/2} \cos \left[ x - \left( l + \frac{1}{2} \right) \frac{\pi}{2} \right], \quad (2.40)$$

$$\mathcal{K}_l(x) \approx \left( \frac{\pi}{2x} \right)^{1/2} \left( 1 + \frac{4l^2 - 1}{8x} \right) e^{-x}. \quad (2.41)$$

The parameters  $\kappa_T$  and  $\gamma$  determine the rate of change of  $u_\ell(r)$  in the core and in the cladding, respectively. A large value of  $\kappa_T$  means faster oscillation of the radial distribution in the core. A large value of  $\gamma$  means faster decay and smaller penetration of the wave into the cladding. Also, letting NA denote the numerical aperture, we observe,  $\kappa_T^2 + \gamma^2 = (n_{\text{core}}^2 - n_{\text{clad}}^2) k_0^2 = \text{NA}^2 \cdot k_0^2$ . So as  $\kappa_T$  increases,  $\gamma$  decreases and the field penetrates deeper into the cladding. As  $\kappa_T$  exceeds  $(\text{NA} \cdot k_0)$ ,  $\gamma$  becomes imaginary and the wave ceases to be bound to the core. It is convenient to normalize  $\kappa_T$  and  $\gamma$  by defining  $X = \kappa_T a$  and  $Y = \gamma a$ . Therefore we may write  $X^2 + Y^2 = V^2$ , where  $V = \text{NA} \cdot k_0 \cdot r_{\text{core}}$ . We shall see shortly that

the so called V-number, or normalized frequency, is an important parameter that governs the number of modes of the fiber, as well as the propagation constants of the modes. It is important to remember that for the wave to be guided,  $X$  must be smaller than  $V$ .

Now if the field has only very small longitudinal components, it can be treated as approximately transverse electromagnetic. The interface conditions require the continuity of  $u_\ell(r)$  and its derivatives  $\frac{du_\ell}{dr}$  at  $r = r_{\text{core}}$ . Thus,

$$A \mathcal{J}_l(\kappa_T r_{\text{core}}) - B \mathcal{K}_l(\gamma r_{\text{core}}) = 0, \quad (2.42a)$$

$$A \kappa_T \mathcal{J}'_l(\kappa_T r_{\text{core}}) - B \gamma \mathcal{K}'_l(\gamma r_{\text{core}}) = 0. \quad (2.42b)$$

For this system of equations to have non-trivial solutions, the system determinant must vanish. This yields

$$\mathcal{J}_l(\kappa_T r_{\text{core}}) \gamma \mathcal{K}'_l(\gamma r_{\text{core}}) - \mathcal{K}_l(\gamma r_{\text{core}}) \kappa_T \mathcal{J}'_l(\kappa_T r_{\text{core}}) = 0. \quad (2.43)$$

Next, employing the identities  $\mathcal{J}'_l(x) = \pm \mathcal{J}_{l\mp 1}(x) \mp \left(\frac{l}{x}\right) \mathcal{J}_l(x)$  and  $\mathcal{K}'_l(x) = -\mathcal{K}_{l\mp 1}(x) \mp \left(\frac{l}{x}\right) \mathcal{K}_l(x)$ , and using the normalizing parameters, we can express equation (2.43) as

$$X \frac{\mathcal{J}_{l\pm 1}(X)}{\mathcal{J}_l(X)} = \pm Y \frac{\mathcal{K}_{l\pm 1}(Y)}{\mathcal{K}_l(Y)}. \quad (2.44)$$

Equation (2.44) is called the characteristic equation. Given  $V$  and  $l$ , the characteristic equation contains a single unknown variable  $X$  (since  $Y^2 = V^2 - X^2$ ). Note that  $\mathcal{J}_{-1}(x) = (-1)^l \mathcal{J}_l(x)$  and  $\mathcal{K}_{-l}(x) = \mathcal{K}_l(x)$ , so that if  $l$  is replaced with  $-l$ , the equation remains unchanged. Once we solve for  $X$ , we can choose  $A = \mathcal{K}_l(\gamma r_{\text{core}})$  and write  $B = \mathcal{J}_l(\kappa_T r_{\text{core}})$

using any of the boundary conditions. Then the final solution can be written as

$$u_\ell(r) = \begin{cases} \mathcal{K}_l(\gamma r_{\text{core}}) \mathcal{J}_l(\kappa_T r), & r < r_{\text{core}}, \\ \mathcal{J}_l(\kappa_T r_{\text{core}}) \mathcal{K}_l(\gamma r), & r > r_{\text{core}}. \end{cases} \quad (2.45)$$

The characteristic equation (2.44) may be solved graphically by plotting its right-hand-side (RHS) and left-hand-side (LHS) versus  $X$  and finding the intersections. It can be shown that for  $l = 0$ , the LHS has multiple branches and the RHS drops monotonically with increasing  $X$  until it vanishes at  $X = V$ . Therefore, there are multiple intersections in the interval  $0 < X \leq V$ . Each intersection point corresponds to a fiber mode with a distinct value of  $X$ . These values are denoted  $X_{lm}$ ,  $m = 1, 2, \dots, M_l$  in order of increasing  $X$ . Once the  $X_{lm}$  are found, the corresponding transverse propagation constants  $\kappa_{Tlm}$ , the decay parameters  $\gamma_{lm}$ , the propagation constants  $\beta_{lm}$ , and the radial distribution functions  $u_{lm}(r)$  may be readily determined using (2.45). The propagation constant can then be written as,

$$\beta_{lm} = \sqrt{n_{\text{core}}^2 k_0^2 - \frac{X_{lm}^2}{r_{\text{core}}^2}}. \quad (2.46)$$

### 2.3.1.2 Mode Cutoff and number of Modes

It is evident from the graphical construction that as  $V$  increases, the number of intersections (modes) increases since the LHS of the characteristic equation (2.44) is independent of  $V$ , whereas the RHS-branches moves to the right as  $V$  increases. Considering the minus signs in the characteristic equation, branches of the LHS intersect the abscissa when  $\mathcal{J}_{l-1}(X) = 0$ . These roots are denoted by  $x_{lm}$ ,  $m = 1, 2, \dots$ . The number of modes  $M_l$  is therefore equal to the number of roots of  $\mathcal{J}_{l-1}(X)$  that are smaller than  $V$ . The  $(l, m)$  mode is allowed if  $V > x_{lm}$ . As  $V$  decreases further, the  $(l, m - 1)$  mode also reaches its cutoff point when a



new root is reached and so on. The smallest root of  $J_{l-1}(X)$  is  $x_{01} = 0$  for  $l = 0$  and the next smallest is  $x_{11} = 2.405$  for  $l = 1$ . When  $V < 2.405$ , all modes with the exception of the fundamental  $LP_{01}$  mode are cut off. The fiber then operates as a single mode waveguide.

### 2.3.1.3 Hybrid Mode Theory

We can solve for the modes in a more general way using the hybrid mode theory. The equation solved here is as follows.

$$\left( \frac{\mathcal{J}'_l(\kappa_T r_{\text{core}})}{\kappa \mathcal{J}_l(\kappa_T r_{\text{core}})} + \frac{\mathcal{K}'_l(\gamma r_{\text{core}})}{\gamma \mathcal{K}_l(\gamma r_{\text{core}})} \right) \left( k_1^2 \frac{\mathcal{J}'_l(\kappa_T r_{\text{core}})}{\kappa_T \mathcal{J}_l(\kappa_T r_{\text{core}})} + k_2^2 \frac{\mathcal{K}'_l(\gamma r_{\text{core}})}{\gamma \mathcal{K}_l(\gamma r_{\text{core}})} \right) = \left( \frac{\beta l}{r_{\text{core}}} \right)^2 \left( \frac{1}{\kappa_T^2} + \frac{1}{\gamma^2} \right)^2. \quad (2.47)$$

Solving this equation we get  $\beta_{lm}$ . Now there are 4 types of modes:  $TE_{lm}$ ,  $TM_{lm}$ ,  $HE_{lm}$ , and  $EH_{lm}$ . The propagation constants of some modes are almost identical.

- $HE_{l+1,m}$  and  $EH_{l-1,m}$  are degenerate.
- $TE_{0m}$ ,  $TM_{0m}$ ,  $HE_{2m}$  are degenerate.
- In general we cannot visualize these modes separately. The superposition of these modes corresponds to particular LP modes which we observe.

For LP modes we often make the weakly guiding approximation, i.e.  $NA \ll 1$ ,  $k_{\text{core}} \approx k_{\text{clad}} \approx \beta$ . This gives after simplification,

$$l = \begin{cases} 1, & \text{TE, TM} \\ \nu + 1, & \text{EH} \\ \nu_1, & \text{HE} \end{cases} \quad (2.48)$$

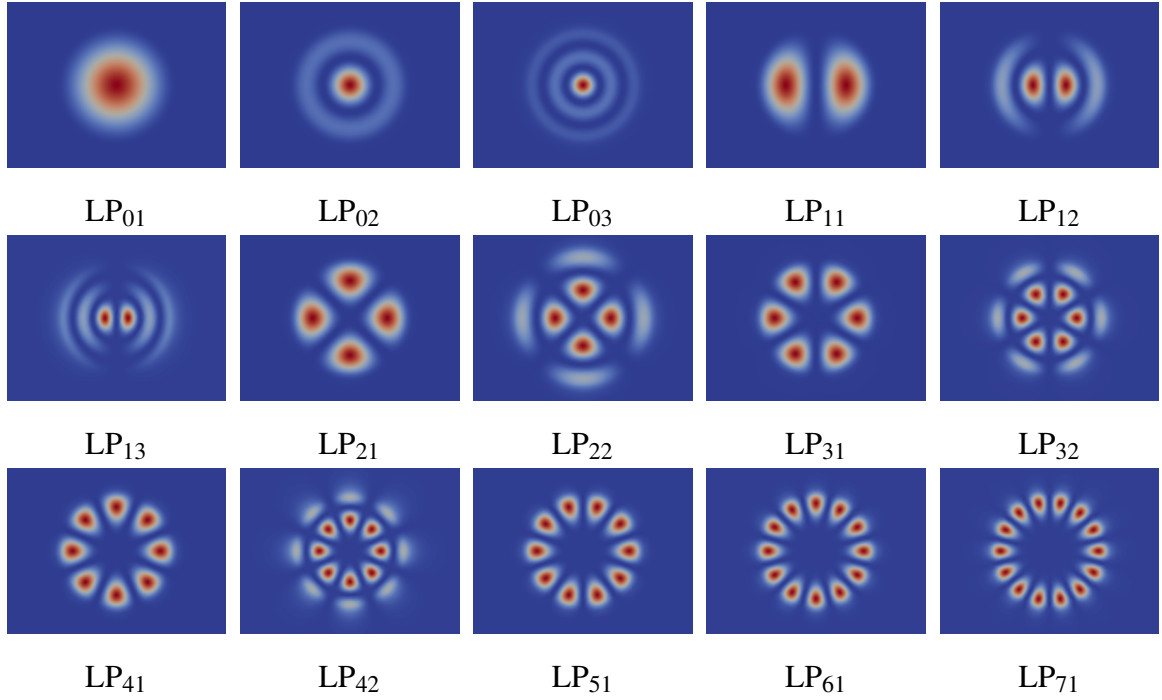


Figure 2.5: Transverse intensity profiles of different fiber modes

and

$$\frac{\kappa_T \mathcal{J}_{l-1}(\kappa_T r_{\text{core}})}{\mathcal{J}_l(\kappa_T r_{\text{core}})} + \frac{\gamma \mathcal{K}_{l-1}(\gamma r_{\text{core}})}{\mathcal{K}_l(\gamma r_{\text{core}})} = 0. \quad (2.49)$$

- Each  $\text{LP}_{0m}$  mode is derived from an  $\text{HE}_{1m}$  mode.
- Each  $\text{LP}_{1m}$  mode is coming from  $\text{TE}_{0m}$ ,  $\text{TM}_{0m}$  and  $\text{HE}_{2m}$  modes.
- Each  $\text{LP}_{lm}$  mode ( $l \geq 2$ ) is from an  $\text{HE}_{l+1,m}$  and an  $\text{EH}_{l-1,m}$  mode.

### 2.3.2 CMT ansatz

In this section we try to build an ansatz for our problem to apply to our CMT formulation.

The guided modes can be determined using the following eigenvalue equation:

$$(\Delta_{xy} + k_\ell^2 n^2) \varphi_m^\ell = \beta_m^{\ell 2} \varphi_m^\ell. \quad (2.50)$$

The individual mode fields can be written as

$$U_\ell^m = A_m^\ell(z) \varphi_m^\ell(x, y) e^{i\beta_m^\ell z}, \quad (2.51)$$

where  $U_\ell^m$ ,  $A_m^\ell(z)$ ,  $\varphi_m^\ell(x, y)$ , and  $\beta_m^\ell$  are the electric field, amplitude, mode-profile, and the propagation constant of the  $m^{\text{th}}$  mode of the  $\ell^{\text{th}}$  light wavelength, respectively. Assuming that the fiber supports  $M_\ell$  modes corresponding to the  $\ell^{\text{th}}$  wavelength of light, to apply CMT in our model we use the following ansatz for the electric field:

$$U_\ell = \sum_{m=1}^{M_\ell} A_m^\ell(z) \varphi_m^\ell(x, y) e^{i\beta_m^\ell z}. \quad (2.52)$$

### 2.3.3 Governing Equations

Finally, we apply the ansatz (2.52) to (2.34). The derivation is as follows:

$$\begin{aligned} \Delta U_\ell &= \sum_{m=1}^{M_\ell} A_m^\ell(z) \Delta_{xy} \varphi_m^\ell(x, y) e^{i\beta_m^\ell z} \\ &+ \sum_{m=1}^{M_\ell} \varphi_m^\ell(x, y) e^{i\beta_m^\ell z} \left( \frac{d^2 A_m^\ell(z)}{dz^2} + 2i\beta_m^\ell \frac{dA_m^\ell(z)}{dz} - \beta_m^{\ell 2} A_m^\ell(z) \right). \end{aligned}$$

We assume that  $A_m^\ell(z)$  is a slowly varying function of  $z$  (having built the fast variations in  $z$  into the  $e^{i\beta_m z}$  term). Accordingly, for each  $A_m^\ell$ , we neglect the second-order derivative  $\frac{d^2 A_m^\ell}{dz^2}$  for all  $m = 1, \dots, M_\ell$ . Doing so, and using (2.50), we obtain for  $0 < z < L$

$$\sum_{m=1}^{M_\ell} \frac{dA_m^\ell}{dz} \varphi_m^\ell \beta_m^\ell e^{i\beta_m^\ell z} = \sum_{m=1}^{M_\ell} A_m^\ell n \left( -k_\ell \alpha_\ell + k_\ell \Upsilon_\ell^R g_{Rj} + \frac{1}{2} k_\ell g_\ell + ik_\ell^2 \delta n \right) \varphi_m^\ell e^{i\beta_m^\ell z}. \quad (2.53)$$

The next step is to multiply both sides of (2.53) by the complex conjugate of  $\varphi_l^\ell$ , namely  $\bar{\varphi}_l^\ell$ , and integrate. We integrate over  $\Omega_z$ , which represents the fiber cross section having the constant longitudinal coordinate value of  $z$ . Then, simplifying using the  $L^2(\Omega_z)$ -orthogonality of the modes,

$$\frac{dA_l^\ell}{dz} = \sum_{m=1}^{M_\ell} e^{i(\beta_m^\ell - \beta_l^\ell)z} K_{lm}^\ell A_m^\ell, \quad \text{for } 0 < z < L, \quad (2.54a)$$

$$\text{where } K_{lm}^\ell = \int_{\Omega_z} \text{Pol } \varphi_m^\ell \bar{\varphi}_l^\ell dx dy. \quad (2.54b)$$

The term "Pol" in equation (2.54a) refers to the associated electric polarization terms. We call the function  $K_{lm}^\ell$  the coupling coefficient between modes  $\varphi_l$ , and  $\varphi_m$ . Equation 2.54 is the main Ordinary Differential Equation (ODE) that we shall try to solve in this dissertation in different amplifier scenarios.

### 2.3.3.1 Governing equation for pump light

For the pump light, the number of guided cladding modes is exceedingly large:  $M_p > 10^5$ . Rather than modeling each of these modes, it is sufficient to approximate the pump field as a plane wave, which effectively acts as the composition of all of the pump guided modes [47, 59]. Accordingly, we set  $M_p = 1$  and the normalized mode  $\varphi_1^p = (\sqrt{\pi} r_{\text{clad}})^{-1}$

(without a transverse dependence). Since the cladding region is many times larger than the core, the corresponding propagation constant is estimated as if this mode travels in a uniform medium of refractive index  $n_{\text{clad}}$ , i.e., we set  $\beta_1 = k_p n_{\text{clad}} = \frac{\omega_p}{c} n_{\text{clad}}$ . Then (2.54) yields

$$\frac{dA_1^p}{dz} = K_{11}^p(I_p, I_s)A_1^p, \quad (2.55)$$

for  $0 < z < L$ , where

$$K_{11}^p(I_p, I_s) = \frac{1}{2\pi r_{\text{clad}}^2 n_{\text{clad}}} \int_{\Omega_z} g_p(I_p, I_s) n_{\text{clad}} dx dy = \frac{1}{2} \langle g_p \rangle. \quad (2.56)$$

Here  $\langle g_p \rangle = |\Omega_z|^{-1} \int_{\Omega_z} g_p dx dy$  denotes the mean value of  $g_p$  taken over  $\Omega_z$ , the area of the fiber cross section out to  $r = r_{\text{clad}}$ .

The irradiance, shown below, is proportional to the square of the field envelope magnitude,

$$I_\ell = \frac{n}{\mu_0 c} |U_\ell|^2.$$

Using (2.52),

$$I_\ell(x, y, z) = \frac{n}{\mu_0 c} \left| \sum_{m=1}^{M_\ell} A_m^\ell(z) e^{i\beta_m^\ell z} \Phi_m^\ell(x, y) \right|^2. \quad (2.57)$$

For the pump plane wave, this reduces to

$$I_p(z) = \frac{n}{\mu_0 c \pi r_{\text{clad}}^2} |A_1^p(z)|^2.$$

Using the equation (2.55) and its complex conjugate, elementary simplifications lead to the following governing ODE for the pump irradiance:

$$\frac{dI_p}{dz} = \langle g_p \rangle I_p. \quad (2.58)$$

Next, consider the signal irradiance, namely the  $\ell = s$  case in (2.57). To highlight the dependence of  $I_s$  on  $A_m^s$ , we use  $A^s \equiv [A_1^s(z), \dots, A_{M_s}^s(z)]^t$  to collectively denote the set of all signal mode amplitudes and write

$$I_s \equiv I_s(x, y, z, A^s) = \frac{n}{\mu_0 c} \left| \sum_{m=1}^{M_s} A_m^s(z) e^{i\beta_m^s z} \varphi_m^s(x, y) \right|^2. \quad (2.59)$$

Note that the modes  $\varphi_l^s(x, y)$  and the propagation constants  $\beta_l^s$  may be precomputed. The cost of this precomputation corresponds to the “off-line” computational cost in this reduced-order model.

### 2.3.3.2 Full CMT model

In order to complete the CMT model (assuming we have expressions for  $g_\ell$ ), we need to provide initial conditions at  $z = 0$ , the beginning of the fiber. What is usually known is the power contained in the pump and signal light. The initial pump irradiance  $I_p^0 = I_p(0)$  can be calculated from the initial pump power  $P_p^0$  provided at the inlet in a co-pumped configuration by  $I_p^0 = \frac{1}{|\varphi_1^p|^2} P_p^0$ . We assume that we also know how the signal light is split into various modes at the inlet, i.e., we may set  $A^\ell(0)$  to some given  $A^\ell(0) = [A_1^\ell(0), \dots, A_{M_\ell}^\ell(0)]^t$ . In practice, most of the signal power is usually carried in the first fundamental mode.

To summarize, the CMT model computes

$$Y(z) = [I_p(z), A_1^\ell(z), A_2^\ell(z), \dots, A_{M_\ell}^\ell(z)]^t, \quad 0 < z < L,$$

where each  $A_m^\ell(z)$  is a signal mode amplitude in the fiber core, and  $Y(z)$  satisfies the ODE

system

$$\frac{dY}{dz} = \begin{bmatrix} \langle g_p(Y) \rangle & 0 \\ 0 & \phi^\ell(z) \cdot K^\ell(Y) \end{bmatrix} Y, \quad 0 < z < L, \quad (2.60a)$$

$$Y(0) = [I_p^0, A^\ell(0)]^t \quad z = 0. \quad (2.60b)$$

The ODE system is coupled with the heat equation (2.26) through the coupling term  $K^\ell(Y)$ . Here,  $\phi^\ell(z)$  is an  $M_\ell \times M_\ell$  matrix defined by  $\phi_{lm}^\ell(z) = e^{i(\beta_m^\ell - \beta_l^\ell)z}$ ,  $K^\ell(Y)$  is a matrix of the same size whose  $(l, m)$ th entry is  $K_{lm}^\ell(I_s, I_p)$  defined in (2.54b), and  $\phi^\ell(z) \cdot K^\ell(Y)$  denotes the Hadamard product of  $\phi^\ell$  and  $K^\ell$ , i.e.,  $[\phi^\ell \cdot K^\ell]_{lm} = \phi_{lm}^\ell K_{lm}^\ell$ .

## 2.4 Two-tone, Raman hybrid laser amplifier model

If a fiber amplifier is seeded with only one laser source-signal, then the amplifier configuration is called *single-tone* configuration. However, when more than one highly coherent laser source is seeded into the amplifier, a laser gain competition (LGC) between the various laser wavelengths develops within the active dopant [45]. To demonstrate the suppression of the stimulated Brillouin scattering (SBS) non-linearity in optical fibers, Dajani et al. [11, 69] were able to utilize the LGC configuration, which was built upon an idea by Weßels et al. [67]. They studied an Yb-doped amplifier, which was seeded with two lasers. By carefully selecting the initial laser seed ratio and by choosing the wavelengths of the two lasers separated by at least  $\Delta\lambda \sim > 10$  nm, a substantial SBS mitigation was achieved. The configuration was named *two-tone* amplifier configuration. The additional laser source for the two-tone configuration usually has a core-pumped laser source that is in-between the wavelength of the pump light and the signal light; subsequently, this wavelength shall

be referred to as the *tone* ( $\lambda_t$ ); thus,  $\lambda_p < \lambda_t < \lambda_s$ .

Generally, optical non-linearities, i.e. SBS, Stimulated Raman scattering (SRS), Kerr effects, Four-wave mixing (FWM), etc., arise in high-power fibers because of two reasons. If the wavelengths inside the fiber gets long interaction lengths then this allows for the non-linear processes to build-up; and/or if the propagating light has very high irradiance levels, it allows very pronouns interactions with the medium and/or with the optical field itself. The two-tone configuration helps suppress the onset of optical non-linearities by reducing the effective length over which any laser field has a high power (thus, high irradiance). The other advantages of a two-tone configuration includes the fact that heat generation is further spread out along the fiber length, leading to the lower peak temperatures [44]. Also, the two-tone configuration mitigates the onset of amplified spontaneous emission (ASE), and therefore also parasitic lasing [4].

For the two-tone configured fibers, the tone wavelength is chosen to be exactly 13.2 THz higher in frequency than the signal wavelength in order to take advantage of the peak Raman gain in a fused silica medium (see Fig. 2.3).

### 2.4.1 Governing equations

The model focuses on forward propagating light along the longitudinal direction ( $+z$ ) of the fiber.  $n_l^\ell = \beta_l^\ell / k_\ell$  denotes the effective index of refraction of the  $l^{\text{th}}$  mode at the given wavelength  $\ell$ . The steady-state active gain via spontaneous emission is represented with  $g_a$ . In our model, as mentioned earlier, we choose the  $\lambda_t$  exactly 13.2 THz higher in frequency than  $\lambda_s$ , where the peak of the Raman gain occurs. Although, Raman gain also occurs between the ASE wavelengths, and between the laser sources and ASE wavelengths, these interactions are neglected since the model is not attempting to accurately capture the condi-



tions once there are significant amounts of ASE power present in the fiber. The dimensionless quantity for the Raman gain is  $Y_R^{\ell=t} = -\omega_t/\omega_s$  for the tone, and  $Y_R^{\ell=s} = 1$  for the signal. We use the complement wavelength index such that  $\ell^c = t$  when  $\ell = s$ , and  $\ell^c = s$  when  $\ell = t$ . The value  $\alpha_{\text{loss}} > 0$  is the sum of the background silica-, hydroxide contamination-, and mode-bend-losses. The losses at the pump wavelength are considered to be insignificant. The wavelength bandwidth over which the spontaneous emission occurs, namely the bin bandwidth for the five central ASE wavelengths, is denoted as  $\Delta\lambda_{\text{ASE}}$ .

For the tone and signal wavelengths ( $\ell \in \{t, s\}$ ), where there are  $M_{\ell \in \{t, s\}} = 3$  guided core modes (LP<sub>01</sub> and both orientations of LP<sub>11</sub>), and  $l = 1, \dots, M_{\ell \in \{t, s\}}$ , the propagation is governed by

$$\frac{dA_l^\ell}{dz} = -\frac{\alpha_{\text{loss}}^\ell}{2}A_l^\ell + \sum_{m=1}^{M_\ell} e^{i(\beta_m^\ell - \beta_l^\ell)z} K_{lm}^\ell A_m^\ell \quad (2.61)$$

$$\text{where, } K_{lm}^\ell = \int_{\Omega_z} \left( \frac{k_\ell}{2\beta_l^\ell} g_\ell + \frac{k_\ell Y_R^\ell g_R I_{\ell^c}}{2\beta_l^\ell} + \frac{ik_\ell^2}{2\beta_l^\ell} \delta n \right) n \varphi_m^\ell \overline{\varphi_l^\ell} dx dy.$$

For the ASE wavelengths ( $\ell = a$ ), only the fundamental mode is modeled ( $M_a = 1$  and  $l = 1 = m$ ):

$$\frac{dA_1^a}{dz} = K_{11}^a A_1^a - \frac{\alpha_{\text{loss}}^a}{2} A_1^a + \mathcal{C}_{11}^a \mathcal{Y}_1^a, \quad (2.62)$$

$$\text{where, } K_{11}^a = \int_{\Omega_z} \left( \frac{k_a}{2\beta_1^a} g_a + \frac{ik_a^2}{2\beta_1^a} \delta n \right) n \varphi_1^a \overline{\varphi_1^a} dx dy,$$

$$\mathcal{C}_{11}^a = \int_{\Omega_z} \frac{k_a}{2\beta_1^a} g_a n \varphi_1^a \overline{\varphi_1^a} dx dy, \quad \text{and} \quad \mathcal{Y}_1^a = \sqrt{\frac{2\mu_0 \hbar c^3}{n_1^a \lambda_a^3} \Delta\lambda_{\text{ASE}}}.$$

For the (planewave) pump wavelength ( $\ell = p$ ), we use equation (2.58). For heat generation we also modify the heat-source quantity. The majority of the heat is generated within the

core area, even though the Raman gain process between the relevant irradiance profiles occurs over the entire cross-sectional overlap area. Now, the heat generated due to Raman gain is negligible. So we only consider heat generation in the core region and the heat source term can be modeled as follows:

$$Q \approx - \left( \underbrace{g_s I_s + g_t I_t + g_p I_p + \sum_{m=1}^{M_a} g_{a_m} I_{a_m}}_{\substack{\text{net active} \\ \text{gain} \\ \text{(stimulated} \\ \text{emission)}}} + \underbrace{\sum_{m=1}^{M_a} g_{a_m} I_{a_m}}_{\substack{\text{net active} \\ \text{gain} \\ \text{(spontaneous} \\ \text{emission)}}} + \underbrace{\sum_{\ell \in \{t,s\}} \Upsilon_R^\ell g_R I_s I_t}_{\substack{\text{net Raman} \\ \text{gain}}} - \underbrace{\sum_{\ell \in \{t,s,a\}} \alpha_{\text{therm}}^\ell I_\ell}_{\substack{\text{absorption} \\ \text{losses}}} \right), \quad (2.63)$$

where the absorption losses ( $\alpha_{\text{therm}}^\ell > 0$ ) sum the hydroxide contamination and background silica (via phonon absorption) losses. Also, for simplicity, this model uses the thermal parameters for glass in the polymer region. However, in order to improve the accuracy of the reported change in temperature in the fiber, we approximately correct the change in temperature value, as if all calculations were done with the proper polymer thermal parameters and appropriate boundary condition at the glass-polymer interface, by using the steady-state thermal profile that one would get if the heat generation occurred uniformly in the active gain region (core region) of the fiber:

$$T(r) = \frac{q_{\text{heat}}}{4\pi} \begin{cases} \frac{2}{\kappa_{\text{therm}}^{\text{SiO}_2}} \ln \left( \frac{r_{\text{clad}}}{r_{\text{core}}} \right) + \frac{2}{\kappa_{\text{therm}}^{\text{poly}}} \ln \left( \frac{r_{\text{fiber}}}{r_{\text{clad}}} \right) + \frac{1}{\kappa_{\text{therm}}^{\text{SiO}_2}} \left( 1 - \left( \frac{r}{r_{\text{core}}} \right)^2 \right), & r \in [0, r_{\text{core}}] \\ \frac{2}{\kappa_{\text{therm}}^{\text{SiO}_2}} \ln \left( \frac{r_{\text{clad}}}{r} \right) + \frac{2}{\kappa_{\text{therm}}^{\text{poly}}} \ln \left( \frac{r_{\text{fiber}}}{r_{\text{clad}}} \right), & r \in (r_{\text{core}}, r_{\text{clad}}] \\ \frac{2}{\kappa_{\text{therm}}^{\text{poly}}} \ln \left( \frac{r_{\text{fiber}}}{r} \right), & r \in (r_{\text{clad}}, r_{\text{fiber}}] \end{cases}, \quad (2.64)$$

where,  $r_{\text{fiber}}$  is the radius of the entire fiber, including the polymer. The thermal conductivity of the polymer is denoted as  $\kappa_{\text{therm}}^{\text{poly}}$ . In this case, the peak change in temperature

always occurs at the center of the fiber cross-section, and is given by

$$T_{\text{peak}} = T(r = 0) = \frac{q_{\text{heat}}}{4\pi} \left[ \frac{2}{\kappa_{\text{therm}}^{\text{SiO}_2}} \ln \left( \frac{r_{\text{clad}}}{r_{\text{core}}} \right) + \frac{2}{\kappa_{\text{therm}}^{\text{poly}}} \ln \left( \frac{r_{\text{fiber}}}{r_{\text{clad}}} \right) + \frac{1}{\kappa_{\text{therm}}^{\text{SiO}_2}} \right]. \quad (2.65)$$

This correction to the reported change in temperature value is derived by approximating the uniform heat deposition per unit length ( $q_{\text{heat}}$ ) using the actual full heat generation in the amplifier simulation ( $Q$ ), i.e.,

$$q_{\text{heat}}(z_0) \approx \iint_{\Omega_{z_0}^{\text{core}}} Q(x, y, z_0) d\Omega_z.$$

Then, using either relation (2.65) or relation (2.64), one can very reasonably approximate the peak change in temperature in the transverse cross-section of the fiber or find the approximate peak temperature in the polymer jacket of the fiber. The results from the two-tone model are illustrated in chapter 6.

## **Chapter 3**

### **Fiber amplifier code implementation and parallelization**

Suppose we are attempting to assemble a 10,000-piece jigsaw puzzle on a rainy weekend. The number of pieces is staggering, and instead of a weekend it might take us several weeks to finish the puzzle. Now assume we have a team of friends helping with the puzzle. It progresses much faster, and we are able to finish the puzzle within desired weekend. This principle is the central idea behind parallel computation. We can dramatically cut down on computation by splitting one large task into smaller tasks that multiple processors can perform all at once. With parallel processes, a task that would normally take several weeks can potentially be reduced to several hours.

A serial process is simply a process that is run entirely by one core of one processor. This means tasks are run one after another as they appear in code. This is analogous to you doing the jigsaw puzzle on your own.

A parallel process is a process that is divided among multiple cores in a processor or set of processors. Each sub-process can have its own memory as well as share memory with other processes. This is analogous to doing the puzzle with the help of friends. Since a supercomputer has a large network of nodes with many cores, we must implement parallelization strategies with our applications to fully utilize a super-computing resource.

### **3.1 Distributed Memory Parallelization**

One of the first considerations in parallel programming is the relationship between the cores and the machine's memory. Each core in a multi-core processor chip has coherent access to the same memory as the other cores in that chip. Many modern nodes have several sockets that allow several chips to be located on the same board. Each node in a parallel job will have one or more of the user's executables running on it. These executables will be called tasks. These tasks can further be parallelized using shared memory parallelism through multiple threads.

#### **3.1.1 General Attributes**

- Distributed memory systems require a communication network to connect inter-processor memory.
- Processors have their own local memory. Memory addresses in one processor do not map to another processor, so there is no concept of global address space across all processors.
- Because each processor has its own local memory, it operates independently. Changes it makes to its local memory have no effect on the memory of other processors.
- When a processor needs access to data in another processor, it is usually the task of the programmer to explicitly define how and when data is communicated. Synchronization between tasks is likewise the programmer's responsibility.

### **3.1.2 Advantages and disadvantages**

Memory of a computer is scalable with the number of processors. As we increase the number of processors, the size of memory increases proportionately. Each processor can rapidly access its own memory without interference and without the overhead incurred with trying to maintain global cache coherency. Distributed memory parallelism can make use of commodity, off-the-shelf processors and networking, which make it cost effective.

On the other hand, the programmer is responsible for many of the details associated with data communication between processors. It may be difficult to map existing data structures, based on global memory, to this memory organization. Also, one should beware of communication costs and non-uniform memory access times: data residing on a remote node takes longer to access than node local data.

### **3.1.3 Hybrid Distributed-Shared memory parallelism**

The largest and fastest computers in the world today employ both shared and distributed memory architectures. The shared memory component can be a shared memory machine and/or graphics processing units (GPU). The distributed memory component is the networking of multiple shared memory/GPU machines, which know only about their own memory - not the memory on another machine. Therefore, network communications are required to move data from one machine to another. Current trends seem to indicate that this type of memory architecture will continue to prevail and increase at the high end of computing for the foreseeable future.

### 3.2 Parallelism Utilization

The fiber amplifier code we have developed is both shared and distributed memory parallel. The distributed memory parallelism is achieved by dividing the fiber into equal parts and assigning each part to individual nodes. Then each node performs task-based shared memory parallelism using the number of cores it has. For shared memory parallelism we use the facilities provided with the software NGSolve. The distributed memory parallelization of our code is developed using message passing interface, or MPI. High performance computing (HPC) clusters are able to solve big problems using a large number of processors, where the processors work simultaneously to produce exceptional computational power and to significantly reduce the total computational time. In such scenarios, scalability is widely used to indicate the ability of hardware and software to deliver greater computational power when the amount of resources is increased. For HPC clusters, it is important that they are scalable, in other words that the capacity of the whole system can be proportionally increased by adding more hardware. For software, scalability is sometimes referred to as parallelization efficiency — the ratio between the actual speedup and the ideal speedup obtained when using a certain number of processors. In this section we focus on software scalability and discuss two common types of scaling: Strong scaling and weak scaling. The speedup in parallel computing can be straightforwardly defined as

$$\text{speedup} = t_1/t_N$$

where  $t_1$  is the computational time for running the software using one processor, and  $t_N$  is the computational time running the same software with  $N$  processors. Ideally, we would like software to have a linear speedup that is equal to the number of processors (speedup

=  $N$ ), as that would mean that every processor would be contributing 100% of its computational power. Unfortunately, this is a very challenging goal for real applications to attain.

### 3.2.1 Amdahl's law and Strong scaling

In 1967, Amdahl pointed out that the speedup is limited by the fraction of the serial part of the software that is not amenable to parallelization [3]. Amdahl's law can be formulated as follows

$$\text{speedup} = 1 / (s + p/N)$$

where  $s$  is the proportion of execution time spent on the serial part,  $p$  is the proportion of execution time spent on the part that can be parallelized, and  $N$  is the number of processors. Amdahl's law states that, for a fixed problem size, the upper limit of speedup is determined by the serial fraction of the code. This is called strong scaling and can be explained by the following example. Consider a program that takes 20 hours to run using a single processor core. Suppose a particular part of the program takes one hour to execute and cannot be parallelized ( $s = 1/20 = 0.05$ ). Consequently, the code that takes up the remaining 19 hours of execution time can be parallelized ( $p = 1 - s = 0.95$ ). Then regardless of how many processors are devoted to a paralleled execution of this program, the minimum execution time cannot be less than that critical one hour. Hence, the theoretical speedup is limited to at most 20 times (when  $N = \infty$ ,  $\text{speedup} = 1/s = 20$ ). As such, the parallelization efficiency decreases as the amount of resources increases. For this reason, parallel computing with many processors is useful only for highly parallelized programs.



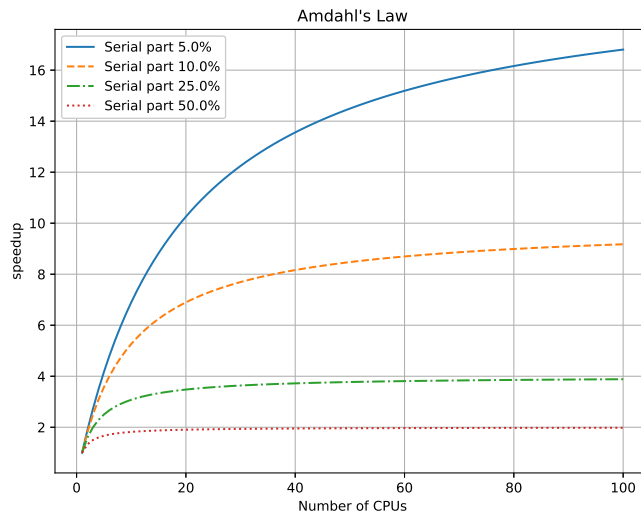


Figure 3.1: Amdahl's Law

### 3.2.2 Gustafson's law and weak scaling

Amdahl's law gives the upper limit of speedup for a problem of fixed size. This seems to be a bottleneck for parallel computing; if one would like to gain a 500 times speedup on 1000 processors, Amdahl's law requires that the proportion of serial part of the problem cannot exceed 0.1%. In practice, however, Gustafson [24] points out that the sizes of problems scale with the amount of available resources. If a problem only requires a small amount of resources, it is not beneficial to use a large amount of resources to carry out the computation. A more reasonable choice is to use small amounts of resources for small problems and larger quantities of resources for big problems. Gustafson's law [24] was proposed in 1988, and is based on the approximations that the parallel part scales linearly with the amount of resources, and that the serial part does not increase with respect to the

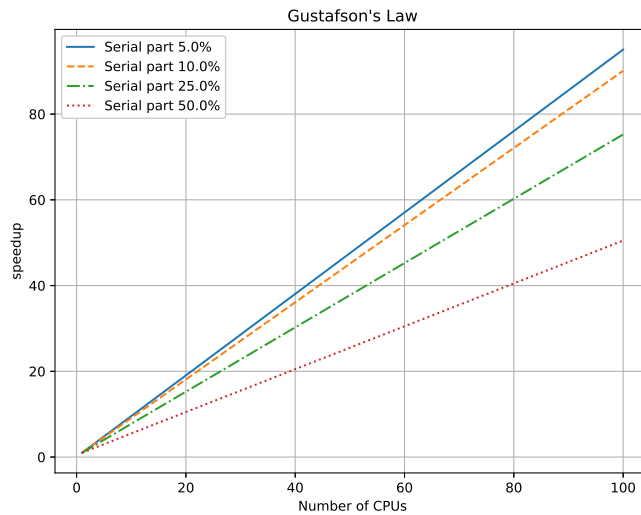


Figure 3.2: Gustafson's Law

size of the problem. It provides the formula for scaled speedup

$$\text{scaled speedup} = s + pN$$

where  $s$ ,  $p$  and  $N$  have the same meaning as in Amdahl's law. With Gustafson's law, the scaled speedup increases linearly with respect to the number of processors (with a slope smaller than one), and there is no upper limit for the scaled speedup. This is called weak scaling, where the scaled speedup is calculated based on the amount of work done for a scaled problem size (in contrast to Amdahl's law which focuses on fixed problem size). If we apply Gustafson's law to the previous example of  $s = 0.05$  and  $p = 0.95$ , the scaled speedup will become infinity when infinitely many processors are used. Realistically, if we have  $N = 1000$ , the scaled speedup will be 950.

### 3.3 Scaling of the fiber amplifier model

In this section we will discuss the numerical implementation of the governing equations (2.54), (2.58), and (2.26) stated in chapters 2. Our domain is an  $L$ -meter long (generally  $L \approx 10$  m) fiber with a radius of order  $\mathcal{O}(10^{-5})$ . We propagate the ODE 2.54 by using a  $z$ -stepping method along the fiber. At each longitudinal ODE  $z$ -step, the code computes the integration to compute the coupling coefficient  $K_{lm}^\ell(I_\ell)$ , where  $I_\ell$  denotes the irradiance of the  $\ell^{\text{th}}$  wavelength. The integration consists of the light-material interaction quantities, including gain, loss, temperature, and other relevant quantities. Mathematically, the interaction between the modes in the optical fiber happens through this coupling coefficient. First, we write down the main governing equations as follows. For  $0 < z < L$ ,

$$\frac{dA_l^\ell}{dz} = \sum_{m=1}^{M_\ell} e^{i(\beta_m^\ell - \beta_l^\ell)z} K_{lm}^\ell(I_\ell) A_m^\ell, \quad \text{where } K_{lm}^\ell = \int_{\Omega_z} \text{Pol}(x, y, z, t) \phi_m^\ell \phi_l^\ell dx dy. \quad (3.1a)$$

$$\frac{dI_p}{dz} = \langle g_p \rangle I_p \quad (3.1b)$$

By combining the two ODEs, we obtain the following single system

$$\frac{dY}{dz} = \begin{bmatrix} \langle g_p(Y) \rangle & 0 \\ 0 & \Phi^\ell(z) \cdot K^\ell(Y) \end{bmatrix} Y, \quad 0 < z < L, \quad (3.2)$$

where  $\forall \ell$ ,  $Y(z) = [I_p(z), A_1^\ell(z), A_2^\ell(z), \dots, A_{M_\ell}^\ell(z)]^t$ ,  $\Phi^\ell(z)$  is an  $M \times M$  matrix defined by  $\Phi_{lm}^\ell(z) = e^{i(\beta_m^\ell - \beta_l^\ell)z}$ ,  $K^\ell(Y)$  is a matrix of the same size whose  $(l, m)^{\text{th}}$  entry is  $K_{lm}^\ell$  defined in (3.1a), and  $\Phi^\ell(z) \cdot K^\ell(Y)$  denotes the Hadamard product of  $\Phi^\ell$  and  $K^\ell$ , i.e.,  $[\Phi^\ell \cdot K^\ell]_{lm} = \Phi_{lm}^\ell K_{lm}^\ell$ .

To compute the integration in the coupling coefficient, we compute the term Pol at each

$z$ -step. First, we write down the complete expression of Pol:

$$\text{Pol}(x, y, z, t) = \left( \text{ink}_\ell \alpha_\ell(z) - \text{ink}_\ell g_\ell(x, y, z) - \text{ink}_\ell \Upsilon_\ell^{\text{R}} g_{\text{R}} I_j(x, y, z) + 2nk_\ell^2 \delta n(x, y, z, t) \right).$$

Therefore, at each  $z$ -step of the ODE solver, we must know the values of  $\alpha_\ell$ ,  $g_\ell$ ,  $I_j$ , and  $\delta n$ . The value of  $\alpha_\ell$  is determined from pre-computed experimental values at different  $z$ -positions and temperatures. The value of  $I_j$  is computed using the formula  $I_j = \frac{n}{\mu_0 c} \left| \sum_{m=1}^{M_\ell} A_m^\ell(z) e^{i\beta_m^\ell z} \varphi_m^\ell(x, y) \right|^2$ ,  $g_\ell$  is computed using the steady-state formulas (2.18), (2.19), and (2.22) in chapter 4, and  $\delta n$  is computed by solving the heat equation (2.26).

To analyze power amplification of an amplifier using our model, we do not need the time dependent heat equation (2.26), as the temperature would be constant in this case. For a full scale TMI simulation, however, it is critical to solve the heat deposition and the temperature sufficiently accurately. The following subsections explore the time dependency in more detail and discuss the need for parallization. Solving the governing problem for a physical fiber of length of 10 m for a usual TMI simulation requires the model to run for at least 0.02 seconds (real time, not wall time). This translates to a considerable number of time-steps (2000 time-steps if  $\Delta t = 10^{-5}$  seconds). Such a task requires a large amount of computational resources and time. Parallelizing the design by dividing the fiber into many parts is one of the more straightforward ways to solve the issue (see Figure 3.3). We assign each part of the fiber to a particular node, as shown in Figure 3.4. Each node receives its initial condition from the previous node (except for the first node, which starts the fiber amplifier simulation at  $z = 0$  and already has the initial condition), solves the fiber amplifier problem on the part of the fiber it had received at the beginning, and sends the solution at the last longitudinal  $z$ -point of its own fiber longitudinal section to the next node (except for the last node with the last fiber longitudinal section) as its initial condition.

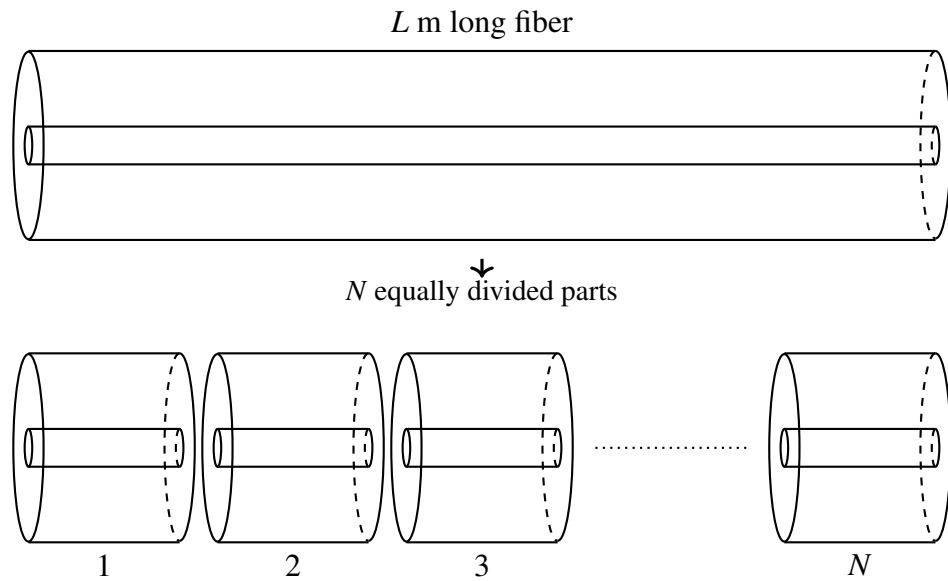


Figure 3.3:  $N$  equally divided parts of the fiber

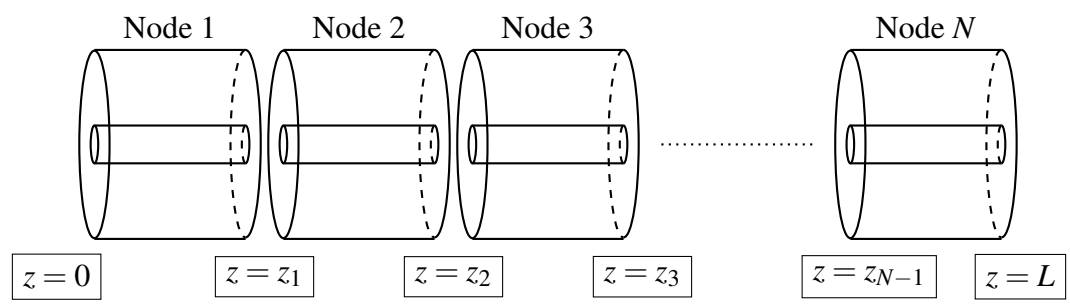


Figure 3.4: Each part of the fiber assigned to an individual node

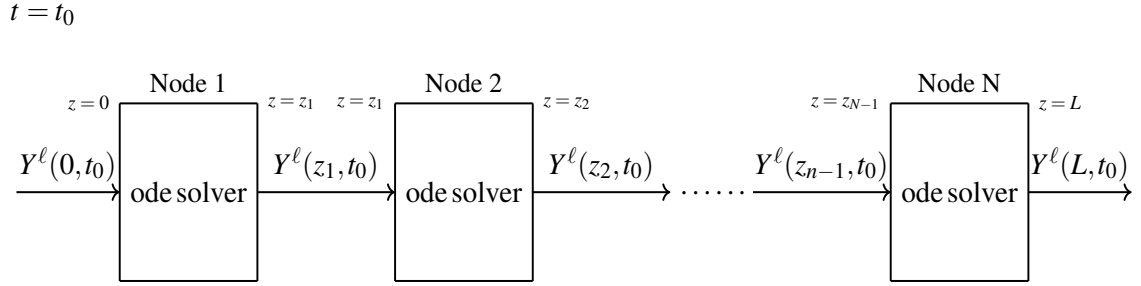


Figure 3.5: Flow of solving the governing problem using  $N$  nodes

During any parallel fiber amplifier simulation, each node stores its own solution for each time-step. Upon completion, the node sends its complete solution to a pre-assigned node which merges the solutions for the sectioned fibers, and produces the final solution for the whole fiber.

### 3.3.1 Time independent simulation

Light propagates through the optical fiber in the longitudinal  $z$  direction. As it propagates, heat is generated due to quantum defect of the molecules/ions in the fiber. As the heat equation (2.26) is the only source of time dependency, a time independent solution of our model implies solving the ODE for a fixed temperature  $T$  (hence for a fixed  $\delta n$ ). We solve the CMT system (3.2) using the classical 4<sup>th</sup> order explicit Runge-Kutta method or simply RK4 method (in complex arithmetic). Most simulations in this dissertation used 50  $z$ -steps per mode beat length unless stated otherwise. Figure 3.5 shows a schematic flow diagram of the mechanism at a given time  $t = t_0$  used in each propagation step.

We may divide the whole implementation into three steps:

1. Construct the coupling term  $\text{Pol}$ ,
2. Build the coupling matrix  $K^\ell$ ,

3. Run the ODE solver to compute the solution.

In step 1 we take the initial value for our ODE solver and calculate  $\alpha_\ell$ , and  $I_j$ . We then compute the active gain  $g_\ell$  based on the doping used in the corresponding active fiber. The value of  $\delta n$  is constant for time-independent simulations. In step 2 the algorithm takes all these values and constructs the coupling matrix  $K^\ell$ . Then finally  $K^\ell$  is fed to the RK4 ODE solver, which solves for the next propagation step. Considering the usual length of an amplifier and their operating wavelengths, our algorithm for a typical amplifier run requires the total number of  $z$ -steps to be in between 300,000 and 450,000.

For time-independent simulations, where the light is propagating only once along the fiber, the parallel code doesn't provide any computational advantage over the serial code. This is due to the fact that each node has to wait until the previous nodes complete their part of the problem. For a single propagation the nodes are not running concurrently. At the same time for a single propagation when a node sends its solution to the next node, it sits idle until the simulation ends. Figure 3.5 shows diagrammatically the flow of solving the problem.

Now suppose we have an  $L$  m long fiber and  $N$  nodes available for computation. We then divide the fiber into  $N$  equal parts and assign the  $j^{\text{th}}$  part to  $j^{\text{th}}$  node. Longitudinally, the  $j^{\text{th}}$  fiber spans from  $z_{j-1}$  to  $z_j$ . So, at time  $t = t_0$ , and  $z = 0$ , and  $Y^\ell(0)$  is fed to Node 1. Node 1 solves the governing problem and produces solution  $Y^\ell(z_1)$ . Then,  $Y^\ell(z_1)$  is fed to Node 2 and Node 2 solves the governing problem using the input as its initial condition. This same process continues for all nodes and stops after Node  $N$  finishes solving the governing problem.

### 3.3.2 Time dependent simulation

Our model can be run for a time dependent simulation as well. In such cases it is critical to calculate the heat deposition and hence the fiber temperature accurately. As mentioned earlier, the current literature suggests that one of the likely causes of TMI is a temperature-induced grating. The characteristic heat diffusion time in the radial direction in a regular amplifier is approximately 1 msec. Experimental evidence shows that TMI may occur anywhere from 1 msec to 20 msec. We used a time-step  $\Delta t = 10^{-5}$  sec. For a 20 msec simulation, the model must run for 2000 time-steps. Figure 3.4 shows a schematic diagram of the time simulation. Here, we may also divide the implementation into the same three steps. In step 1, we also solve the time dependent heat equation (2.26) to compute  $\delta n$ .

As mentioned previously, we divide the fiber into  $N$  equal parts (based on the number of available nodes). Then each part is assigned to a particular node (or computer) where each node solves the same problem (3.2) together with the time-dependent equation (2.26), but with different initial conditions. For the time dependent problem, the solution flow is a little different. When a node finishes its computation and sends the information to the next node, it can start the simulation of its longitudinal section for the next time-step as soon as it receives initial data.

Figures 3.6 through 3.10 show a simple illustration of the solution flow. We suppose that the problem is assigned to a system that has  $N$  nodes. Node  $i$  computes for the fiber-longitudinal section from  $z = z_{i-1}$  to  $z = z_i$ . The solid arrows, dashed arrows, and the dash-dotted arrows, respectively, represent the ODE solver, the heat solver, and the MPI messages that we send to communicate between the nodes. The ODE solution and the heat solution of node  $i$  after time-step  $j$  are respectively denoted by  $Y_i(t_j)$ , and  $T_i(t_j)$ . The back side of the solid and dashed arrows shows the requirement for the solver and the front



side shows the solution from the solver. The dash-dotted arrows can be thought of as a messenger which carries the solution at last  $z$ -step from node  $i$  to node  $i + 1$  as its initial condition. The color green represents that the corresponding job is done, while magenta represents that the corresponding node has all the resources to start that simulation. Finally orange represents that the corresponding simulation has a wait or depends on either an MPI message from the previous node or the previous simulation of the same node. When a node completes all its simulations it stores the corresponding solutions in memory. When a node completes its job, it sends its solution to a preassigned node  $x$ , which merges all the solutions and saves the final solution  $Y$  to disk.

### 3.3.2.1 Speed-up of the fiber amplifier model

Let  $N$  be the number of nodes, and  $n$  the number of time-steps. Let  $\mathcal{T}_i$  be the time for a node to perform initialization on the whole fiber and  $\mathcal{T}$  be the wall time in seconds for one node to compute a full fiber simulation for one time-step (after initialization). Let  $\mathcal{T}_t$  be the time required for a node to transfer to another node a 1 time-step solution for the full fiber. Let  $\mathcal{T}_m$  be the (roughly fixed) time to merge an arbitrary number of longitudinal section solutions for one time-step. We then assume the following:

- All nodes compute at the same rate, so that each node would require  $\mathcal{T}_i + \mathcal{T}$  seconds to initialize and compute one time-step on the whole fiber and  $\frac{\mathcal{T}_i + \mathcal{T}}{N}$  seconds to compute any longitudinal section (of length  $\frac{L}{N}$ ) for one time-step.
- We can neglect the communication time when only initial data are being passed.

Then the wall time to compute  $n$  steps on a full fiber without parallelization would be  $n(\mathcal{T}_i + \mathcal{T})$ . In this case, no final communication or merging is required. The wall time to compute

$n$  steps on a full fiber with parallelization across  $N$  nodes and obtain a merged solution would be  $\mathcal{T}_i + \mathcal{T} + \frac{(n-1)\mathcal{T}}{N} + \frac{n\mathcal{T}_t}{N} + n\mathcal{T}_m$ . This holds since at time  $\mathcal{T}_i + \mathcal{T}$ , all nodes have been initialized and completed at least one time-step, and the last node has completed exactly one time-step. The remaining time for the simulation is just the time for the last node to complete its remaining  $(n-1)$  time-steps. Since it takes this node  $\frac{\mathcal{T}}{N}$  seconds to complete one time-step, the additional time is  $\frac{(n-1)\mathcal{T}}{N}$ . The transfer time is just the time for the last node to send its solution, with the time given by  $\frac{n\mathcal{T}_t}{N}$ . The merge time is  $n\mathcal{T}_m$  assuming linear with the number of time-steps. Then the speedup ratio is  $\frac{n(\mathcal{T}_i + \mathcal{T})}{\mathcal{T}_i + \mathcal{T} + \frac{(n-1)\mathcal{T}}{N} + \frac{n\mathcal{T}_t}{N} + n\mathcal{T}_m}$ .

Upon simplification, the ratio becomes  $\frac{N}{\frac{N}{n} + \frac{\mathcal{T} + \mathcal{T}_t + \mathcal{T}_m}{\mathcal{T}_i + \mathcal{T}} - \frac{\mathcal{T}}{n(\mathcal{T}_i + \mathcal{T})}$ .

For fixed  $N$ , as  $n \rightarrow \infty$ , we get a speedup of

$$\text{speedup} = \frac{N(\mathcal{T} + \mathcal{T}_i)}{(\mathcal{T} + \mathcal{T}_t + \mathcal{T}_m)} \quad (3.3)$$

As we can see that the speed-up trend of our model is linear and can be compared to Gustafson's law.

### 3.3.2.2 Features of the fiber amplifier model

Along with parallelization, this fiber amplifier model has a lot of distinct attributes, which are listed as follows:

- ✓ The program is capable of handling both single- and multi-tone configured amplifiers. In the multi-tone configuration, the initial seed-ratio can be set to any value. It also supports inclusion of arbitrary number of ASE wavelengths.
- ✓ For each operating wavelengths, the user can select the propagating guided modes

that the associated fiber supports. This enables easy interchange between single-mode and multi-mode propagation.

- ✓ For the ODE solve, the user can select from explicit Euler method, 4<sup>th</sup> order Runge-Kutta method and 7<sup>th</sup> order Dormand-Prince method. In each case, the user can set arbitrary number of ODE steps.
- ✓ The program supports inclusion of quantum defect heating with time. The time-step can be set to any arbitrary value. Currently, the time-dependent heat equation is solved using implicit Euler method.
- ✓ Along with distributed memory parallelization, in each ODE step, for computing the integration of the coupling term and also for computing the heat source, the program utilizes shared memory parallelization techniques provided by the multi-physics finite element software library NgSolve [57, 56].
- ✓ Currently the program supports steady-state Yb-doped and Tm-doped active gain. The total dopant concentration can be set to any arbitrary value. It also supports inclusion of the Raman gain.
- ✓ The program accepts experimentally measured (thus, given) loss values. It also accepts loss as the imaginary part of the associated propagation constant.
- ✓ Amplifier configuration with any initial temperature profile for the whole fiber is supported. So, essentially we can start a particular amplifier configuration at any simulation time, provided we have the temperature profile of that fiber configuration at that time.

- ✓ The program can measure power in each mode of each operating wavelengths as well as the power of the entire wavelength. It can also measure the amplifier efficiency.
- ✓ The program supports predefined artificial refractive index gratings. Also, the grating can be set to a particular region inside the fiber-core from a list of predefined regions.

Figure 3.6: Initial stage of the simulation,

- : the associated job is done,
- : the associated job has all the resources to start the job but did not start yet,
- : the associated job is waiting for resources to start,
- solid arrow shows the flow of the ODE solver,
- dashed arrow shows the flow of the heat solver,
- and the dash-dotted arrow shows the MPI interactions.

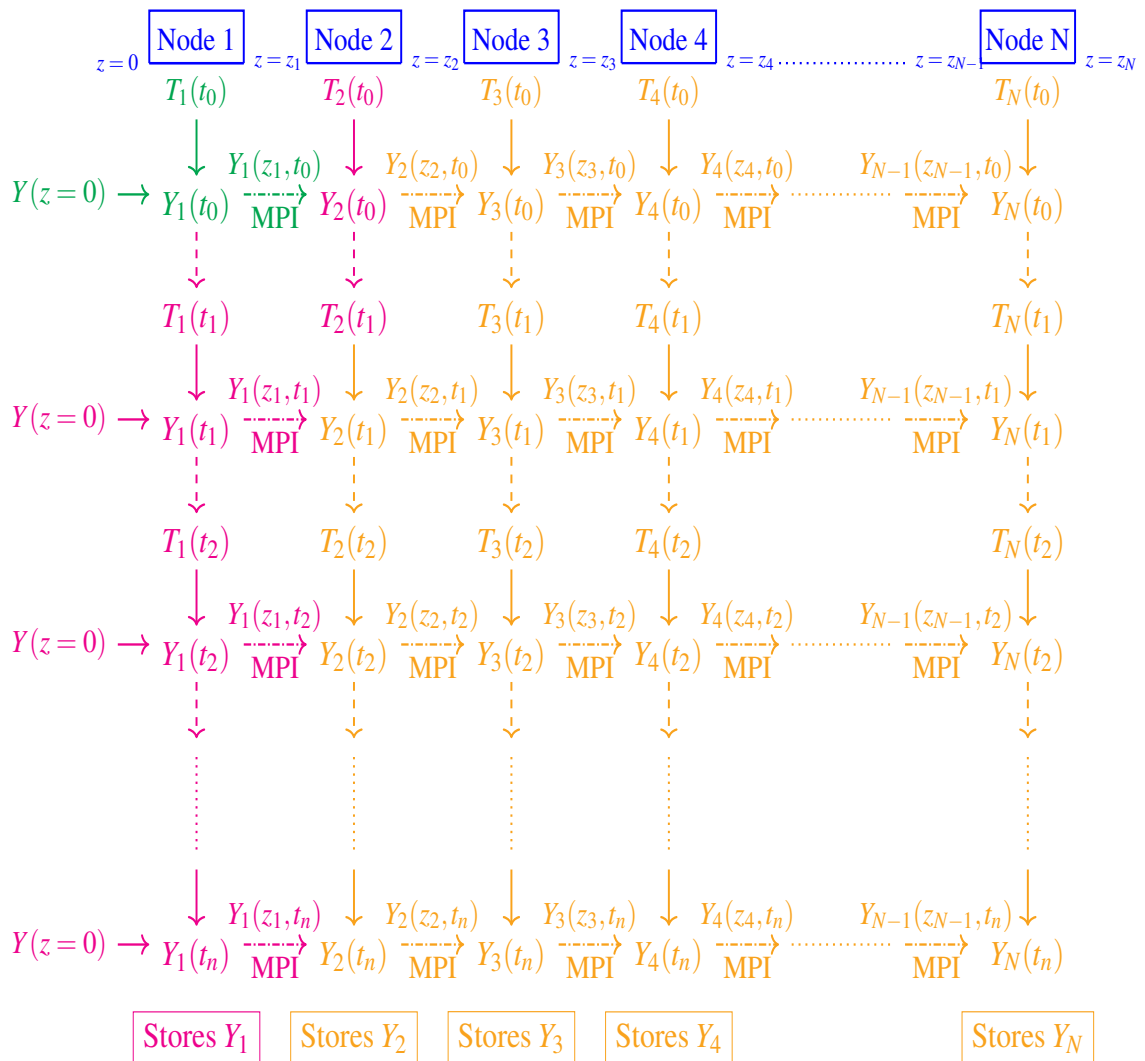


Figure 3.7: Simulation continuation,

- : the associated job is done,
- : the associated job has all the resources to start the job but did not start yet,
- : the associated job is waiting for resources to start,
- solid arrow shows the flow of the ODE solver,
- dashed arrow shows the flow of the heat solver,
- and the dash-dotted arrow shows the MPI interactions.

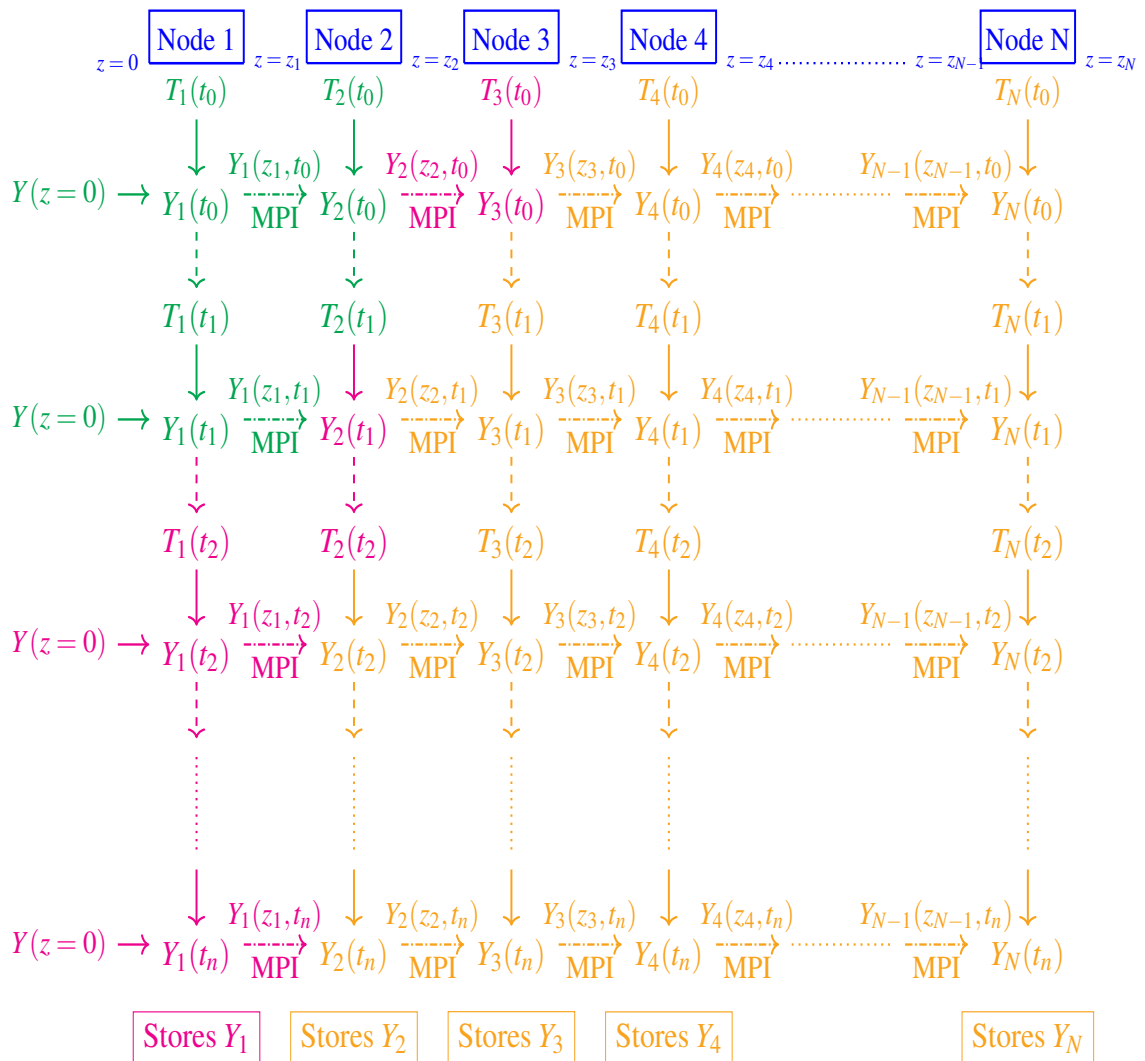


Figure 3.8: Simulation continuation,

- : the associated job is done,
- : the associated job has all the resources to start the job but did not start yet,
- : the associated job is waiting for resources to start,
- solid arrow shows the flow of the ODE solver,
- dashed arrow shows the flow of the heat solver,
- and the dash-dotted arrow shows the MPI interactions.

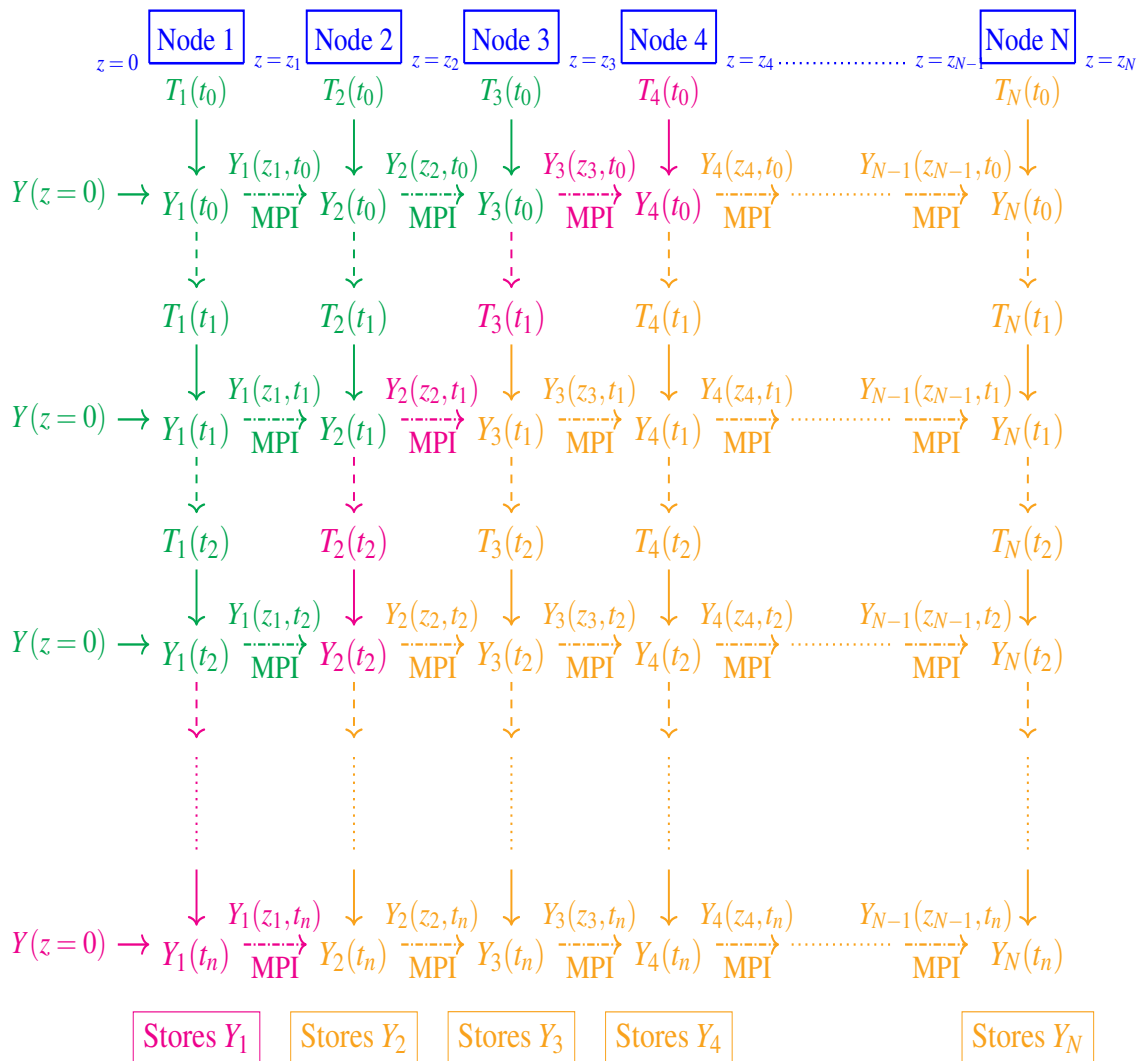


Figure 3.9: Simulation continuation,

- : the associated job is done,
- : the associated job has all the resources to start the job but did not start yet,
- : the associated job is waiting for resources to start,
- solid arrow shows the flow of the ODE solver,
- dashed arrow shows the flow of the heat solver,
- and the dash-dotted arrow shows the MPI interactions.

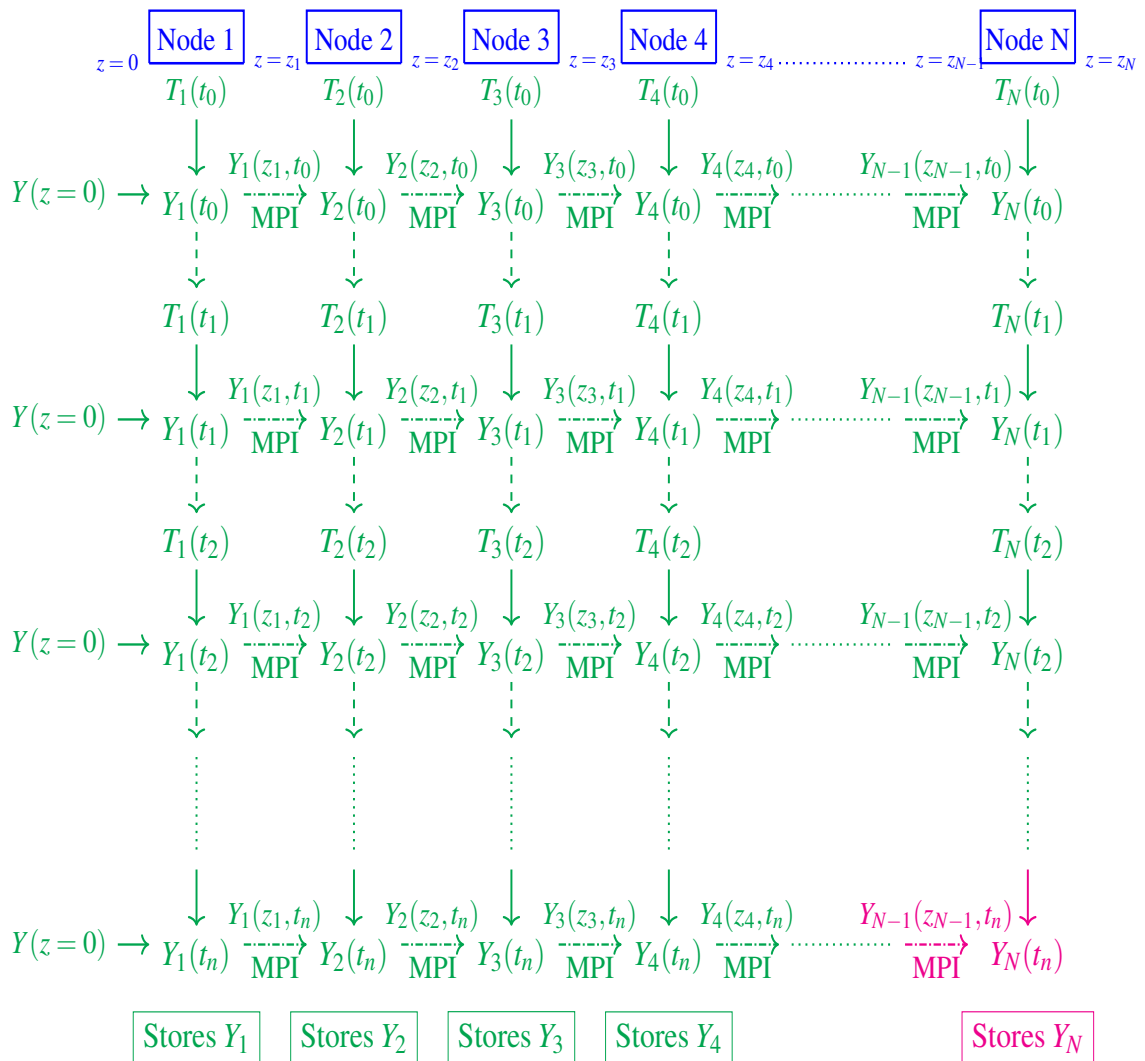
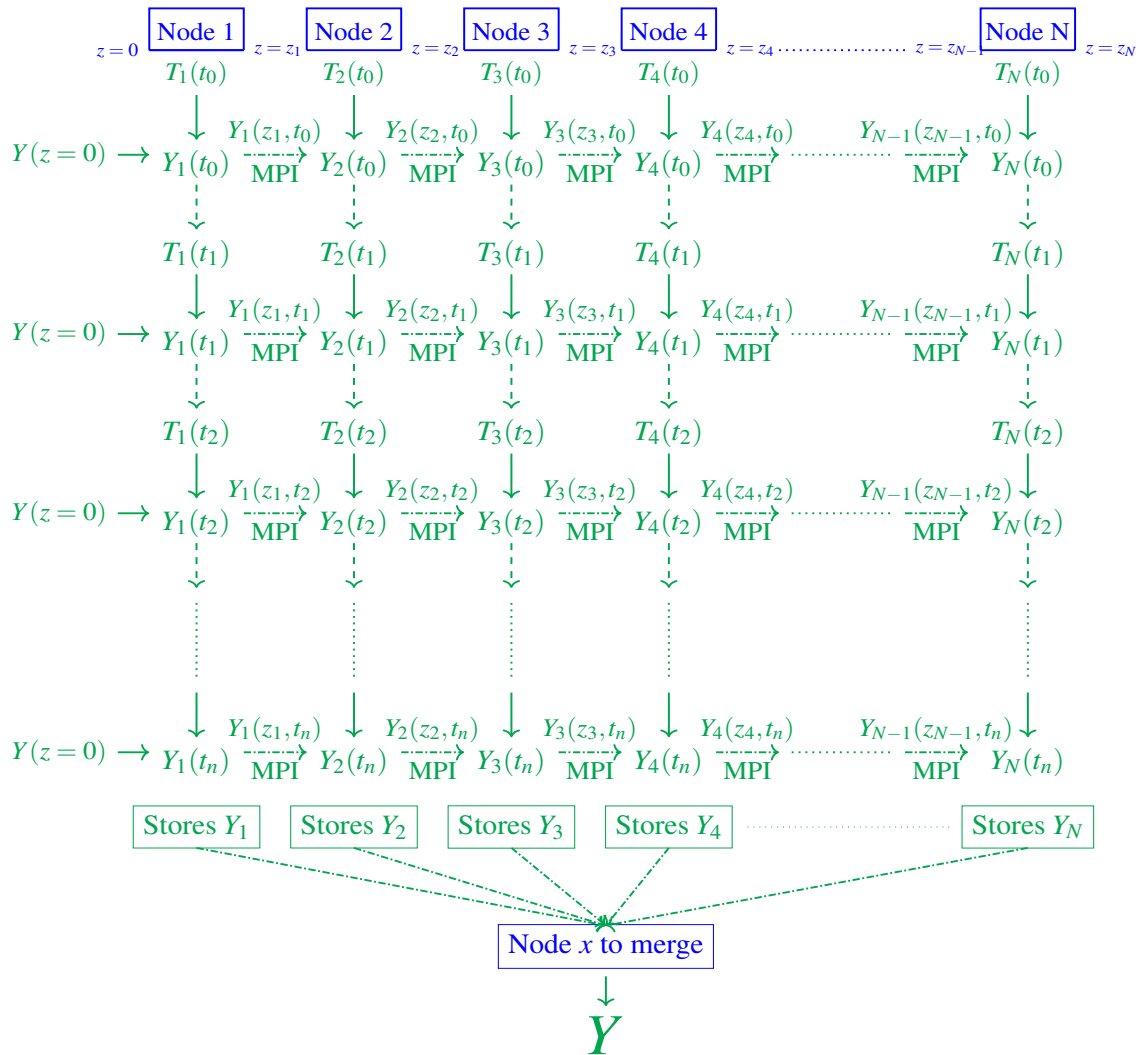




Figure 3.10: Last step of the simulation,

- : the associated job is done,
- : the associated job has all the resources to start the job but did not start yet,
- : the associated job is waiting for resources to start,
- solid arrow shows the flow of the ODE solver,
- dashed arrow shows the flow of the heat solver,
- and the dash-dotted arrow shows the MPI interactions.



## Chapter 4

### Tm- and Yb-doped Equivalent Fibers

The content of the chapter are published in [13]. In this chapter, we present the concept of a nearly equivalent short fiber, which is an artificially short fiber with nonphysical parameters that can mimic a longer physical fiber in some respects. One main advantage while solving an equivalent fiber is it can be solved using fewer steps of an ODE solver, thus providing significant reductions in computational cost.

To explain the principle behind the equivalent short fiber technique, we first consider applying an ODE solver to solve the CMT model (2.54). To solve for a 10 m long amplifier, which also is the usual length of an amplifier, and their operating wavelengths, our algorithm requires the total number of  $z$ -steps to solve the ODE (2.54) to be in between 300,000 and 450,000. Therefore, it would be extremely useful to reduce the fiber length (and hence the number of ODE steps) while still preserving the relevant physical processes in the fiber amplifier. We shall now show that this is possible to some extent using the computational scale model of an equivalent short fiber described below.

To begin with, one might consider shortening the  $z$ -domain in (2.54a) using a dimensional analysis. Also, we assume that there are only two wavelengths present in the fiber, namely, pump ( $p$ ) and signal ( $s$ ). Note that the left hand side of (2.54a) has dimension V/m

(volts per meter), and  $K_{lm}^\ell$  has units of  $\text{m}^{-1}$ . Therefore, by non-dimensionalization, one is led to believe that a shorter fiber of length  $\tilde{L} \ll L$  might, in some ways, behave similarly to the original fiber of length  $L$ , provided its coupling coefficient is magnified by  $L/\tilde{L}$ . However, not all nonlinear systems admit scale models that are perfect replicas of the original. Below we shall identify what properties of such a shorter fiber can be expected to be close to the original.

#### 4.1 A Scaled Fiber Amplifier Model

We introduce the variable change

$$\zeta(\tilde{z}) = \tilde{z}L/\tilde{L}.$$

A fiber of length  $L$ , under the variable change  $\tilde{z} = \zeta^{-1}(z) = z\tilde{L}/L$  becomes one of length  $\tilde{L}$ .

Under this variable change, (2.54) and (2.58) become

$$\frac{\tilde{L}}{L} \frac{d}{d\tilde{z}} A_l^s \left( \frac{\tilde{z}L}{\tilde{L}} \right) = \sum_{m=1}^{M_s} e^{i(\beta_m^s - \beta_l^s)\tilde{z}L/\tilde{L}} K_{lm}^s \left( I_s \left( \frac{\tilde{z}L}{\tilde{L}} \right), I_p \left( \frac{\tilde{z}L}{\tilde{L}} \right) \right) A_m^s \left( \frac{\tilde{z}L}{\tilde{L}} \right) \quad (4.1a)$$

$$\frac{\tilde{L}}{L} \frac{d}{d\tilde{z}} I_p \left( \frac{\tilde{z}L}{\tilde{L}} \right) = \langle g_p \rangle I_p \left( \frac{\tilde{z}L}{\tilde{L}} \right) \quad (4.1b)$$

for all  $0 < \tilde{z} < \tilde{L}$ . In other words, defining  $\hat{A}_l^s = A_l^s \circ \zeta$  and  $\hat{I}_p = I_p \circ \zeta$ , the above system may be rewritten as the following system on the shorter domain  $0 < \tilde{z} < \tilde{L}$  for  $\hat{Y} = [\hat{I}_p, \hat{A}_l^s]^t$ ,

$$\frac{d\hat{Y}}{d\tilde{z}} = \begin{bmatrix} (L/\tilde{L}) \langle g_p(\hat{Y}) \rangle \hat{I}_p \\ \sum_{m=1}^{M_s} e^{i(\beta_m^s - \beta_l^s)\tilde{z}L/\tilde{L}} (L/\tilde{L}) K_{lm}^s(\hat{Y}) \hat{A}_m^s \end{bmatrix}. \quad (4.2)$$

Supplemented with the same initial data at  $z = \tilde{z} = 0$ , (4.2) is exactly equivalent to (2.60), i.e.,

$$\hat{Y} = Y \circ \zeta. \quad (4.3)$$

In other words, the solution of (4.2), being the pull back of the original solution  $Y$  to the shorter domain, is a perfect replica of the original solution  $Y$ .

Unfortunately, (4.2) on  $0 < \tilde{z} < \tilde{L}$  offers no computational advantages over the original system (2.60) on  $0 < z < L$ . This is because the mode beat length of (4.2) has been reduced by a factor of  $\tilde{L}/L$  due to the variable change. So in order to solve the ODE system (4.2), keeping the same number of steps per mode beat length, the total number of steps needed to solve the system has not been reduced. This leads us to consider another mode coupling system with the same mode beat length as the original system (2.60).

Let  $\tilde{Y}(\tilde{z}) = [\tilde{I}_p(\tilde{z}), \tilde{A}_1^s(\tilde{z}), \dots, \tilde{A}_{M_s}^s(\tilde{z})]^t$  solve

$$\frac{d\tilde{Y}}{d\tilde{z}} = \begin{bmatrix} \langle (L/\tilde{L})g_p(\tilde{Y}) \rangle & 0 \\ 0 & p(\tilde{z}) \cdot (L/\tilde{L})K^s(\tilde{Y}) \end{bmatrix} \tilde{Y}, \quad 0 < \tilde{z} < \tilde{L}, \quad (4.4a)$$

$$\tilde{Y}(0) = [\tilde{I}_p(0), A_1^s(0), \dots, A_{M_s}^s(0)]^t \quad \tilde{z} = 0. \quad (4.4b)$$

Clearly, (4.4) is not the same as (4.2) due to the differences in the phase factors. Therefore, unlike the solution  $\hat{Y}$  of (4.2), the solution  $\tilde{Y}$  of (4.4) is not a perfect replica of the original solution  $Y$ . Nonetheless, we shall now proceed to argue that (4.4) is a practically useful scale model of (2.60) as it approximately preserves the power distribution from the original. Power, unlike the amplitude  $A^s$ , is the quantity that can be, and actually is, experimentally measured.

To quantitatively describe the light amplification results of the simulation, we compute

the signal and pump power, after the approximate  $Y(z) = [I_p(z), A^s(z)]$  has been computed, as follows:

$$P_s(z) = \int_{\Omega_z} I_s(x, y, z) dx dy, \quad P_p(z) = \int_{\Omega_z} I_p(z) dx dy = |\Omega_z| I_p(z). \quad (4.5)$$

Let  $P_l^s(z)$  and  $\tilde{P}_l^s(\tilde{z})$  be respectively the powers contained in the  $l^{th}$  mode of the signal at the longitudinal point  $z$  for the physical and equivalent fiber, defined by

$$\begin{aligned} P_l^s(z) &= \int_{\Omega_z} \frac{n}{\mu_0 c} |A_l^s(z) \varphi_l^s(x, y)|^2 dx dy, & 0 < z < L, \\ \tilde{P}_l^s(\tilde{z}) &= \int_{\Omega_{\tilde{z}}} \frac{n}{\mu_0 c} |\tilde{A}_l^s(\tilde{z}) \varphi_l^s(x, y)|^2 dx dy, & 0 < \tilde{z} < \tilde{L}. \end{aligned}$$

One may express these in terms of

$$\Phi_l^s = \int_{\Omega_z} \frac{n}{\mu_0 c} |\varphi_l^s|^2 dx dy,$$

as  $P_l^s(z) = |a_l^s|^2 \Phi_l^s$ , where  $a_l^s(z) = A_l^s(z) e^{i\beta_l^s z}$ .

To obtain an equation for  $P_l^s(z)$ , we may start from the second equation of the block system (2.60), or equivalently from (2.54a), which can be rewritten as

$$e^{i\beta_l^s z} dA_l^s/dz = \sum_{m=1}^{M_s} K_{lm}^s(z) e^{i\beta_m^s z} A_m^s(z).$$

Then using  $da_l^s/dz = e^{i\beta_l^s z} d_z A_l^s + i\beta_l^s a_l^s$ , we have

$$\frac{da_l^s}{dz} = i\beta_l^s a_l^s + \sum_{m=1}^{M_s} K_{lm}^s(z) a_m^s(z).$$

Using also the complex conjugate of this equation, we have

$$\frac{d|a_l^s|^2}{dz} = a_l^s \frac{d\bar{a}_l^s}{dz} + \bar{a}_l^s \frac{da_l^s}{dz} = i\beta_l^s a_l^s \bar{a}_l^s - i\beta_l^s \bar{a}_l^s a_l^s + \sum_{m=1}^{M_s} \bar{K}_{lm}^s a_l^s \bar{a}_m^s + K_{lm}^s \bar{a}_l^s a_m^s,$$

i.e.,

$$\frac{d|a_l^s|^2}{dz} = 2 \sum_{m=1}^{M_s} \Re[K_{lm}^s(Y) \bar{a}_l^s a_m^s],$$

for all  $l = 1, \dots, M_s$ , or equivalently,

$$\frac{dP_l^s}{dz} = 2K_{ll}^s(Y)P_l^s + \rho_l^s(Y), \quad (4.6)$$

where

$$\rho_l^s(Y) = 2\Phi_l^s \sum_{\substack{m=1 \\ m \neq l}}^{M_s} \Re[K_{lm}^s(Y) \bar{a}_l^s a_m^s], \quad (4.7)$$

for  $l = 1, \dots, M_s$ .

To the system (4.6), let us also add the pump power using the index  $l = 0$ , i.e., let  $P(z) \equiv [P_p(z), P_1^s(z), \dots, P_{M_s}^s(z)]$  as defined in (4.5). Then integrating (2.58), we obtain  $dP_0/dz = \langle g_p \rangle P_0$ . All together, we have thus obtained an equation for  $P_l$  for all  $l = 0, 1, \dots, M_s$ ,

$$\frac{dP}{dz} = \begin{bmatrix} \langle g_p(Y) \rangle & 0 \\ 0 & 2\text{diag}[K(Y)] \end{bmatrix} P + \begin{bmatrix} 0 \\ \rho(Y) \end{bmatrix}, \quad (4.8)$$

where  $P = [P_0, P_1, \dots, P_{M_s}]^t$  and  $\text{diag}[\cdot]$  denotes the diagonal part of a matrix.

To understand the motivation for the remaining arguments, we now highlight an observation concerning (4.8). A scale model providing a perfect replica of the original power distribution is easy to obtain if the system (4.8) were an autonomous system: indeed, if

there exists a function  $F$  of  $P$  alone such that  $dP/dz = F(P)$ , then by merely scaling  $F$  by  $L/\tilde{L}$ , we obtain an equivalent system that provides perfect replicas of the original power distribution on the shorter fiber of length  $\tilde{L}$ . However (4.8) is not autonomous, in general. Yet, for practical fibers, our numerical experience suggests that (4.8) behaves almost like an autonomous system. Therefore our strategy now is to view (4.8) as a perturbation of an autonomous system.

Of particular interest is the fact that if the fiber amplifier was robustly single-mode ( $M_s = 1$  for the laser signal), then the governing system (4.8) would be autonomous. This can be achieved by not using a LMA amplifier, but one of a smaller fiber core size and/or a lower numerical aperture (NA) such that the fiber core can only support only one guided core mode, the fundamental mode (indexed by  $m = 1$ ), at the signal wavelength. However, even with a LMA fiber, if one were to account for fiber bending effects, which cause the higher-order core modes (indexed by  $1 < m \leq M_s$ ) to leak into the cladding region more so than for the fundamental mode, then the fiber would operate nearly as a single-mode fiber. Actual fiber amplifiers are almost always wrapped on a spool rather than stretched out straight, thus ensuring this fiber bending effect. This provides us with greater confidence of autonomous system-like behavior, even in real-world implementations of fiber laser amplifier systems.

Recall from (2.60) that  $K_{lm}^s$  is defined using  $g_s(I_s, I_p)$ , where  $I_s$  takes the form in (2.57). We define the following perturbation of  $I_s$ ,

$$\mathcal{I}_s(P) = \sum_{m=1}^{M_s} \frac{n}{\mu_0 c} |a_m^s \varphi_m^s|^2 = \sum_{m=1}^{M_s} \frac{n}{\mu_0 c \Phi_m^s} P_m^s |\varphi_m^s|^2.$$

It seems difficult to characterize when  $I_s - \mathcal{I}_s$  is small *a priori* (as it depends, e.g., on the localization and orthogonality of the specific fiber modes) but after a CMT calculation, we

may check if this difference is small *a posteriori*. Deferring for the moment the matter of the size of  $I_s - \mathcal{I}_s$ , let us proceed to define  $\gamma_\ell(P) = g_\ell(\mathcal{I}_s(P), I_p) = g_\ell(\mathcal{I}_s(P), P_0/|\omega_z|)$ , for  $\ell \in \{s, p\}$ . They represent the gain functions obtained by replacing  $I_s$  by  $\mathcal{I}_s$ . The new gain functions in turn prompt the definition of a new mode coupling coefficient: instead of the coupling term in (2.60), we now consider

$$\kappa_{lm}(P) = \frac{k_s}{2\beta_l^s} \int_{\Omega_z} \gamma_s(P) n(x, y) \varphi_m^s(x, y) \overline{\varphi_l^s(x, y)} dx dy.$$

for all  $l, m = 1, \dots, M_s$ . Additionally let

$$\kappa_{00}(P) = \frac{1}{2} \langle \gamma_p(P) \rangle P_0,$$

and  $\kappa_{0l} = \kappa_{l0} = 0$ , for all  $l = 1, \dots, M$ . We may now view these  $\kappa_{lm}$  as entries of an  $(M+1) \times (M+1)$  matrix, using which (4.8) can be expressed as

$$\frac{dP}{dz} = 2\kappa(P)P + \eta \tag{4.9}$$

where  $\eta \in \mathbb{R}^{M+1}$  is defined by

$$\eta(z) = \begin{bmatrix} \langle g_p(Y) - \gamma_p(P) \rangle & 0 \\ 0 & 2 \text{diag}[K(Y) - \kappa(P)] \end{bmatrix} P + \begin{bmatrix} 0 \\ \rho(Y) \end{bmatrix}.$$

We view  $\eta$  as a function of  $z$ , i.e.,  $\eta : [0, L] \rightarrow \mathbb{R}^{M+1}$ . The  $z$ -dependence is clear once we express the  $z$ -dependence of the solution  $Y \equiv Y(z)$  and power  $P \equiv P(z)$ . Equation (4.9) shows that power is governed by a perturbation of an autonomous system whenever  $\eta$  is small enough to be viewed as a perturbation.



Returning to consider (4.4), we define analogous quantities for the short fiber, namely

$$\tilde{a}_l^s(z) = \tilde{A}_l^s(z)e^{i\beta_l^s z}, \quad \tilde{P}_0 = \int_{\Omega_z} \tilde{I}_p \, dx dy, \quad \tilde{P}_l = |\tilde{a}_l^s|^2 \Phi_l^s,$$

for  $l = 1, \dots, M_s$ . Then we may repeat the above arguments starting from (4.4) to obtain the following analogue of (4.9).

$$\frac{d\tilde{P}}{d\tilde{z}} = 2\frac{L}{\tilde{L}}\kappa(\tilde{P})\tilde{P} + \tilde{\eta}, \quad (4.10)$$

where  $\tilde{\eta} : [0, \tilde{L}] \rightarrow \mathbb{R}^{M+1}$  is now given by

$$\tilde{\eta} = \begin{bmatrix} \langle g_p(\tilde{Y}) - \gamma_p(\tilde{P}) \rangle & 0 \\ 0 & 2 \text{diag}[K(\tilde{Y}) - \kappa(\tilde{P})] \end{bmatrix} \tilde{P} + \begin{bmatrix} 0 \\ \rho(\tilde{Y}) \end{bmatrix}.$$

Note that  $\rho(\tilde{Y})$  is defined by (4.7) after replacing not only  $Y$  by  $\tilde{Y}$ , but also  $a_l^s$  (which depends on  $Y$ ) by  $\tilde{a}_l^s$  (which depends on  $\tilde{Y}$ ).

To conclude this analysis, it now suffices to compare (4.10) and (4.9). Applying the change of variable  $\zeta$  to (4.9), we get

$$\frac{d}{d\tilde{z}}(P \circ \zeta) = 2\frac{L}{\tilde{L}}\kappa(P \circ \zeta)P \circ \zeta + \frac{L}{\tilde{L}}\eta \circ \zeta. \quad (4.11)$$

Comparing (4.10) and (4.11) we see that when  $\eta$  and  $\tilde{\eta}$  are negligibly small compared to the other terms,  $P_l \circ \zeta$  and  $\tilde{P}_l$  solve approximately the same equation, and consequently

$$P \circ \zeta \approx \tilde{P}. \quad (4.12)$$

We summarize this discussion as follows.

The system (4.4) is an equivalent short fiber model of (2.60) in the sense that the power  $P_l^s$  contained in the  $l^{\text{th}}$  mode is approximately preserved from the original fiber model (2.60) through a change of variable, under the above assumptions.

## 4.2 Simulation Results

Thulium (Tm)-doped fiber amplifiers [29, 30] can operate in eye-safe laser wavelengths (larger than  $1.4 \mu\text{m}$ ) and can reach an atmospheric transmission window ( $2.1\text{--}2.2 \mu\text{m}$ ). There are efficient high-power Light Emitting Diode (LED)s that operate in the range of  $0.79\text{--}0.793 \mu\text{m}$ , which is a peak absorption bandwidth for Tm-doped fibers. Cross-relaxations and upconversions occur in Tm-doped amplifiers. Even though Tm-doped fibers usually have better TMI suppression compared to other rare-earth ion doped fibers [59], ytterbium (Yb)-doped fiber amplifiers have also emerged as excellent candidates for high power operation due to their high-efficiencies and low amplified spontaneous emission gain. Yb-doped amplifiers are usually pumped at  $976 \text{ nm}$  and can lase around  $1064 \text{ nm}$  very efficiently.

### 4.2.1 Computation With Physical Fiber

We report the results obtained from simulation of the CMT model for two  $10 \text{ m}$  long fibers, one doped with Yb and the other with Tm. The fiber parameters are collected from data sheets of commercially available exemplars of these fibers (specifically Nufern<sup>TM</sup> fibers – see [nufern.com](http://nufern.com)). All parameters used for the simulation of both the fibers are reported in Tables 4.1 and 4.2.

Parameter	Value	Units	Parameter	Value	Units
$\lambda_p = 2\pi c/\omega_p$	$9.76 \times 10^{-7}$	m	$\lambda_s = 2\pi c/\omega_s$	$1.064 \times 10^{-6}$	m
$\sigma^{\text{abs}}(\omega_p)$	$1.429 \times 10^{-24}$	m <sup>2</sup> /ion	$\sigma^{\text{ems}}(\omega_p)$	$1.776 \times 10^{-24}$	m <sup>2</sup> /ion
$\sigma^{\text{abs}}(\omega_s)$	$6 \times 10^{-27}$	m <sup>2</sup> /ion	$\sigma^{\text{ems}}(\omega_s)$	$3.58 \times 10^{-25}$	m <sup>2</sup> /ion
$N_{\text{total}}$	$3 \times 10^{26}$	ions/m <sup>3</sup>	$\tau$	$8 \times 10^{-4}$	s
$n_{\text{core}}$	1.450971	–	NA	0.06	–
$r_{\text{core}}$	$1.25 \times 10^{-5}$	m	$r_{\text{clad}}$	$2 \times 10^{-4}$	m
$P_p^0$	1000	W	$P_s^0$	25	W

Table 4.1: Parameters used in Yb-doped fiber simulation

Parameter	Value	Units	Parameter	Value	Units
$\lambda_p = 2\pi c/\omega_p$	$7.93 \times 10^{-7}$	m	$\lambda_s = 2\pi c/\omega_s$	$2.110 \times 10^{-6}$	m
$\sigma^{\text{abs}}(\omega_p)$	$4.4686 \times 10^{-25}$	m <sup>2</sup> /ion	$\sigma^{\text{ems}}(\omega_p)$	0	m <sup>2</sup> /ion
$\sigma^{\text{abs}}(\omega_s)$	$1.7423 \times 10^{-27}$	m <sup>2</sup> /ion	$\sigma^{\text{ems}}(\omega_s)$	$1.17397 \times 10^{-25}$	m <sup>2</sup> /ion
$\tau_{10}$	$6.2232 \times 10^{-3}$	s	$\tau_{20}$	$5.5179 \times 10^{-3}$	s
$\tau_{21}$	$2.5707 \times 10^{-1}$	s	$\tau_{30}$	$1.3949 \times 10^{-3}$	s
$\tau_{31}$	$1.7033 \times 10^{-2}$	s	$\tau_{32}$	$6.8446 \times 10^{-2}$	s
$\Gamma_1$	$2.59288 \times 10^3$	Hz	$\Gamma_2$	$2.92755 \times 10^7$	Hz
$\Gamma_3$	$8.05943 \times 10^4$	Hz	–	–	–
$N_{\text{total}}$	$3 \times 10^{26}$	ions/m <sup>3</sup>	$\kappa_R$	$1.17 \times 10^{-21}$	m <sup>3</sup>
$n_{\text{core}}$	1.439994	–	NA	0.1	–
$r_{\text{core}}$	$1.25 \times 10^{-5}$	m	$r_{\text{clad}}$	$2 \times 10^{-4}$	m
$P_p^0$	1100	W	$P_s^0$	30	W

Table 4.2: Parameters used in Tm-doped fiber simulation

We solve the CMT system (2.60) using the classical 4<sup>th</sup> order explicit Runge-Kutta method (in complex arithmetic). The phase terms  $\phi_{lm}^s(z) = e^{i(\beta_m^s - \beta_l^s)z}$  in the ODE system oscillate at a wavelength not smaller than the so-called *mode beat length*

$$\frac{2\pi}{\max_{l,m=1,\dots,M_s} |\beta_l^s - \beta_m^s|}. \quad (4.13)$$

An ODE solver applied to solve (2.60) must take sufficient number of steps per mode beat length to capture the effect of these oscillations in the solution. Prevailing theories [47] point to the potential importance of the mode beating term in thermal effects, so we must be careful to treat these oscillations with the needed accuracy if the model is to be extendable to incorporate thermal effects in the future. In all our simulations, we used 50 ODE steps per mode beat length.

Before running the ODE solver, we precompute the propagation constants  $\beta_j$ , the mode beat length, and of course, the modes. For step-index fibers, we can compute the modes  $\phi_l^s$  exactly in closed form (see [2, 53]) as described in chapter 2, section 2.3.1. For the particular case of the Tm parameters in Table 4.2, we find that the fiber only has the LP<sub>01</sub> and LP<sub>11</sub> modes, while for the Yb fiber with the parameters set in Table 4.1, we found four modes LP<sub>01</sub>, LP<sub>11</sub>, LP<sub>21</sub> and LP<sub>02</sub>. In our simulation the fiber geometry was meshed using finite elements (with curved elements at the cladding boundary and at the core-cladding interface) and the relevant LP modes were interpolated into the degree  $p$  Lagrange finite element space based on the mesh. Integration involving finite element functions is broken into a sum over integrals over all mesh elements and a sufficiently high quadrature rule is used to approximate an element integral. This is how we approximate all required integrals, such as in the computation of the coupling coefficient (2.54a), as well as in power

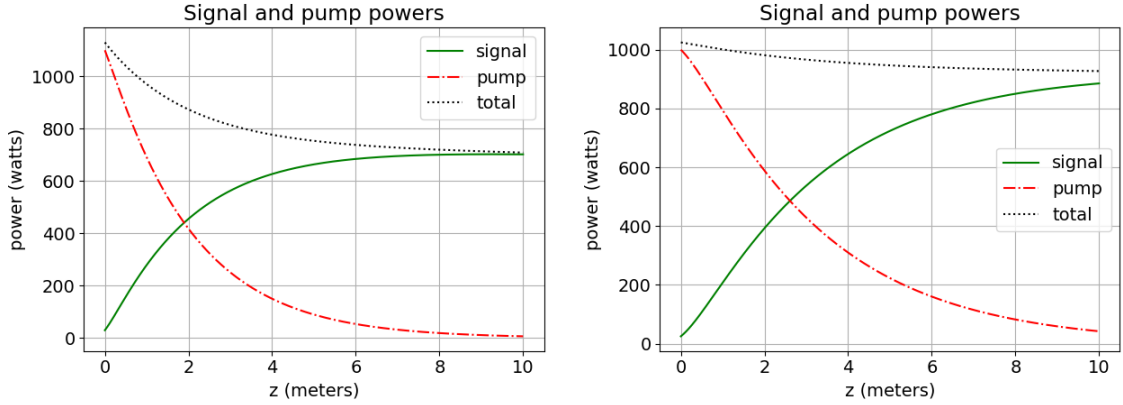


Figure 4.1: The simulated distribution of powers along the Tm-doped (left) and the Yb-doped (right) fiber amplifier. The pump power  $P_p$  and the signal power  $P_s$ , as defined in (4.5), are shown. The black dotted line plots  $P_s + P_p$ .

computations. Note that each step of the multi-stage ODE solver requires many such integrations.

The initial condition  $Y(0)$  is set so that the entire signal power is fed into the  $LP_{01}$  mode at the inlet  $z = 0$ . Initial pump power  $P_p(z = 0)$  was set 1000 W for the Yb case and 1100 W for the Tm case. Figure 4.1 shows the distribution of the computed  $P_s$  and  $P_p$  (marked “signal” and “pump” there) for the Tm and Yb-doped fibers. The energy transfer from the pump light to the signal light is clearly evident. We used  $p = 5$  Lagrange elements for these plots. The use of 50 steps per mode beat length implies that the Yb case required 421,014 RK4 steps, while the Tm case required 302,340 steps of the ODE solver to cover the 10 m fiber.

### 4.3 Computations of Equivalent Fibers

In this section, we perform extensive numerical experiments to verify the practical utility of the equivalent fiber concept introduced in Section 4.1. We shall compare the relative

differences in the powers obtained from the original fiber and its equivalent short fiber for various settings to gauge the practical effectiveness of the approximation (4.12). In Subsections 4.3.1 and 4.3.2, we show a way to understand the equivalent short fiber as a fiber with artificial parameters (with values not physically realizable) for the Tm and Yb cases, respectively.

### 4.3.1 Realizing the equivalent short fiber for the Tm-doped case

The equations of the equivalent short fiber, namely (4.4), can be realized for a dopant medium if we can find a set of “artificial” parameters that would scale the original  $g_p$  and the original  $K^\ell$  by  $L/\tilde{L}$ . In view of (2.54a), this effect is achieved by scaling the original  $g_\ell$  by  $L/\tilde{L}$ . Now consider the expressions for  $g_\ell$  for Tm-doped fiber, given in (2.18) and (2.19). Clearly, in view of these expressions,  $g_\ell$  will be scaled by  $L/\tilde{L}$  if all the ion populations  $N_i$  are so scaled.

This observation, in turn, leads us to consider the expressions for  $N_i$  we derived in (2.17).

Let

$$\tilde{N}_{\text{total}} = \frac{L}{\tilde{L}} N_{\text{total}}, \quad \tilde{\kappa}_R = \frac{\tilde{L}}{L} \kappa_R.$$

The value of the expression for  $N_0$  in (2.17a) will be scaled by  $L/\tilde{L}$  if we replace  $\kappa_R$  by  $\tilde{\kappa}_R$  and  $N_{\text{total}}$  by  $\tilde{N}_{\text{total}}$ , i.e., (2.17a) implies

$$\begin{aligned} \frac{L}{\tilde{L}} N_0 = & \frac{\gamma_0 \tilde{\kappa}_R \tilde{N}_{\text{total}} - \gamma_1 (1 + \gamma_2 + \gamma_3) - 1}{2 \tilde{\kappa}_R (\gamma_0 + \gamma_1 \gamma_4)} \\ & + \frac{\sqrt{(1 - \gamma_0 \tilde{\kappa}_R \tilde{N}_{\text{total}} + \gamma_1 (1 + \gamma_2 + \gamma_3))^2 + 4(\gamma_0 + \gamma_1 \gamma_4) \tilde{\kappa}_R \tilde{N}_{\text{total}}}}{2 \tilde{\kappa}_R (\gamma_0 + \gamma_1 \gamma_4)}. \end{aligned} \quad (4.14)$$

Let  $\tilde{N}_0 = LN_0/\tilde{N}_0$ , the left hand side above. Proceeding to analyze the expressions in (2.17b), we find that the same change in  $\kappa_R$  and  $N_{\text{total}}$ , and the consequent change in  $N_0$  to  $\tilde{N}_0$

per (4.14), also scales all other  $N_i$  by  $L/\tilde{L}$ , i.e.,

$$\frac{L}{\tilde{L}}N_1 = \frac{(\gamma_3 + \gamma_4 \tilde{\kappa}_R \tilde{N}_0) \gamma_1 \tilde{N}_0}{1 + \gamma_0 \tilde{\kappa}_R \tilde{N}_0}, \quad \frac{L}{\tilde{L}}N_2 = \frac{\gamma_2 \gamma_1 \tilde{N}_0}{1 + \gamma_0 \tilde{\kappa}_R \tilde{N}_0}, \quad \frac{L}{\tilde{L}}N_3 = \frac{\gamma_1 \tilde{N}_0}{1 + \gamma_0 \tilde{\kappa}_R \tilde{N}_0}.$$

Therefore, all the ion populations  $N_i$  are scaled by  $L/\tilde{L}$ , and so are  $g_s$  and  $g_p$ . We have thus arrived at our main observation of this subsection:

A short fiber of length  $\tilde{L}$  is equivalent to a Tm-doped fiber of length  $L$  if the fiber's original parameters  $N_{\text{total}}$  and  $\kappa_R$  are changed to  $\tilde{N}_{\text{total}} = LN_{\text{total}}/\tilde{L}$  and  $\tilde{\kappa}_R = \tilde{L}\kappa_R/L$ , respectively, i.e., this change realizes (4.4).

To see how this idea works in practice, we consider two scenarios, both with an equivalent short fiber of  $\tilde{L} = 0.1$  m representing the 10 m long Tm fiber we simulated in Figure 4.1. (All parameters are as in Table 4.2 except for  $N_{\text{total}}$  and  $\kappa_R$ , which were modified for the equivalent fiber as stated above.) In the first scenario, 100% of the input signal power is carried in the  $\text{LP}_{01}$  mode at the inlet (the same setting as in the computation reported in Figure 4.1). In the left panel of Figure 4.2, we find that the plots of the computed powers for the equivalent short fiber and the real fiber are virtually identical. Even though the difference between them appear to be zero visually, we have quantified this difference in the bottom left plot of Figure 4.2: since the domains of the two power functions to be compared are different, we pull back the original powers to the shorter domain and plot  $P_l \circ \zeta - \tilde{P}_l$  (for the two modes,  $\text{LP}_{01}$  and  $\text{LP}_{11}$ ) on the shorter domain. Clearly, from the scale of the plot, the absolute differences are found to be of the order of  $10^{-9}$ , so indeed the differences between the two sets of power curves are negligible. The practical value of the equivalent short fiber calculation lies in the fact that the artificially short fiber provides 100x computational speed up compared to the real-length fiber calculation than the real-length

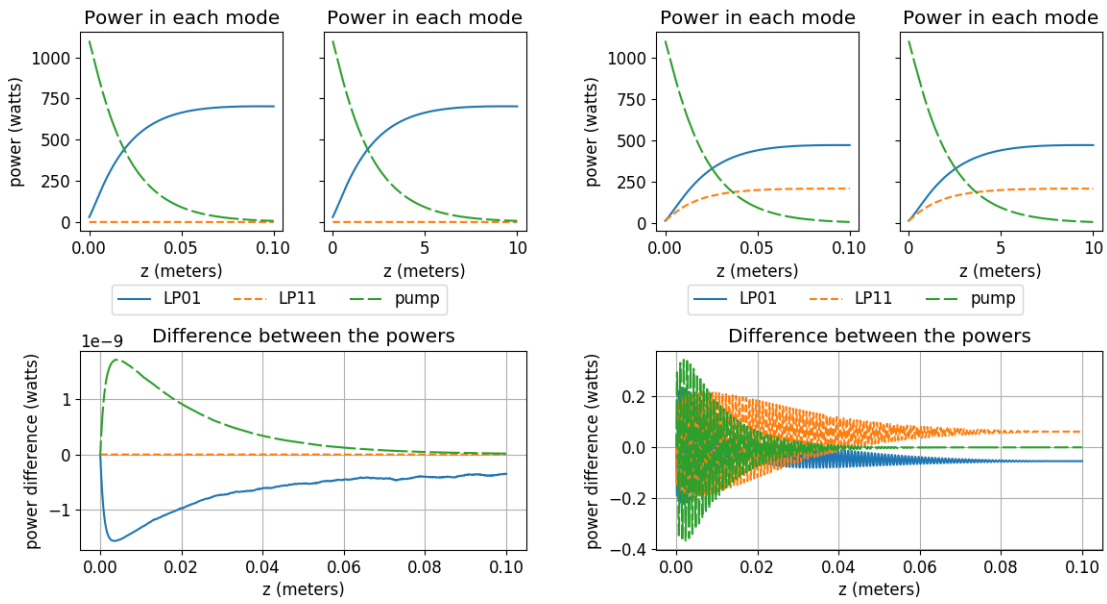


Figure 4.2: A Tm-doped amplifier comparison between a real-length fiber and its equivalent short counterpart. The upper left panel shows the case where the input signal power was wholly contained in the  $LP_{01}$  mode, while the upper right panel shows the case where it was equally distributed between the two modes- $LP_{01}$ , and  $LP_{11}$ . The power difference along the fiber is plotted below for each case. The oscillations we see is due to the phase difference between the physical and equivalent fiber model.



fiber calculation of Figure 4.1.

In the second scenario, the total input power of 30 W is distributed equally between the LP<sub>01</sub> and LP<sub>11</sub> modes. From the top right panel of Figure 4.2, we find that LP<sub>01</sub> mode amplifies more than the LP<sub>11</sub> mode. Moreover, as in the left panel, the results from the real and equivalent short fiber are visually indistinguishable. However, a more careful examination of the difference  $P_l \circ \zeta - \tilde{P}_l$  in the bottom right plot shows that maximal absolute power differences are about 0.3 near the inlet of the fiber. Although this is many fold larger than the first scenario, the relative power error of  $3 \times 10^{-4}$  is still quite small enough to make the equivalent short fiber a useful practical tool. Note that the difference  $P_l \circ \zeta - \tilde{P}_l$  is now highly oscillatory, due to the interactions between the two modes.

### 4.3.2 Realizing the equivalent short fiber for the Yb-doped case

I also made a similar investigation for the Yb-doped amplifier case, and likewise found that the equivalent short fiber concept is highly practical, leading to very small relative errors in the power levels. This is not surprising given that the Yb ion gain dynamics are much simpler than they are for the Tm-doped amplifier case. The following conclusion can be arrived at easily proceeding similarly as in Subsection 4.3.1.

A short fiber of length  $\tilde{L}$  is equivalent to a Yb-doped fiber of length  $L$  if the fiber's original parameter  $N_{\text{total}}$  is changed to  $\tilde{N}_{\text{total}} = LN_{\text{total}}/\tilde{L}$ , i.e., this change realizes (4.4).

Figure 4.3 gives some indication of the practical performance of this equivalent short fiber. As in the experiments for the Tm-fiber reported in Figure 4.2, here we consider two scenarios, the first where all input signal power is given to the LP<sub>01</sub> mode, and the second where the input power is distributed equally to the four core guided modes of the fiber (25% each). The upper left panel in Figure 4.3 shows the former, while the upper right

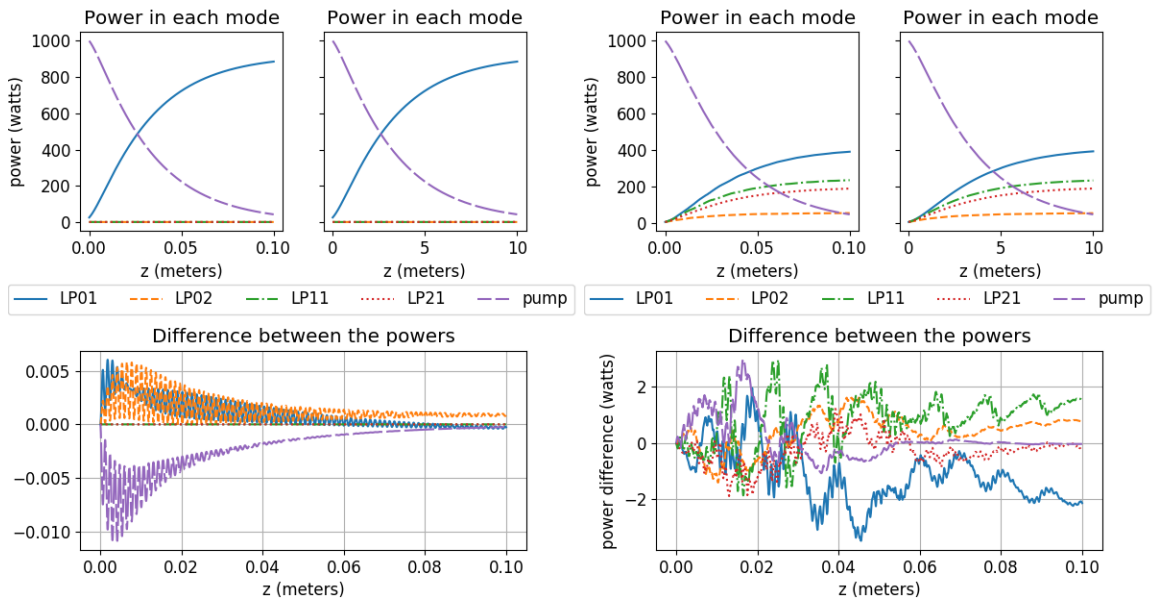


Figure 4.3: A Yb-doped amplifier comparison between a real-length fiber and its equivalent short counterpart. The upper left panel shows the case where the input signal power was wholly contained in the  $LP_{01}$  mode, while the upper right panel shows the case where it was equally distributed between the four modes- $LP_{01}$ ,  $LP_{21}$ , and  $LP_{02}$ . The power difference along the fiber is plotted below for each case. The oscillations we see is due to the phase difference between the physical and equivalent fiber model.

panel shows the latter. The equivalent fiber is less faithful in the latter case, but the scale of the errors observed in the bottom plots in both cases are well within the acceptable error ranges in engineering practice. (Laboratory power measurement uncertainties tend to be about  $\pm 5\%$ .)

### 4.3.3 Increase of error with respect to some parameters

We want to understand how relative power differences between the equivalent and real fiber vary with respect to two important input parameters  $P_p^0$  and the short fiber length  $\tilde{L}$ . We consider both the Tm and Yb fibers, holding the original fiber length  $L$  fixed to 10 m.

The solutions of the original and equivalent fiber models vary as initial conditions are changed. Therefore to compare one with the other in the *worst case* scenario, we take the maximum of the power error measures over the set

$$\mathcal{A} = \left\{ \alpha \in \mathbb{C}^M : \int_{\Omega_z} I_s(x, y, 0, \alpha) dx dy = P_s^0 \right\},$$

i.e., the set  $\mathcal{A}$  is the set of all input distributions yielding the same initial signal power  $P_s^0$ , which is set for Tm and Yb fiber per Tables 4.2 and 4.1, respectively. The initial pump power  $P_p^0$  is varied in the range 1000–5000 W (thus providing a corresponding range of initial values for the  $I_p$ -component in the model). We solve the full CMT model and the equivalent short fiber model, not only for this range of  $P_p^0$ , but also for decreasing values of the short fiber length  $\tilde{L}$ . The following quantity is then computed across all such solutions:

$$\varepsilon^\ell(P_p^0, \tilde{L}) = \max_{A^0 \in \mathcal{A}} \frac{\max_{l=0,1,\dots,M_\ell} \max_{0 \leq z \leq L} |(P_l - \tilde{P}_l \circ \zeta^{-1})(z)|}{\max_{l=0,1,\dots,M_\ell} \max_{0 \leq z \leq L} |P_l(z)|}. \quad (4.15)$$

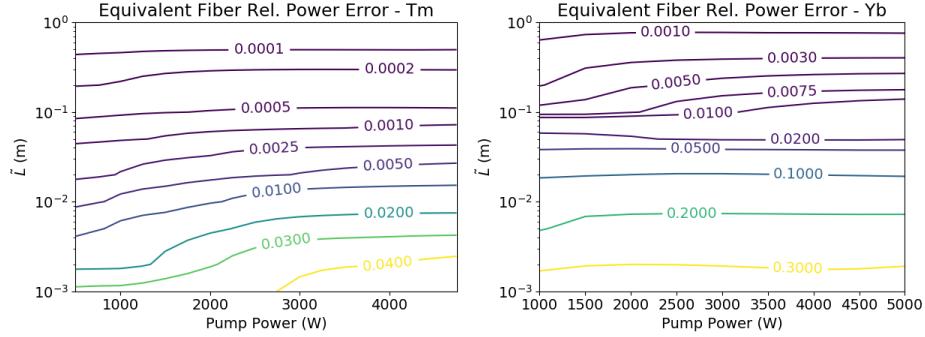


Figure 4.4: Maximal relative power differences between a 10 m long real fiber and equivalent short fibers of various lengths  $\tilde{L}$ , for various initial pump powers  $P_p^0$ . The Tm case is shown on the left and Yb case on the right.

Thus  $\varepsilon$  represents the maximal possible power deviations between the equivalent and original models over all input signal distributions and over all mode components, as a function of initial pump power  $P_p^0$  and the fictitious length  $\tilde{L}$ . Values of  $\varepsilon^\ell$  will thus inform us of the ranges of  $P_p^0$  and  $\tilde{L}$  where the equivalent short fiber is more useful for wavelength  $\ell$ .

To practically compute  $\varepsilon^\ell$ , we replace the maximum over the infinite set  $\mathcal{A}$  by a computable maximum over a finite set obtained by assigning each mode component all possible values from 0 to 100% in 10% increments (while constraining the total signal power to  $P_s^0$ ). In the case of the 2-mode thulium fiber, this resulted in 11 input power distributions, while for the ytterbium-doped fiber having 4 modes, 286 distributions were required. The maximum over  $z$  in (4.15) is replaced by the maximum over the points where ODE solver traversed. We used polynomial degree  $p = 5$  for the finite element approximation of modes and the 7-stage Dormand-Prince Runge Kutta method for solving the ODE system. Collecting data from hundreds of simulations, we then plot  $\varepsilon^\ell$  in a two-dimensional grid of  $P_p^0$  and  $\tilde{L}$  values. The resulting contour plots of the function  $\varepsilon^\ell$  are given in Figure 4.4 for Yb and Tm fibers, for a range of  $P_p^0$  and  $\tilde{L}$  values. We find that relative error  $\varepsilon^\ell$  varies mildly with respect to  $P_p^0$  for any fixed  $\tilde{L}$ , indicating that the absolute error in the powers increases

more or less linearly as  $P_p^0$  is increased. Looking vertically at the plots of Figure 4.4, we find that holding  $P_p^0$  fixed, there are significant variations in  $\varepsilon^\ell$  with respect to  $\tilde{L}$ . The errors definitively increase as  $\tilde{L}$  decrease. Figure 4.4 clearly indicates that excessively short equivalent fiber lengths are not recommendable.

## Chapter 5

### TMI in Tm-doped Single-, and Two-tone Fibers

Primarily heat deposition in an optical fiber amplifier takes place through quantum defect heating. In laser science, the term "quantum defect" refers to the fact that the energy of a pump photon is generally higher than that of a signal photon (photon of the output radiation). Laser amplification converts pump photons into signal photons, and then the left-over energy becomes heat. As described previously, the TMI is believed to occur due to a *temperature induced* refractive index grating [33]. So, for the full fiber laser amplifier simulations it is critical to model the heat source and then compute the temperature sufficiently accurately. In the following sections we shall discuss the TMI in a little more detail, solve the field equation (3.1a) coupled with the heat equation (2.26), and present TMI thresholds under a few different circumstances.

#### 5.1 Transverse Mode Instability

The first experimental observation of TMI was reported in [14, 15]. The impression that TMI could be caused by thermal effects was also supported by some experiments [25]. TMI experiments are mostly done using Yb-doped fibers, but recently it is predicted and observed in Tm-doped amplifiers [59, 16]. All of these experiments point to the conclu-

sion that TMI is indeed a thermo-optical effect and that once a certain heat threshold has been reached, the onset of TMI can be expected. TMI is even predicted for Raman amplifiers [46] as well.

In theory, one of the known optical elements that allows transfer of energy between transverse modes is a long period bragg grating or LPBG. Also, an energy transfer between modes can only be a phase matched process [33]. When an optical fiber deposits heat, the thermal changes induce a dynamic grating which consequently influences the modal interference pattern [62], in other words, triggers TMI. We shall talk more about LPBG in chapter 7.

In the following section we shall discuss the entities that influence the heat-load in the fiber laser system. One of the main parameters is the input pump power which introduces a grating in the refractive index by impacting the temperature in the fiber. The following sections will explore this in more detail.

## 5.2 Numerical formulation of the heat equation

In our simulations, the fiber geometry was discretized using 5<sup>th</sup> order Lagrange finite elements with curved elements at the cladding boundary and at the core-cladding interface. Next, we discretize the time domain using the implicit Euler method. The full scheme is as follows:

If  $T^n, T^{n+1} \in H_0^1(\Omega_z)$  respectively denote the temperature of the fiber cross-section at the  $n^{\text{th}}$  and  $(n+1)^{\text{th}}$  time-step, then using implicit Euler's scheme we get,

$$\left(T^{n+1}, v\right) + \frac{\kappa_{\text{therm}} \Delta t}{\rho_0 C} \left(\nabla_{xy} T^{n+1}, \nabla_{xy} v\right) - \frac{\Delta t}{\rho_0 C} \left(Q(T^{n+1}), v\right) = \left(T^n, v\right), \quad (5.1)$$

for all  $v \in H_0^1(\Omega_z)$ . Here  $\Delta t$  denotes the size of the time-step. We solve equation (5.1) at each  $z$ -step of the fiber at each time-step. Next, we shall model the heat source term  $Q(T)$ .

### 5.3 Simulation of the onset of TMI

The content of this subsection are published in [19]. In this subsection, we investigate the power thresholds of the TMI for both single- and two-tone amplifier configurations at  $\lambda_s = 2110$  nm. The two-tone simulations are run with various seeding conditions, and include cases for two bulk Raman gain coefficients:  $g_R \in \{5, 15\} \cdot 10^{-14}$  m/W. Higher Raman gain coefficients can be achieved with specific passive dopants such as germanium. Only a straight fiber is considered, and its length has been fixed at  $L = 6$  m, which, in all cases, is sufficient to determine whether or not the amplifier has reached its TMI threshold. We consider a simulation to have reached the TMI threshold if the fundamental mode persistently transfers at least 10% of its power to higher order modes. The total seed power is set at 100 W, which ensures that the total ASE power throughout the fiber remains low ( $< 1$  W) for the single-tone case with 1 kW of launched pump power.

Table 5.1 lists the TMI threshold in terms of launched pump power ( $P_p(z = 0)$ ), and then provides the corresponding output signal amplification efficiencies and maximum total ASE powers. In the table, the single-tone (1: $\infty = 0$  seed ratio) and the 21:10 seed ratio two-tone configurations have about the same output signal powers in a cold fiber, making these set-ups very comparable to one another. Also, recall that the two-tone configuration with a 1:1 seed ratio approximately maximizes the output signal power for the amplifier. These cases show the trend as the tone seed power is increased compared to the signal seed power.

Other results of this study include the plot in Fig. 5.1 of the steady-state absolute temperature at the fiber's transverse center along the fiber length for both the single- and two-



tone cases of the coiled fiber, using an identical launched pump power that is below their respective TMI thresholds, and that have comparable output signal powers in a cold amplifier. Note that for the two-tone configured amplifier, in order to better spread the heat deposition more evenly along the fiber, one would ideally want the tone wavelength to be close to the average of the pump and signal wavelengths:  $\lambda_t \sim (\lambda_p + \lambda_s)/2$ . Since this is not the case for our Tm-doped amplifier, there likely will not be significant difference between the single- and two-tone longitudinal heat profiles. Although, Figure 5.1 demonstrates that with our configuration where the difference of frequencies  $\lambda_t$  and  $\lambda_s$  is 13.2 THz, the two-tone configuration does, to a small degree, spread the heat out along the fiber length a bit more than does the single-tone configuration, leading to a slightly lower peak temperature. Additionally, Figs. 5.2 and 5.3 provide visual snapshots of the output signal mode power levels through time, both below and above the TMI threshold, and for both the single- and two-tone configured amplifiers.

In this TMI threshold investigation, we find that the Raman gain is having a moderate impact on the TMI threshold depending on the seed ratio, and does seem to slightly mitigate the onset of the ASE. Recall that this is a large mode area fiber, and the two-tone config-

Table 5.1: Launched pump power TMI threshold interval, with its corresponding output signal amplification efficiencies and maximum total ASE power range, for a straight Tm-doped amplifier with a 2110 nm signal wavelength, and a 100 W total seed power.

$\mathbf{g_R = 5 \cdot 10^{-14} \frac{m}{W}}$	TMI Power Threshold Interval [kW]	Output Signal Efficiency Interval	Maximum Total ASE Power [W]
single-tone	2.3-2.4	0.555-0.563	< 1
two-tone (1:1)	1.6-1.7	0.595-0.611	20-25
two-tone (21:10)	1.9-2.0	0.575-0.595	60-75
$\mathbf{g_R = 1.5 \cdot 10^{-13} \frac{m}{W}}$	Threshold Interval [kW]	Efficiency Interval	ASE Power [W]
single-tone	2.3-2.4	0.555-0.563	< 1
two-tone (1:1)	2.2-2.3	0.610-0.613	< 1
two-tone (21:10)	3.0-3.1	0.610-0.625	< 1

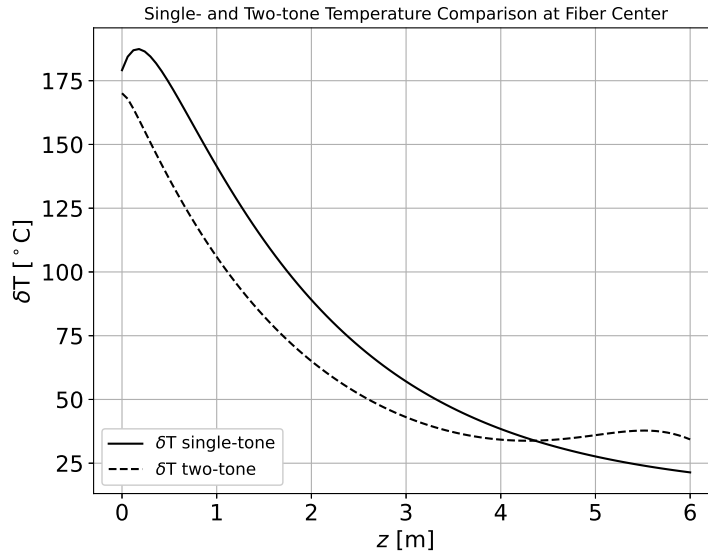
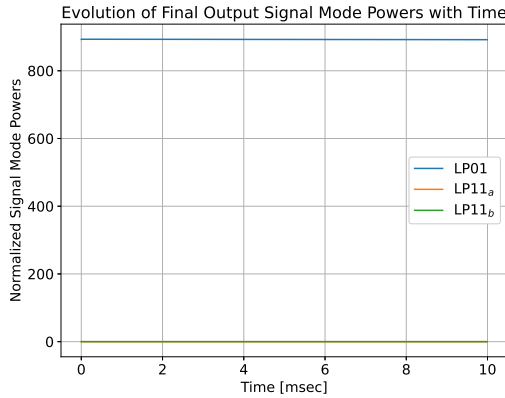
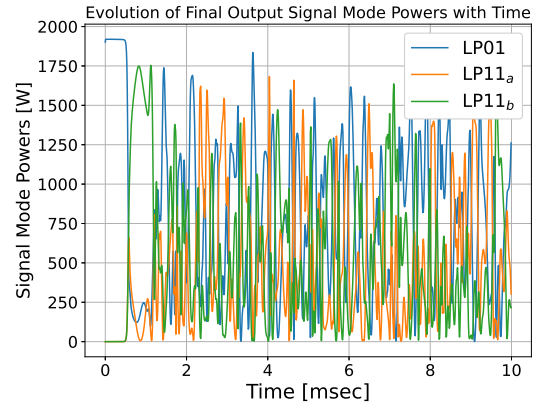


Figure 5.1: Change in temperature at the fiber center comparison between single- and two-tone coiled fiber at 2110 nm after 0.01 seconds.

uration tends to reduce the onset of optical non-linearities. The two-tone configuration, in general, is not able to significantly impact the longitudinal thermal profile compared to the single-tone configuration since the tone wavelength is relatively very close to the signal wavelength, rather than being more intermediate between the pump and signal wavelengths. Even still, our results indicate that the chosen seed ratio more prominently affects the TMI threshold and signal amplification efficiency in important ways. The two-tone configuration does seem to suppress the onset of the TMI over the single-tone configuration, at least as long as the ASE power levels are kept low. However, it is not too surprising that the TMI power thresholds are lower for the 1:1 seed ratio as compared to the 21:10 seed ratio, since the 1:1 seed ratio is closer to maximizing the output signal power. Unfortunately, the optimal seed ratio for mitigating the onset of the TMI will not likely be close to the optimal seed ratio for suppressing the onset of SBS. Even still, one may desire the lower seed ratios in order to maximize the output signal powers, and thus the signal amplification efficiency as well. And, as described previously, one problem with too high of a seed ratio is the onset

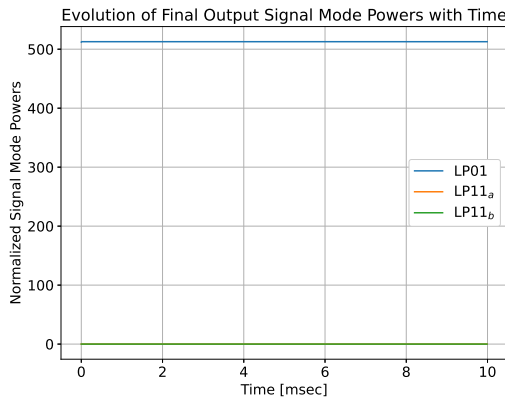


(a) Below TMI threshold.

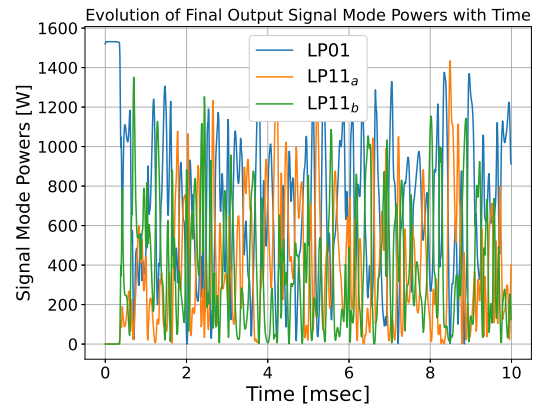


(b) Above TMI threshold.

Figure 5.2: Output signal mode powers for the single-tone configured straight amplifier operating either below (a) or above (b) the TMI threshold.



(a) Below TMI threshold.



(b) Above TMI threshold.

Figure 5.3: Output signal mode powers for the two-tone configured straight amplifier (1:1 seed ratio) operating either below (a) or above (b) the TMI threshold.

of ASE; however, this is where having a larger bulk Raman gain coefficient is helpful in mitigating the onset of ASE.

This CMT TMI model can also predict all kinds of useful data for experiments like optimal seed ratios, onset TMI power levels, onset ASE power levels, change in temperatures throughout the fiber, comparisons of single- and two-tone configurations, et cetera. These are discussed in more details in Chapter 6.

## Chapter 6

### Tm-doped Two-tone fibers and ASE

The content of this chapter are published in [19]. The chapter focuses on the results from simulating the model described in section 2.4.

Table 6.1: Important emission ranges of different rare-earth ions [50]

Rare-earth ions	Emission range
$Ho^{3+}$	2.1-2.9 $\mu\text{m}$
$Er^{3+}$	0.55 $\mu\text{m}$ , 1.5-1.6 $\mu\text{m}$ , 2.7 $\mu\text{m}$
$Tm^{3+}$	0.48-0.8 $\mu\text{m}$ , 1.45-1.53 $\mu\text{m}$ , 1.7-2.1 $\mu\text{m}$
$Yb^{3+}$	1.0-1.1 $\mu\text{m}$

In this report we will talk about Tm-doped fibers. As we can see from Table 6.1, Tm-doped fibers can operate in eye-safe laser wavelengths and they can reach an atmospheric transmission window. The difficulty of lasing and/or amplifying a laser signal in the 2.1-2.2  $\mu\text{m}$  regime is due to the fact that the gain spectrum of the thulium (Tm) dopant rapidly diminishes beyond 2.1  $\mu\text{m}$ , as shown in Fig. 6.1. Part of the problem is that it will be difficult to create a strong seed power for the signal, and combined with the low gain in this wavelength range, one expects to observe significant amounts of ASE, and possibly parasitic lasing [4] consequently. However, above 2100 nm in wavelength there are some

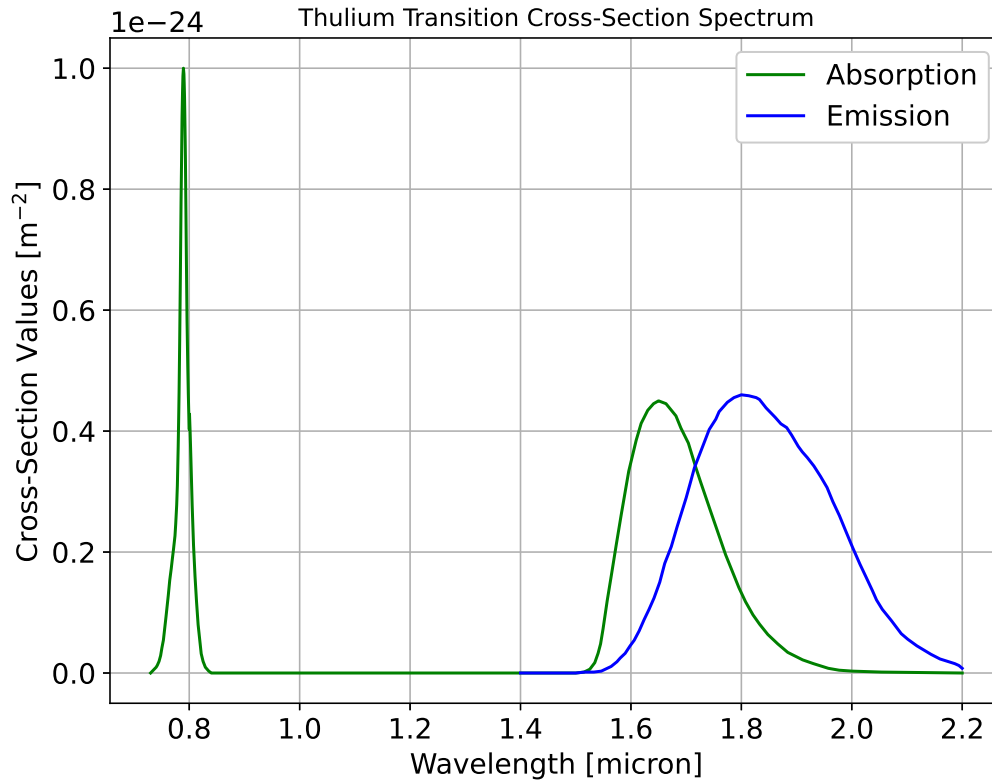


Figure 6.1: Absorption and emission cross-section spectra of the thulium dopant [65].

propitious atmospheric transmission windows, where one can expect to get up to about 95% transmission, as seen in Fig. 6.2 [7, 6, 28].

Tm-doped amplifiers can have higher dopant concentrations than ytterbium-doped amplifiers, and thus they are more susceptible to cross-relaxations and upconversions (see Fig. 6.3) [23]. The strong cross-relaxation in the thulium kinetics model can almost double the optical-to-optical (O-O) efficiency of the amplifier. Also, heat generation in the fiber is still an important issue that can either degrade ( $\sim > 85^\circ\text{C}$ ), or even destroy ( $\sim > 125^\circ\text{C}$ ), the polymer coating. The trade-off to be considered is that the heat deposition per unit length

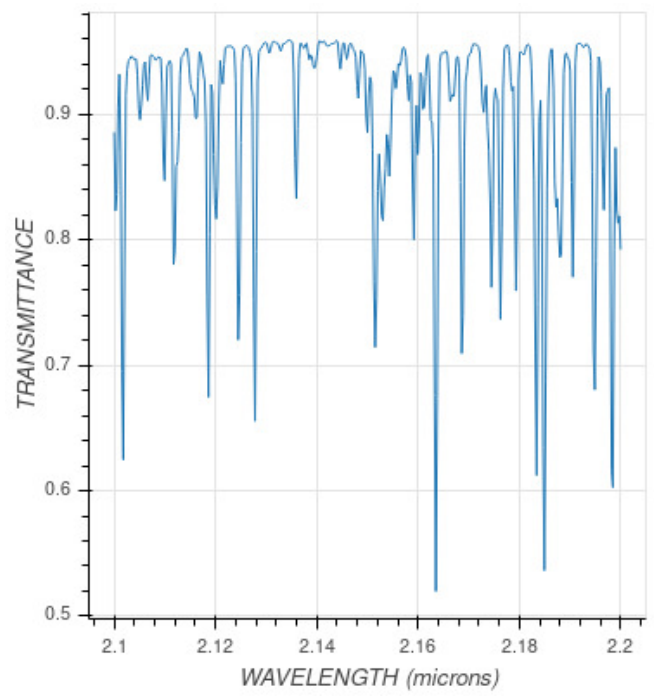


Figure 6.2: Atmospheric transmittance in the wavelength range 2.1-2.2  $\mu\text{m}$ .

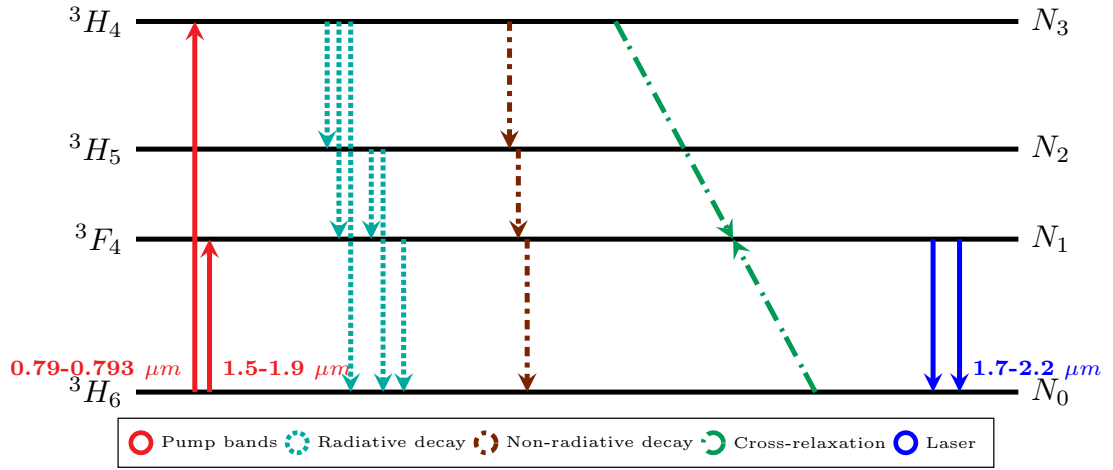


Figure 6.3: Simplified thulium electron energy level diagram.

will decrease as the dopant concentration is lowered; however, the cross-relaxation process also diminishes in direct proportion to the dopant concentration. Without a pronounced cross-relaxation, the fiber efficiency ( $\eta$ ) will tend towards what would be expected from the quantum defect:  $\eta \sim 1 - \lambda_p/\lambda_s$ , which would vastly increase the amount of energy being deposited as heat per unit length. This study will use the steady-state thulium energy level kinetics model presented in McComb's dissertation [40], and will only consider the typical co-/cladding-pumped configuration, where the wavelength of the pump light is near the peak absorption around 790-793 nm. In the absorption/emission dataset that we have [65], this peak occurs at 790 nm.

This model considers a continuous-wave, weakly guided, step-index Tm-doped optical fiber amplifier with core radius  $r_{\text{core}} = 10 \mu\text{m}$ , surrounded by a pure fused silica inner cladding that extends to radius  $r_{\text{clad}} = 200 \mu\text{m}$ , and a polymer jacket of thickness  $75 \mu\text{m}$  ( $r_{\text{fiber}} = 275 \mu\text{m}$ ). The refractive index of the core and the inner cladding regions are denoted as  $n_{\text{core}}$  and  $n_{\text{clad}}$ , respectively. The core numerical aperture ( $\text{NA}_{\text{core}} = \sqrt{n_{\text{core}}^2 - n_{\text{clad}}^2}$ )

is 0.09. Generally, our model follows the same coupled mode theory approach as described in Naderi et al. [47], though we use a slightly different notation. Other notable differences include the fact that we modify the governing equations for the inclusion of the ASE wavelengths, the intrinsic loss of the glass, the loss due to  $\text{OH}^{-1}$  (hydroxide) contamination, and the mode-bend-loss (when the fiber is coiled). Moreover, the transverse domain is discretized using higher (polynomial) order finite elements, such that the elements conform to the fiber boundaries. All integrations over the transverse domain are computed using at least third-order Lagrangian element spaces ensuring higher precision calculations [18].

Only the transverse guided core modes are included in the model for the tone, signal, and ASE wavelengths, and the pump light is modeled as a planewave [13, 17]. The mode profiles and pump planewave extend throughout the core and inner cladding regions, but are considered to be negligibly small in the polymer coating region. Under the fiber coiling situations, the corresponding mode-loss values are calculated using the technique outlined by Schermer & Cole [55]. Our propagation model is currently not capable of handling coiled fiber mode profiles, so instead we use the straight fiber mode profiles. Though we do use the proper propagation constants and mode-bend-losses. Even still, after some numerical testing we found that in all cases pertinent to our investigations, comparing the coiled ( $R_{\text{bend}} = 80$  mm) and straight fibers and including multiple wavelengths and thermal load conditions, the mode overlaps with the core (gain) region of the fibers only varies by 5.3% at most. This would not hold true under tighter bends. Likely, the low variation in mode overlaps is due to the fact that Tm-doped fiber amplifiers have larger core numerical apertures (especially compared to Yb-doped amplifiers), which limit the mode deformation significantly. One consequence of this is that the gain saturation is maximized, which means that, in most situations, our results show best-case performance metrics.



This simulation only accounts for the forward propagating ASE, and only considers the fundamental mode at each ASE wavelength. Though it is certainly possible to include backward propagating light in the model, and backward ASE affects the onset of the TMI [5, 12], this effort is only attempting to indicate when ASE will be an issue, not to accurately model its quantity nor its precise effects on amplifier performance. Moreover, including any backward propagating light would significantly increase the simulation runtime. We feel that this approach offers a fair indication of when ASE will become prominent in the amplifier, while keeping the simulations computationally tractable. The change in the fiber temperature compared to the ambient temperature (25°C).

It satisfies the heat equation with a source term ( $Q$ ) representing the net absorption along the fiber, primarily due to the gain mechanisms. An analysis of the relative sizes of derivatives in the heat equation indicates that  $\partial_z^2[\delta T]$  may be neglected. We solve the time dependent transverse heat equation (2.26) on the transverse domains  $\Omega_{z_0}^{\text{fiber}} = \{(x, y, z) | x^2 + y^2 \leq r_{\text{fiber}}^2; z = z_0 \in [0, L]\}$  at each discrete longitudinal point along the fiber, with a zero Dirichlet boundary condition at the boundary  $r = r_{\text{fiber}}$ .

The main goal of this chapter is to present relevant information, extracted from computer simulation results, on the practicality and feasibility of a Tm-doped fiber amplifier operating in the 2100-2200 nm wavelength regime. The detailed numerical simulations will investigate different dopant concentrations, single- and two-tone amplifier configurations, various seed ratios and total seed powers in a straight fiber, or one that is circularly bent ( $R_{\text{bend}} = 80$  mm), all at three specific signal wavelengths: 2110 nm, 2133 nm, and 2170 nm. This makes for a hybrid gain amplifier, including the active Tm dopant [17] and gain from the SRS optical non-linearity [48], with the hope of, at least slightly, improving the suppression of the ASE and reducing the amplifier length that achieves 95% pump

absorption. Also, expected peak temperatures within the fiber, signal output powers, and signal amplification efficiencies, will be shown, all while allowing ASE to arise naturally in the amplifier based on the given conditions. Moreover, we will show the effect of wavelength on the mode-bend-loss values in the presence of three distinct steady-state thermal profiles.

Section 6.1 presents the modeling results, starting with the wavelength and temperature dependence of the guided core mode-bend-losses near  $2\mu\text{m}$  (subsection 6.1.1) and a brief comparison between single- and two-tone amplifier output signal powers (subsection 6.1.2). Then, subsection 6.1.3 provides results regarding the effects of varying the total dopant concentration. The onset of ASE in the amplifier is studied in subsection 6.1.4 as seeding conditions are altered. Each of these result subsections quantify aspects of complicated trade-space that pertains to Tm-doped amplifiers operating in the  $2.1\text{-}2.2\mu\text{m}$  wavelength range.

## 6.1 Simulation results

In all of our runs, we have included experimentally calculated values for background silica loss and  $\text{OH}^{-1}$  contamination loss (1 ppm) extracted from [58, Fig. 2]. The thulium absorption/emission cross-section values are evaluated using the data extracted from [65]. Moreover, this model considers ASE within the  $1.9\text{-}2.15\mu\text{m}$  wavelength band by binning this region into five equally sized bins. The first bin has a central wavelength set at 1925 nm, and each bin spans  $\Delta\lambda_{\text{ASE}} = 50\text{ nm}$  in wavelength. Using more ASE bins over the same region is more accurate, since each bin references the gain parameters at the central wavelength, which vary over the ASE wavelength window. However, based on our numerical tests, so long as the ASE levels power remain low ( $\sim < 5\text{ W}$ ), five bins produce results that

are within a few percent of those found when twenty five bins are used. The total dopant concentration is uniformly distributed throughout the fiber core region, and is formulated as  $N_{\text{total}} = (3 \cdot 10^{26}) \mathcal{N}_{\text{factor}} [\text{ions}/\text{m}^3]$ , where  $\mathcal{N}_{\text{factor}}$  is a unitless scaling factor. Additionally, the fiber length is always set at the point where 95% of the pump power has been absorbed ( $L \equiv L_{95\%}$ ). Seed ratios are always presented as the tone power to the signal power ( $P_t:P_s$ ) in its reduced fraction form. Finally, in all cases when the amplifier is coiled, the bending is circular such that  $R_{\text{bend}} = 80$  mm all along the fiber length.

### 6.1.1 Thermally dependent mode-bend-loss

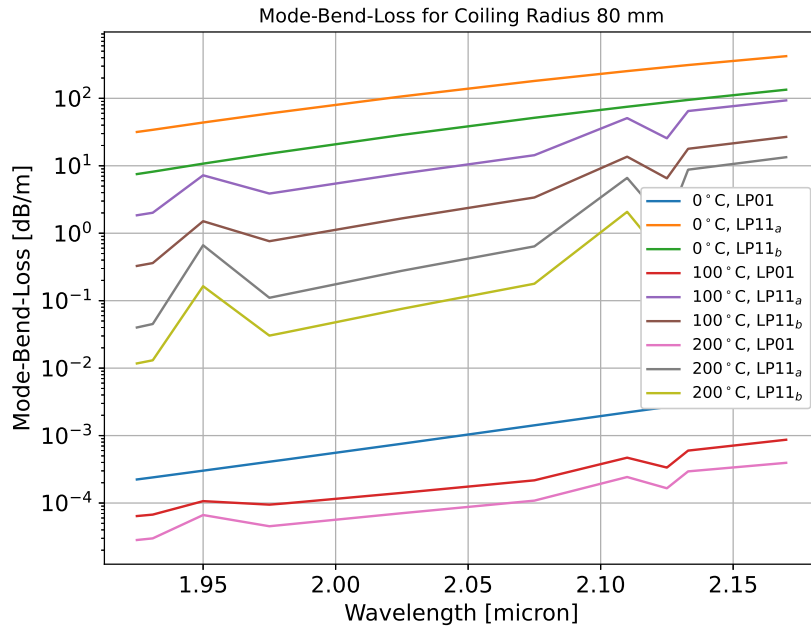


Figure 6.4: Mode-bend-loss behavior under three different temperature profiles.

When the amplifier is coiled, the calculation of the mode-bend-loss values account for thermal effects by altering the refractive index according to thermal profiles, utilizing relation (2.64), at specified discrete peak change in temperature values [19]. Figure 6.4 shows

the computed mode-bend-loss behavior at three different fiber peak change in temperatures, namely 0°C, 100°C, and 200°C, as the wavelength varies around 2  $\mu\text{m}$ . In this plot, the mode-bend-losses increase with the wavelength for the guided core modes because longer laser wavelengths result in fiber waveguides that are closer to being robustly single-mode. However, the thermal lensing effect reduces the mode-bend-loss values by increasing the numerical aperture of the fiber core region, and therefore its  $V$ -number. The kinks in this plot may be due to the fact that our mode solver is finding degenerate modes compared to what it found at other wavelengths. However, this is not evident in the numerical results, which are always finding only one solution for the fundamental mode, and for each orientation of the LP<sub>11</sub> mode. For now these kinks may be considered part of the uncertainty in the calculated mode losses.

### **6.1.2 Single- and two-tone output signal power comparisons**

This study describes the two-tone seed ratios that either match the single-tone amplifier output signal power or maximize the amplifier output signal power in a cold amplifier [19]. In all cases the length of the fiber is set at where 95% pump absorption occurs, the amplifier is given 1 kW of launched pump power, the amplifier is coiled and has a total seed power, summing the tone and signal values across all modes, of 100 W. Heating effects are not considered. For  $\lambda_s = 2110$  nm, the single- and two-tone configured amplifiers produce nearly identical signal output powers when the two-tone seed ratio is 21:10. However, the amplifier reaches its maximum output signal power when a 1:1 ratio is used in the two-tone configuration. For the signal wavelengths of 2133 nm and 2170 nm, the single-tone configuration seems to produce the maximum output signal power for the amplifier. For these wavelengths, we checked seed ratios as low as 1:50 for the two-tone configured

amplifier, and the output signal powers were increasing as this seed ratio decreased.

### 6.1.3 Effects of the dopant concentration

In this investigation we vary the Tm dopant concentration to study important amplifier performance characteristics. Both single- and two-tone amplifier configurations are considered, and straight and coiled fiber cases are investigated. In all cases, the total seed power is 20 W, and, if not otherwise stated, the total launched pump power is 1 kW. This total seed power was chosen to ensure that the ASE wavelengths do not grow to significant levels ( $< 1$  W). For the two-tone configuration simulations, a 10:1 seed ratio is used. The first reported metric is the fiber length that corresponds to 95% pump power absorption. The fiber performance is also characterized by the output signal power ( $P_s(z = L)$ ), the output signal amplification efficiency ( $\eta_s(z = L)$ ), and the peak change in temperature ( $\delta T_{\max} = \max(T(x, y, z, t)) - T_{\text{ambient}}$ ) experienced throughout the amplifier. In this study, the normalized power is obtained by dividing the given power by the total initial power, which is the sum of the total seed power and the launched pump power. The fiber signal amplification efficiency ( $\eta_s$ ) at longitudinal point  $z_0$  is expressed by the following formula:

$$\eta_s(z = z_0) = \frac{P_s(z = z_0) - P_s(z = 0)}{P_p(z = 0) - P_p(z = z_0) + P_t(z = 0) - \max\{P_t(z = 0), P_t(z = z_0)\}}.$$

The numerical modeling results of this study for the straight and coiled fibers are illustrated in figures 6.5, 6.6, 6.7, and 6.9. We plot 6.5, and 6.6, the first row shows the fiber length at which 95% of the launched pump power is absorbed. The second and third rows, respectively, depict the trends in the output signal powers and the output amplifier efficiencies under the same variations of the total dopant concentration. We plot the peak change in temperature variations over the entire length of the straight fiber in the core 6.7

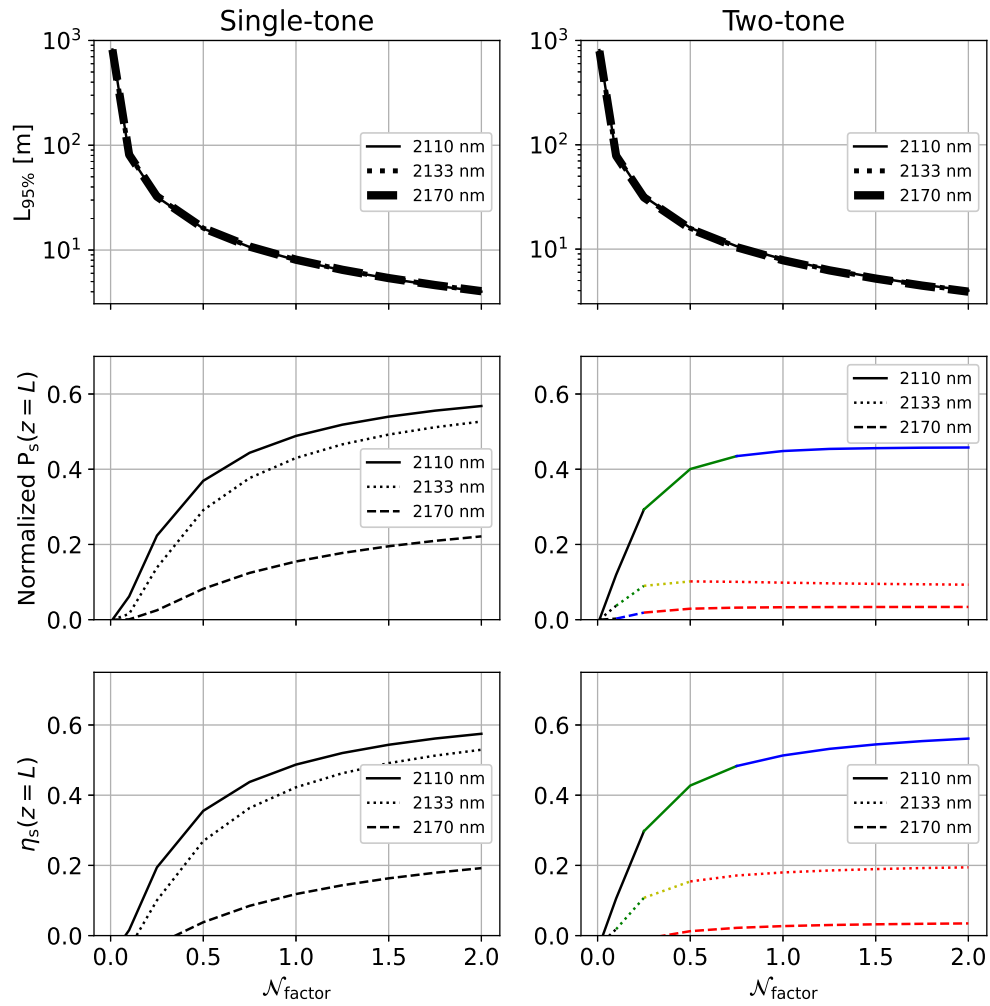


Figure 6.5: Straight amplifier performances. The color-codes indicate a range of ratios of output tone power to output signal power: —  $< 0.01$ , —  $0.01-0.1$ , —  $0.1-0.5$ , —  $0.5-1.0$ , and —  $> 1.0$ .

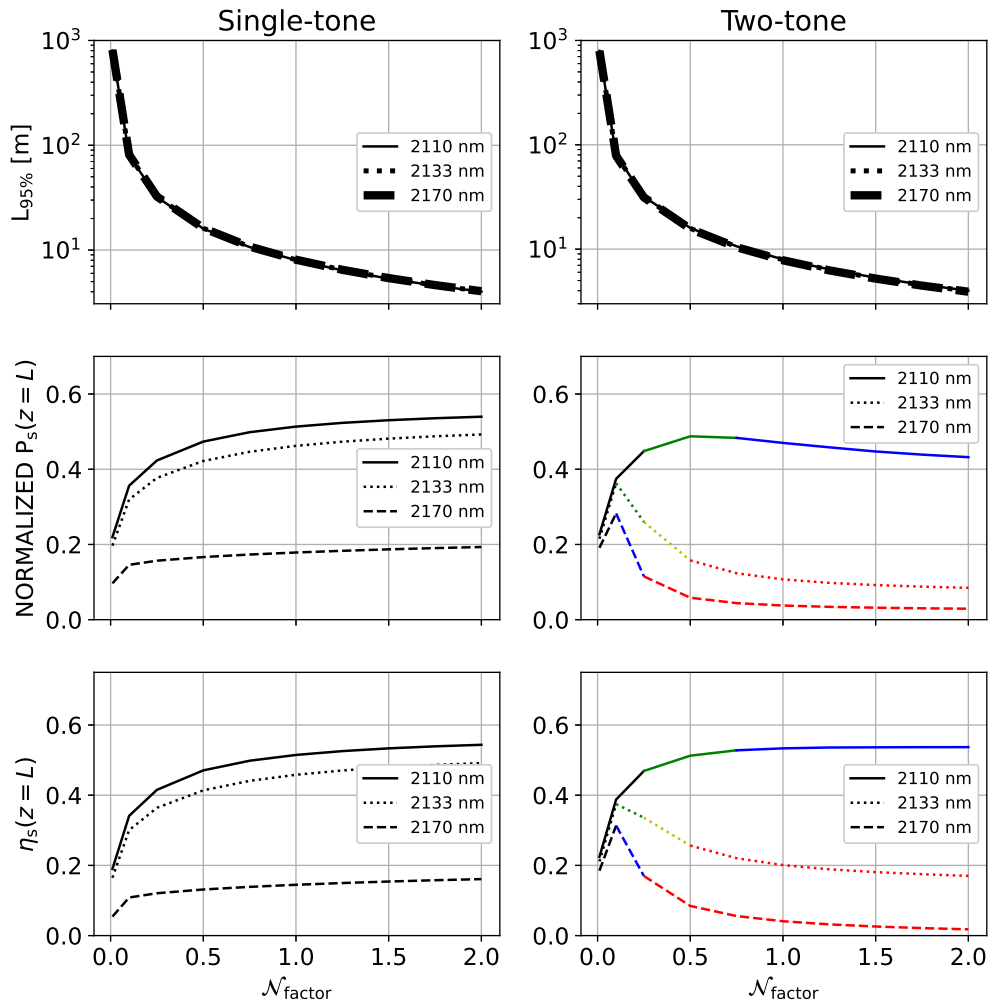


Figure 6.6: Coiled amplifier performances. The color-codes indicate a range of ratios of output tone power to output signal power: —  $<0.01$ , —  $0.01-0.1$ , —  $0.1-0.5$ , —  $0.5-1.0$ , and —  $>1.0$ .

and polymer jacket 6.9 regions. The coiled fiber results are very similar to the straight fiber results, illustrated in Figures

Recall that this study uses a fixed seed ratio, and thus is not optimizing the output signal power. Therefore, a color-code is implemented to better describe the amplifier output behavior. In Figure 6.5, and 6.6, the second and third rows of the two-tone column uses black to signify that output tone power is less than 1% of the output signal power, whereas green indicates this ratio is within 0.01 and 0.1, blue represents that it is between 0.1 and 0.5, yellow is for 0.5 to 1, and, finally, red indicates that the ratio is above 1.

The main trade-off to be considered is that a higher dopant concentration allows for a shorter fiber, which typically acts as an optical non-linearity suppression mechanism (e.g., SBS mitigation); however, it also results in higher fiber temperatures. As described previously, higher temperatures can lead to polymer degradation or failure. The higher temperatures reduce the mode-bend-losses (review Fig. 6.4), including the differential mode-losses, which would make higher-order mode filtration less efficacious [34]. Near single-mode operation leads to better output beam quality. Longer fiber amplifiers are better for achieving this mode filtration effect since the losses are a scattering process as the light propagates. However, a longer fiber will also likely result in lower amplifier efficiencies since the mode-bend-losses, intrinsic silica losses, and hydroxide contamination losses will have a greater impact on the performance. Note that the heating due to absorption from the loss mechanisms is non-negligible in terms of total energy deposited throughout the fiber, and thus are included in the heat source term ( $Q$ ), but they do not have a significant impact on the peak change in temperatures. None of these results are surprising, or unexpected.



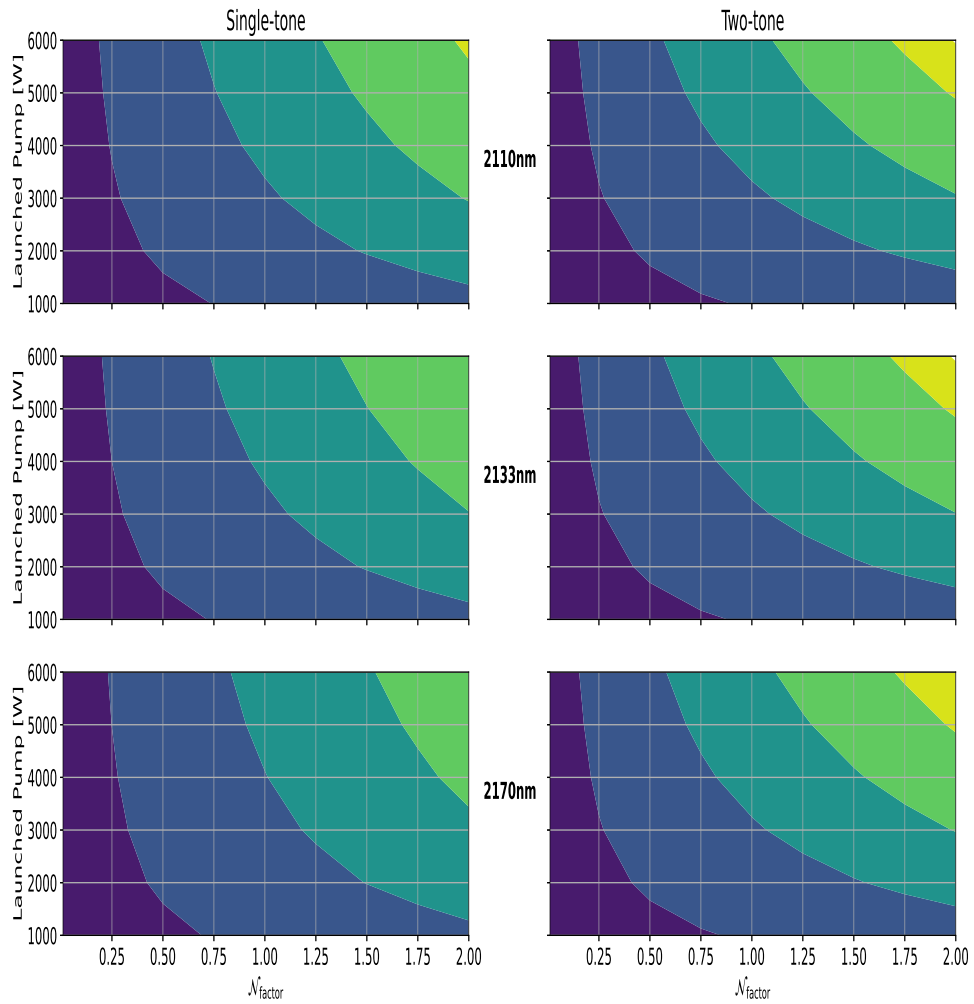


Figure 6.7: Peak change in temperature in a straight fiber throughout the core region as a function of launched pump power and dopant concentration. Color bands relate to peak change in temperature ranges (core region) as follows:

■ 17°C-77°C, ■ 77°C-177°C, ■ 177°C-277°C, ■ 277°C-377°C, and ■ 377°C-427°C.

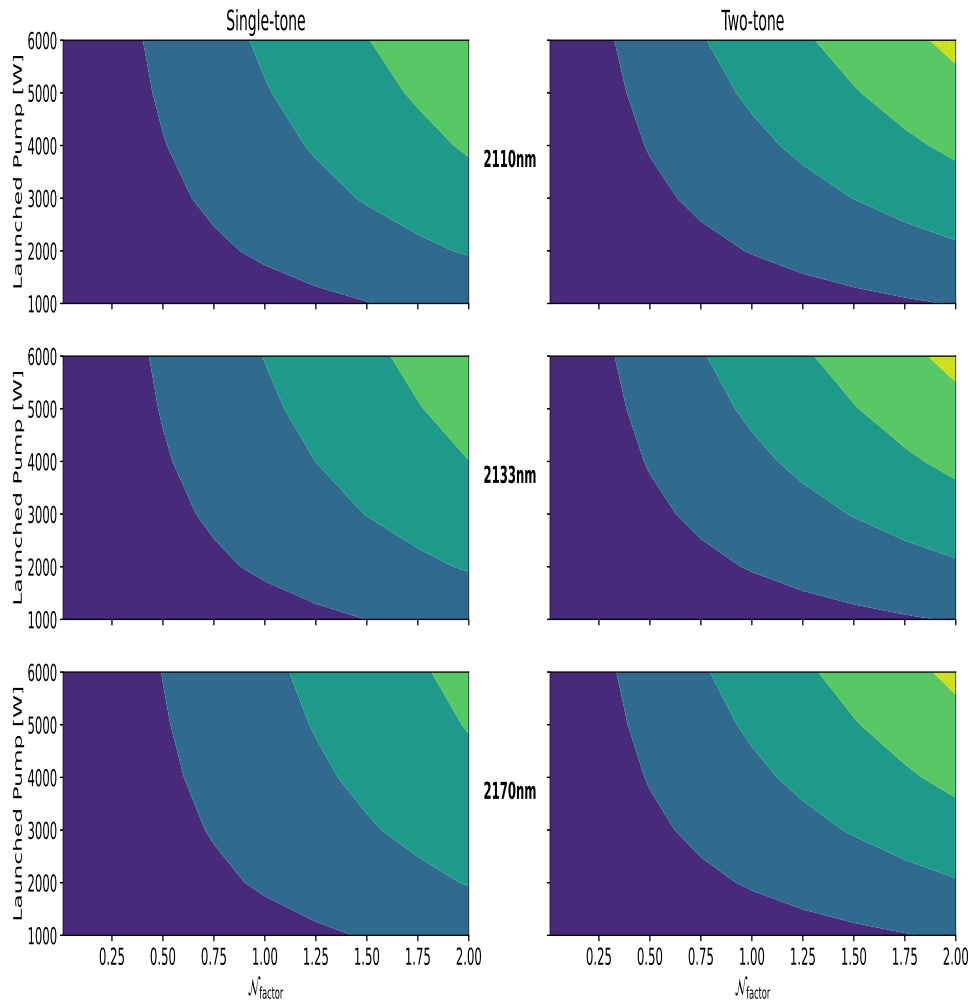


Figure 6.8: Peak change in temperature in a straight fiber throughout the core region as a function of launched pump power and dopant concentration. Color bands relate to peak change in temperature ranges (core region) as follows:

17°C-77°C, 
  77°C-177°C, 
  177°C-277°C, 
  277°C-377°C, and 
  377°C-427°C.

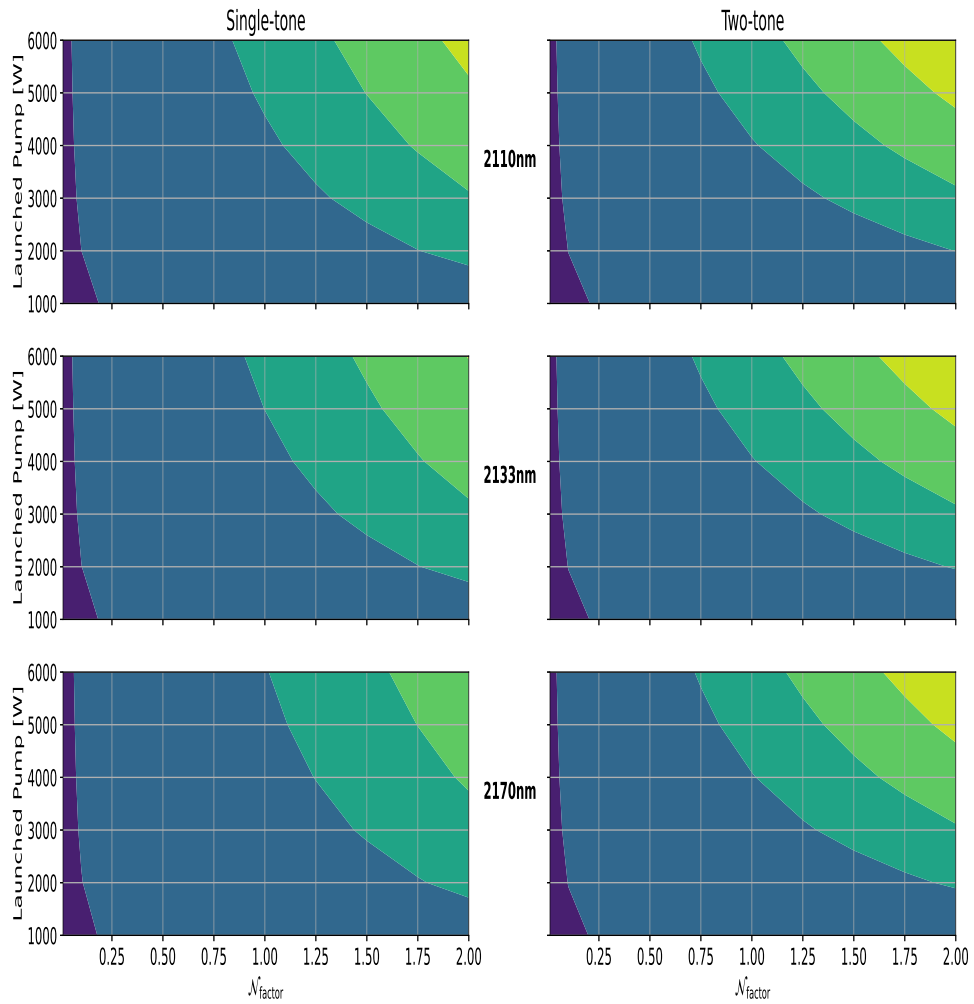


Figure 6.9: Peak change in temperature in a straight fiber throughout the polymer coating region as a function of launched pump power and dopant concentration. Color bands relate to peak change in temperature ranges (polymer region) as follows:  
 ■ 17°C-27°C, ■ 27°C-47°C, ■ 47°C-57°C, ■ 57°C-67°C, and ■ 67°C-77°C.

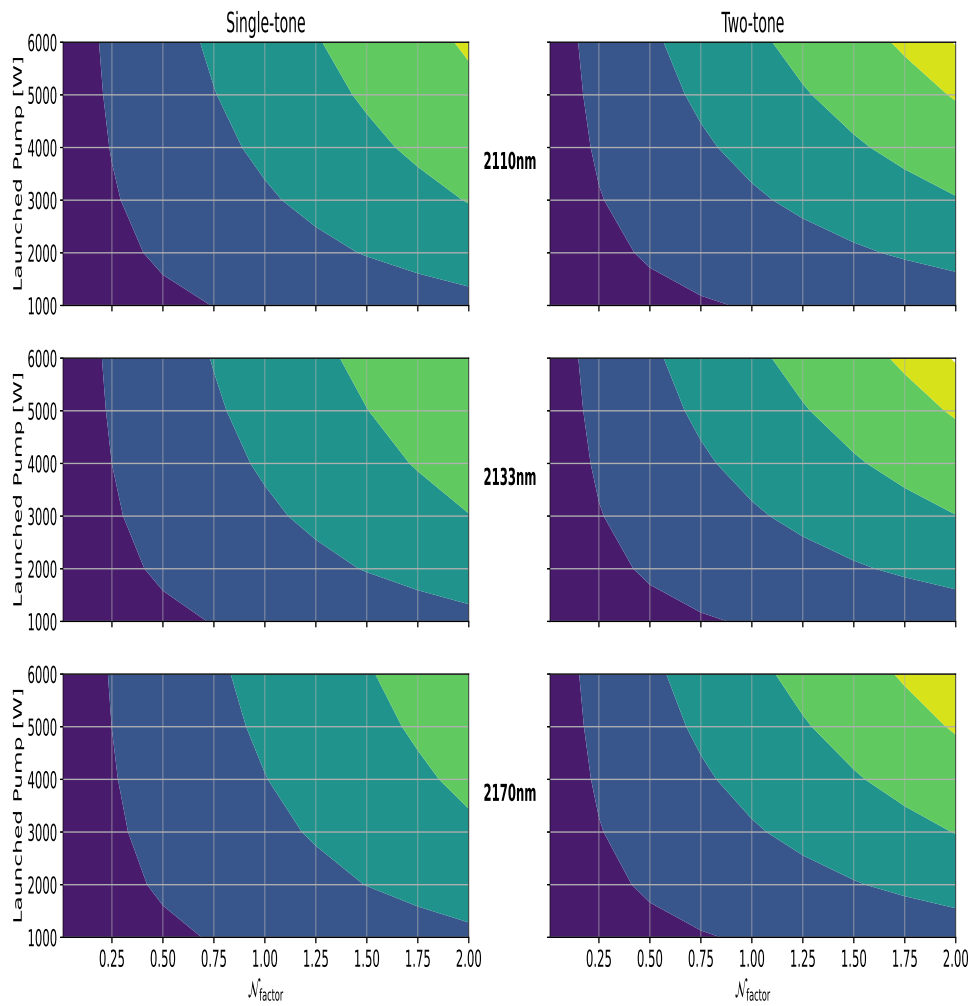


Figure 6.10: Peak change in temperature in a coiled fiber throughout the core region as a function of launched pump power and dopant concentration. Color bands relate to peak change in temperature ranges (core region) as follows:

■ 17°C-77°C, ■ 77°C-177°C, ■ 177°C-277°C, ■ 277°C-377°C, and ■ 377°C-427°C.

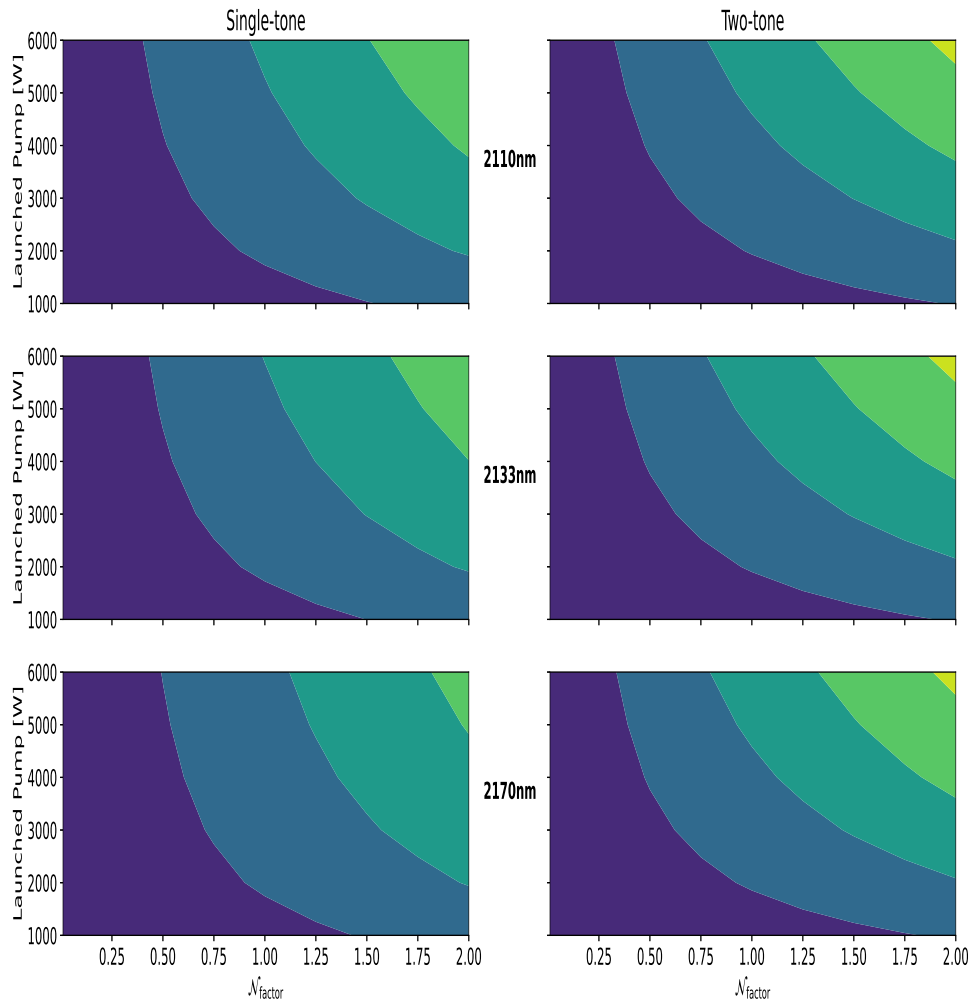


Figure 6.11: Peak change in temperature in a coiled fiber throughout the core region as a function of launched pump power and dopant concentration. Color bands relate to peak change in temperature ranges (core region) as follows:

■ 17°C-77°C, ■ 77°C-177°C, ■ 177°C-277°C, ■ 277°C-377°C, and ■ 377°C-427°C.

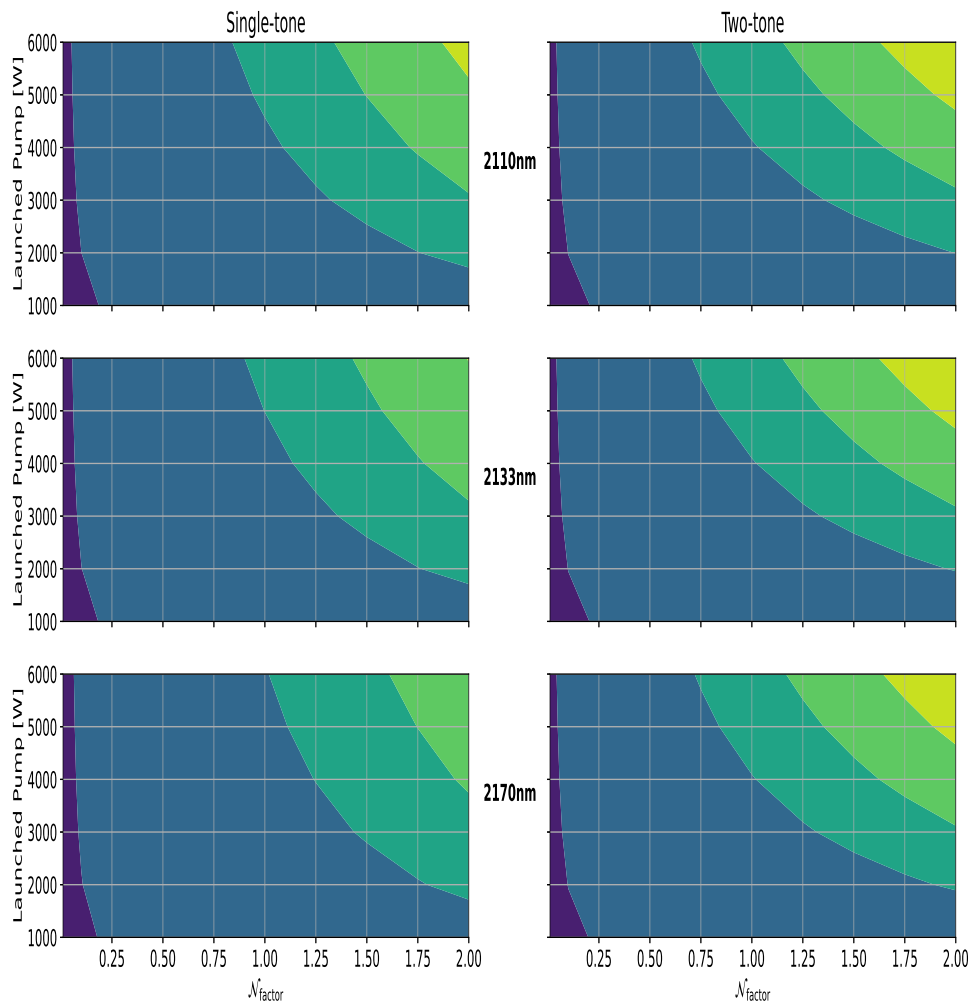
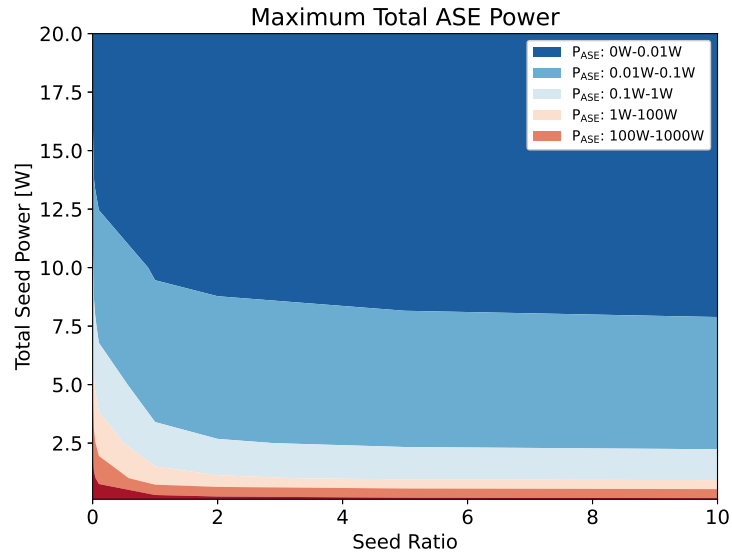


Figure 6.12: Peak change in temperature in a coiled fiber throughout the polymer coating region as a function of launched pump power and dopant concentration. Color bands relate to peak change in temperature ranges (polymer region) as follows:  
 ■ 17°C-27°C, ■ 27°C-47°C, ■ 47°C-57°C, ■ 57°C-67°C, and ■ 67°C-77°C.

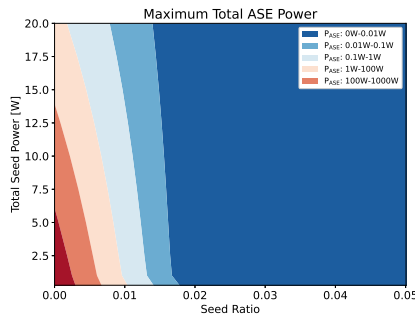
#### 6.1.4 Onset of ASE based on seed conditions

Amplified spontaneous emission is an issue when lasing in the 2.1-2.2  $\mu\text{m}$  wavelength regime especially when one cannot achieve high enough seed powers to sufficiently saturate the active gain mechanism such that stimulated emission dominates, and suppresses the spontaneous emission. In these simulations, we are launching 1 kW of pump power into the coiled fiber, and are using a total dopant concentration of  $3 \cdot 10^{26}$  ions/m<sup>3</sup> ( $\mathcal{N}_{\text{factor}} = 1$ ). Note that the circular bending of the fiber has little effect on the onset of ASE. Furthermore, the total ASE power is calculated by summing together the powers of each of the five ASE wavelength bins. Finally, for simplicity, we treat the fibers as being robustly single-mode, which allows us to implement the equivalent short fiber concept delineated in [17] without loss of simulation fidelity.

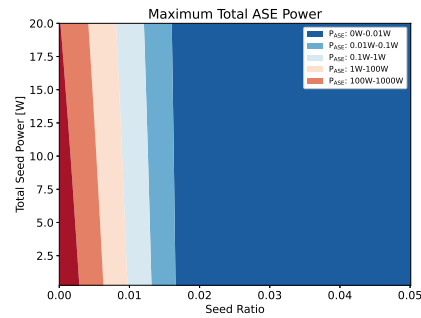
Figure 6.13 displays color contours for the maximum total ASE power levels along the amplifier based on the total seed power and the seed ratio for all three signal wavelengths. The seed ratios used for this study are 1:50, 1:25, 1:10, 1:1, 2:1, 5:1, and 10:1. These ratios are given as decimals on the abscissa of the plots. Moreover, the single-tone configured amplifier results are plotted at the seed ratio of  $1:\infty = 0$ . For the signal wavelengths of 2133 nm and 2170 nm, review Fig. 6.13 plots b and c respectively, the total ASE power only increases significantly as the seed ratios approach the single-tone case, and thus are zoomed to that region. In the remaining part of these two plots, the maximum ASE power level remains below 0.01 W within the considered fiber length. Our results reflect the expectation that by increasing the total seed power, the onset of ASE is mitigated. It is also clear from the data that lower seed ratios are worse at suppressing the ASE. This is also not surprising, given that the signal is at a wavelength of low gain for the Tm dopant, and therefore needs a stronger seed to ensure stimulated emission throughout the fiber.



(a)  $\lambda_s = 2110$  nm



(b)  $\lambda_s = 2133$  nm



(c)  $\lambda_s = 2170$  nm

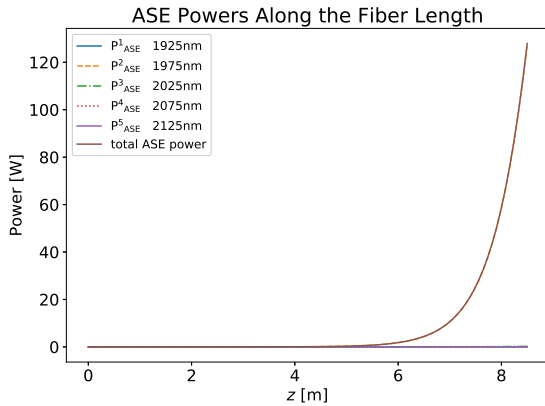
Figure 6.13: Maximum total ASE power levels in a straight fiber.

Figures 6.14–6.16 provide some examples of the ASE power profiles along the fiber length, including the sum total ASE power level, when the total seed power is 5 W. The stark difference in the ASE power levels between the two-tone (a) and single-tone (b) configurations in both Fig. 6.15 and 6.16 provide some indication as to why the ASE power levels are so low at all seed ratios for data collected at  $\lambda_s = 2133$ , and 2170 nm (see Fig. 6.13 plots b and c). In these cases, for the two-tone configuration, the tone wavelength is near

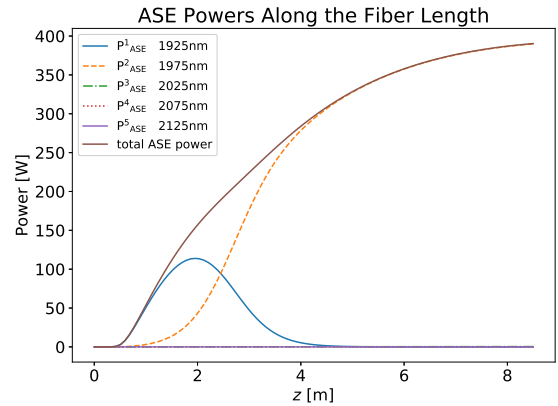


the peak in the gain spectra of the Tm dopant. Thus, the tone laser saturates the gain so well that the spontaneous emission is suppressed. The signal is so weak that it does not compete well for the active gain, and the SRS effect is not strong enough to compensate. Therefore, most of the output power resides in the tone wavelength. This demonstrates that, when operating outside the main gain bandwidth, large seed ratios will likely inhibit the signal amplification. However, in the single-tone case, there is no tone wavelength to force stimulated emission, and so the ASE grows significantly.

This numerical simulation effort provides important quantifications of the complex performance trade-space for high-power continuous-wave Tm-doped fiber laser amplifiers operating in the 2.1-2.2  $\mu\text{m}$  wavelength regime. All of these calculations are done under somewhat idealized conditions, but are indicative of what can be anticipated in real amplifiers. The results provide relative magnitudes and trends that allow other researchers to identify potentially important parameter ranges to quantify their amplifier performance under various configurations.

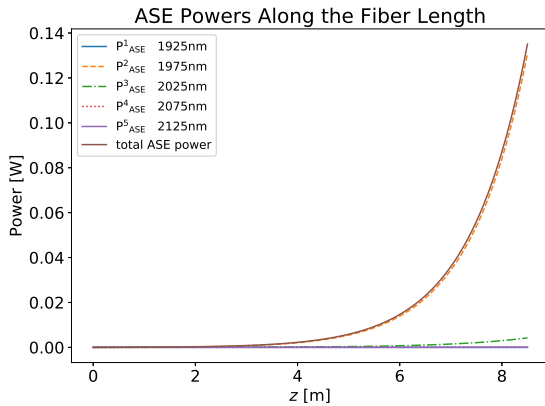


(a) Two-tone configuration with a 10:1 seed ratio.

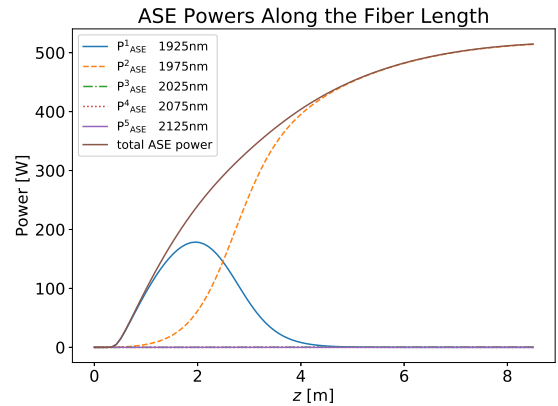


(b) Single-tone configuration.

Figure 6.14: ASE power levels when  $\lambda_s = 2110$  nm using total seed power of 5 W.

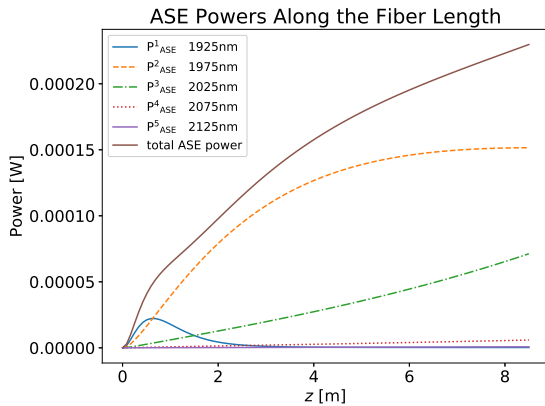


(a) Two-tone configuration with a 10:1 seed ratio.

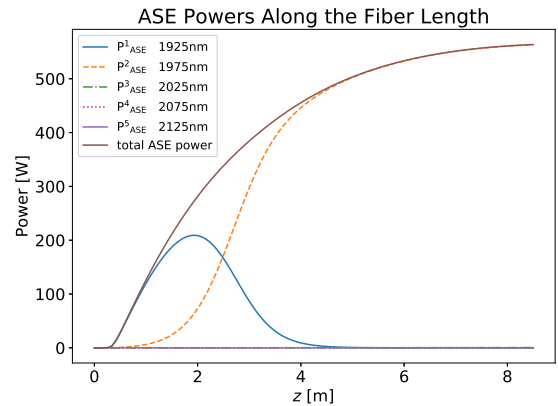


(b) Single-tone configuration.

Figure 6.15: ASE power levels when  $\lambda_s = 2133$  nm using total seed power of 5 W.



(a) Two-tone configuration with a 10:1 seed ratio.



(b) Single-tone configuration.

Figure 6.16: ASE power levels when  $\lambda_s = 2170$  nm using total seed power of 5 W.

## **Chapter 7**

### **Propagation of light in the presence of artificial gratings**

As we have already discussed, one of the issues, which is currently recognized to be the main roadblock to power scaling of beam combinable fiber amplifiers, is the nonlinear transverse mode instability (TMI). TMI can be described as a sudden breakdown in beam quality at high power operation, first observed experimentally [15]. As pointed out in the review [31], when attempting to design highly coherent lasers capable of sustained high (average) powers, a practically uncrossable limit was encountered due to the TMI. After intensive speculations on the cause of TMI, the prevailing theory seems to be that the cause is a temperature-induced grating. Numerical modeling is essential for investigating the TMI, and other non-linearities that arise inside fiber amplifiers, since experimental evidence is mostly limited to examining the amplifier output, and cannot measure the onset of physical effects that occur inside of the glass fiber. Before we try to find the root cause of TMI, a firm understanding is required about how the power transfer occurs between modes due to refractive index grating. One of the most discussed refractive index gratings is the Fiber Bragg Grating or FBG. An FBG is a periodic perturbation or change of the refractive index along the fiber length formed by exposing the core of the optical fiber to an intense optical interference pattern. When the grating period equals half the input

light wavelength, the first wavelength signal will be reflected coherently to make a large reflection. The reflected wavelength is called the Bragg wavelength, and defined by the relationship:

$$\text{Bragg wavelength} = 2n\Lambda,$$

where  $n$  is the effective refractive index of the grating in the fiber core and  $\Lambda$  is the grating period.

### 7.1 Long Period Bragg Grating and Mode Coupling

Our interest here is Long Period Bragg Gratings or LPBGs which can couple modes with the same propagating direction inside the core. The long period gratings have an effect on mode coupling because the grating period is now about 1000x bigger and similar to the inter-mode beat length. Thus, physical structures like the gratings only interact with electromagnetic phenomenon (light or beating modes) when they have similar sizes. For example, the fundamental mode or FM of a multi-mode fiber can be coupled to a certain higher-order mode or HOM, or a core mode can be coupled to cladding modes propagating in a similar direction using LPBG. In order to do this, we need to make sure that the grating period is equal to the difference of the phases of the two involved modes, i.e. if we want to couple two modes having propagation constants  $\beta_1$  and  $\beta_2$ , using an LPBG of period  $d$ , then for ideal coupling the above condition states

$$d = \frac{2\pi}{\Delta\beta},$$

where  $\Delta\beta = (\beta_1 - \beta_2)$ . We can easily couple from the fundamental (LP<sub>01</sub>) mode to any higher-order mode with  $l = 0$  ( $l$  corresponds to first index of LP<sub>lm</sub>, where  $l$  is the azimuthal

order and  $m$  is the radial order), and even to modes with  $l \neq 0$  if the Bragg grating is radially asymmetric. Numerical verification of these results are given in the following sections.

Now before proceeding further we need to remember that we are most interested in the conditions that cause power or energy to leave the fundamental mode. This is because we want an LMA fiber (which supports a few core guided modes) to operate like a single-mode fiber that only guides the fundamental mode. The fundamental mode produces the best beam quality at the output end of the fiber, and all HOMs produce reduced beam quality. Therefore, the following sections are going to focus on the LP<sub>01</sub> fundamental mode interacting with some other HOM. Also, this is what the observed TMI phenomenon does in high-power fiber laser amplifiers. The artificial LPBG is a controlled theoretical and numerical test that will explore the conditions for coupling. Section 7.2 attempts to derive analytical expressions for power in a simpler system with only two propagating modes.

## 7.2 An autonomous system for Power

We begin our discussion by writing down the coupled ODE (2.54) for step-index fibers:

$$\frac{dA_l^\ell}{dz} = \sum_{m=1}^{M_\ell} e^{i(\beta_m^\ell - \beta_l^\ell)z} K_{lm}^\ell A_m^\ell, \quad \text{for } 0 < z < L, \quad (7.1a)$$

$$\text{where } K_{lm}^\ell = \int_{\Omega_z} \text{Pol} \phi_m^\ell \phi_l^\ell dx dy. \quad (7.1b)$$

Next, we consider a simplified system where we propagate only one laser wavelength (hence ignoring the super-script  $\ell$ ) consisting of two guided core modes ( $M_s = 2$ ). We ignore gain as it has no contribution towards the mode coupling effect that is being investigated. By ignoring the active gain, the Raman gain, and all forms of loss along the fiber from the term "Pol" in equation (7.1b), we ensure that the total laser power ought to be

conserved as it propagates along the fiber length. Finally, we prevent our computational LPBG to have a time dependence. For example, we consider a LPBG of the following form

$$\Pi(z) = \delta n_0 \sin(\Lambda_1 \Delta \beta z).$$

Ideally, to better match the TMI phenomenon one should consider a time dependent grating but since our goal is to come up with analytical expressions for power when the coupling is non-chaotic, we ignore the time dependence. In real fibers the fabricated FBGs and/or natural LPBGs of TMI tend to have refractive index fluctuations that are more within about  $10^{-5}$  to  $10^{-3}$ . So, we fix  $\delta n_0 = 10^{-4}$ . Also, we assume that the modes are real valued. Also, at  $z = 0$ , mode 1 contains all the power (say  $P_{\text{total}}$ ), i.e.  $P_1(z = 0) = P_{\text{total}}$ , and  $P_2(z = 0) = 0$  where subscripts are denoting the mode indices. Finally, we approximate  $\beta_1$ , and  $\beta_2$  by  $\beta_{\text{avg}}$  where  $\beta_{\text{avg}} = \frac{\beta_1 + \beta_2}{2}$ . Hence, we redefine  $K_{lm}$  for  $l, m \in \{1, 2\}$  as follows,

$$\begin{aligned} K_{lm} &= \int_{\Omega_z} \frac{ik^2}{\beta_{\text{avg}}} \Pi(z) n(x, y) \varphi_m(x, y) \overline{\varphi_l(x, y)} dx dy, \\ &= i \Im(K_{lm}). \end{aligned}$$

$$\text{Therefore, } K_{lm}, = iC_1 \sin(\Lambda_1 \Delta \beta z) \quad \text{when } l \neq m, \quad (7.2a)$$

$$\text{and } K_{lm}, = 0 \quad \text{when } l = m, \quad (7.2b)$$

where  $C_1 = \Im(K_{lm}) = \int_{\Omega_z} \frac{k^2 \delta n_0}{\beta_{\text{avg}}} n(x, y) \varphi_m(x, y) \overline{\varphi_l(x, y)} dx dy \approx \mathcal{O}(10^{-5})$  is a constant.

We also have the following properties as our coupling term is a purely imaginary number.

$$K_{lm}^* = -K_{lm}, \quad \forall l, m,$$

$$K_{lm} = K_{ml}, \quad \forall l, m.$$

For the newly defined system we rewrite the CMT-amplitude equation as follows:

$$\frac{dA_1}{dz} = K_{11}A_1 + e^{i(\beta_2 - \beta_1)z} K_{12}A_2, \quad (7.3a)$$

$$\frac{dA_2}{dz} = e^{i(\beta_1 - \beta_2)z} K_{21}A_1 + K_{22}A_2. \quad (7.3b)$$

The power carried by a particular mode can be defined as,

$$\begin{aligned} P_l &= \frac{1}{\mu_0 c} |A_l|^2 \int_{\Omega_z} n(x, y) \varphi_l^2, \\ &= \frac{1}{\mu_0 c} A_l A_l^* \int_{\Omega_z} n(x, y) \varphi_l^2. \end{aligned} \quad (7.4)$$

Differentiating the power carried by the  $l^{\text{th}}$  mode with respect to  $z$  we get,

$$\begin{aligned}
\frac{dP_l}{dz} &= \frac{1}{\mu_0 c} \int_{\Omega_z} n(x,y) \phi_l^2 \left[ A_l \left( \frac{dA_l}{dz} \right)^* + A_l^* \left( \frac{dA_l}{dz} \right) \right], \\
&= \frac{1}{\mu_0 c} \int_{\Omega_z} n(x,y) \phi_l^2 \left[ A_l \left( \sum_{m=1}^2 e^{-i(\beta_m - \beta_l)z} K_{lm}^* A_m^* \right) + A_l^* \left( \sum_{m=1}^2 e^{i(\beta_m - \beta_l)z} K_{lm} A_m \right) \right], \\
&= \frac{1}{\mu_0 c} \int_{\Omega_z} n(x,y) \phi_l^2 \left[ \sum_{m=1}^2 \Im(K_{lm}) (\mathbf{a}_m a_l^* + \mathbf{a}_m^* a_l) \right], \\
&\quad \left( \text{where, } a_l = A_l e^{i\beta_l z} \text{ and } \mathbf{a}_l = i a_l, \forall l \right), \\
&= \frac{1}{\mu_0 c} \int_{\Omega_z} n(x,y) \phi_l^2 \left[ \sum_{m=1}^2 \Im(K_{lm}) (|\mathbf{a}_m|^2 - |a_l|^2) \right] \tag{7.5} \\
&\quad + \frac{1}{\mu_0 c} \int_{\Omega_z} n(x,y) \phi_l^2 \sum_{m=1}^2 \Im(K_{lm}) \left[ (\mathbf{a}_m a_l^* - \mathbf{a}_m \mathbf{a}_m^* + \mathbf{a}_m^* a_l^* + a_l a_l^*) \right], \\
&= \sum_{m=1}^2 \Im(K_{lm}) \left[ \frac{\int_{\Omega_z} n(x,y) \phi_l^2}{\int_{\Omega_z} n(x,y) \phi_m^2} P_m - P_l \right] + \eta_l(z), \quad \left( |a_l|^2 = |a_l|^2 = |A_l|^2, \forall l \right), \\
&= \sum_{m=1}^2 \Im(K_{lm}) \left[ \mathbb{I}_{lm} P_m - P_l \right] + \eta_l(z), \quad \left( \text{where, } \mathbb{I}_{lm} = \frac{\int_{\Omega_z} n(x,y) \phi_l^2}{\int_{\Omega_z} n(x,y) \phi_m^2} \right),
\end{aligned}$$

where  $\eta_l$  is defined as  $\eta_l = \frac{1}{\mu_0 c} \int_{\Omega_z} n(x,y) \phi_l^2 \sum_{m=1}^2 \Im(K_{lm}) \left[ (\mathbf{a}_m a_l^* - \mathbf{a}_m \mathbf{a}_m^* + \mathbf{a}_m^* a_l^* + a_l a_l^*) \right]$ .

Finally, we write the system explicitly for the two modes as:

$$\frac{dP_1}{dz} = \Im(K_{12}) \left[ \mathbb{I}_{12} P_2 - P_1 \right] + \eta_1, \tag{7.6a}$$

$$\frac{dP_2}{dz} = \Im(K_{21}) \left[ \mathbb{I}_{21} P_1 - P_2 \right] + \eta_2. \tag{7.6b}$$



If  $\eta_l$  is very small for all  $l \in \{1, 2\}$ , we may neglect them which results in an **autonomous system** for power. Also, mode power exchange can be interpreted using the equations (7.6a), and (7.6b). Imagine at some point (say at  $z = z_1$ ) in the fiber, mode 1 contains all the power. i.e.  $P_1(z_1) = P_{\text{total}}$  and  $P_2(z_1) = 0$ . Then equations (7.6a), and (7.6b) at  $z = z_1$  can be written as,

$$\frac{dP_1}{dz} = -\Im\mathfrak{m}(K_{12})P_1 + \eta_1(z) \quad (7.7a)$$

$$\frac{dP_2}{dz} = \Im\mathfrak{m}(K_{21})\mathbb{I}_{21}P_1 + \eta_2(z) \quad (7.7b)$$

Equation (7.7a) shows that mode 1 will lose power and (7.7b) shows that mode 2 will gain power through the coupling term. In fact, all the power gets exchanged between the modes if the coupling is 100% efficient. As we recall,  $\mathbb{I}_{lm} = \frac{\int_{\Omega_z} n(x, y) \phi_l^2}{\int_{\Omega_z} n(x, y) \phi_m^2}$ , approximating  $\mathbb{I}_{12} \approx 1$  and  $\mathbb{I}_{21} \approx 1$  we write (7.6a), and (7.6b) in the following manner:

$$\frac{d\mathbf{P}}{dz} = \Im\mathfrak{m}(K_{12})\mathbf{B} \cdot \mathbf{P} + \boldsymbol{\eta} \quad (7.8)$$

where,  $\mathbf{P} = \begin{bmatrix} P_1 \\ P_2 \end{bmatrix}$ ,  $\mathbf{B} = \begin{bmatrix} -1 & 1 \\ 1 & -1 \end{bmatrix}$  and  $\boldsymbol{\eta} = \begin{bmatrix} \eta_1 \\ \eta_2 \end{bmatrix}$ .

Now,  $\mathbf{B}$  is a real symmetric matrix and hence diagonalizable. Upon diagonalization we get

$$\mathbf{B} = \mathbf{U}^T \mathbf{D} \mathbf{U},$$

where,  $\mathbf{U} = \begin{bmatrix} 1/\sqrt{2} & 1/\sqrt{2} \\ -1/\sqrt{2} & 1/\sqrt{2} \end{bmatrix}$  and  $\mathbf{D} = \begin{bmatrix} 0 & 0 \\ 0 & -2 \end{bmatrix}$ . Let,  $\mathbf{W} = \mathbf{U} \cdot \mathbf{P} = \frac{1}{\sqrt{2}} \begin{bmatrix} P_2(z) + P_1(z) \\ P_2(z) - P_1(z) \end{bmatrix}$ .

Therefore we rewrite (7.8) as,

$$\frac{d \mathbf{W}}{dz} = \Im(K_{12}) \mathbf{D} \cdot \mathbf{W} + \mathbf{U} \cdot \boldsymbol{\eta} \quad (7.9)$$

i.e.

$$\frac{d W_1}{dz} = [\mathbf{U} \cdot \boldsymbol{\eta}]_1 \quad (7.10a)$$

$$\frac{d W_2}{dz} = -2\Im(K_{12})W_2 + [\mathbf{U} \cdot \boldsymbol{\eta}]_2 \quad (7.10b)$$

i.e.

$$\frac{d W_1}{dz} = [\eta_2(z) + \eta_1(z)] \quad (7.11a)$$

$$\frac{d W_2}{dz} = -2C_1 \sin(\Lambda_1 \Delta \beta z) W_2 + [\eta_2(z) - \eta_1(z)] \quad (7.11b)$$

The solution to the above system of equations can be written as follows:

$$\mathbf{W} = \mathbf{F} \cdot \mathbf{W}(z=0) + \mathbf{F} \cdot \int_0^z \mathbf{U} \cdot \boldsymbol{\eta} \quad (7.12)$$

where,

$$\mathbf{F}(z) = \begin{bmatrix} 1 & 0 \\ 0 & e^{\xi(z)} \end{bmatrix}, \text{ and } \xi(z) = \frac{2C_1}{\Lambda_1 \Delta \beta} \cos(\Lambda_1 \Delta \beta z).$$

Hence,

$$\mathbf{P} = (\mathbf{U}^T \mathbf{F}) \cdot \mathbf{W}(\mathbf{0}) + (\mathbf{U}^T \mathbf{F}) \cdot \int_0^z \mathbf{U} \cdot \boldsymbol{\eta} \quad (7.13)$$

From (7.13) we get,

$$P_1(z) = \frac{1}{2}P_{\text{total}}(1 + e^{\xi}) + \int_0^z [\mathbf{U} \cdot \boldsymbol{\eta}]_1 - e^{\xi} \int_0^z [\mathbf{U} \cdot \boldsymbol{\eta}]_2 \quad (7.14a)$$

$$P_2(z) = \frac{1}{2}P_{\text{total}}(1 - e^{\xi}) + \int_0^z [\mathbf{U} \cdot \boldsymbol{\eta}]_1 + e^{\xi} \int_0^z [\mathbf{U} \cdot \boldsymbol{\eta}]_2 \quad (7.14b)$$

Since,  $P_1 + P_2 = P_{\text{total}}$ , we have  $\int_0^z [\mathbf{U} \cdot \boldsymbol{\eta}]_1 = 0$ . Finally, the powers of the two modes can be written as,

$$P_1(z) = \frac{1}{2}P_{\text{total}}(1 + e^{\xi}) - e^{\xi} \int_0^z [\eta_2(z) - \eta_1(z)] dz \quad (7.15a)$$

$$P_2(z) = \frac{1}{2}P_{\text{total}}(1 - e^{\xi}) + e^{\xi} \int_0^z [\eta_2(z) - \eta_1(z)] dz \quad (7.15b)$$

Next, we rewrite the power solutions in equation (7.15) as follows:

$$P_1(z) = \frac{1}{2}P_{\text{total}} + e^{\xi} h(z) \quad (7.16a)$$

$$P_2(z) = \frac{1}{2}P_{\text{total}} - e^{\xi} h(z) \quad (7.16b)$$

where,  $h(z) = \frac{1}{2}P_{\text{total}} - \int_0^z (\eta_2 - \eta_1)$  and  $\eta_l = \frac{1}{\mu_0 c \Omega_z} \int n(x, y) \phi_l^2 \sum_{m=1}^2 \Im \mathbf{m}(K_{lm}) \left[ (\mathbf{a}_m a_l^* - \mathbf{a}_m \mathbf{a}_m^* + \mathbf{a}_m^* a_l^* + a_l a_l^*) \right]$ . Next, let us look at the function

$$f(z) = P_1(z) - P_2(z) = 2e^{\xi} h(z), \text{ where } \xi(z) = \frac{2C_1}{\Lambda_1 \Delta \beta} \cos(\Lambda_1 \Delta \beta z).$$

We have  $\max(f) \leq P_{\text{total}}$  and  $\min(f) \geq -P_{\text{total}}$ . Now,

$$\frac{df(z)}{dz} = 2 \left( e^{\xi} \frac{d\xi}{dz} h(z) + e^{\xi} \frac{dh(z)}{dz} \right).$$

Clearly, at  $z_j = \frac{\pi j}{\Lambda_1 \Delta \beta}$ ,  $\xi(z_j) = 0$  for all  $j = 1, 2, \dots$ . Therefore, the difference between the two mode powers at these specific longitudinal points are given by

$$f(z_j) = e^{(-1)^j \frac{2C_1}{\Lambda_1 \Delta \beta}} \left[ P_{\text{total}} - \int_0^{\frac{\pi j}{\Lambda_1 \Delta \beta}} (\eta_2 - \eta_1) \right]$$

If  $\mathcal{O}(\Lambda_1) = 1$  we have  $e^{(-1)^j \frac{2C_1}{\Lambda_1 \Delta \beta}} \approx 1$ , as  $C_1 \approx \mathcal{O}(10^{-5})$  and  $f(z_j) \approx P_{\text{total}} - \int_0^{\frac{\pi j}{\Lambda_1 \Delta \beta}} (\eta_2 - \eta_1)$ .

The  $\eta$ s are the power in the cross-mode terms, and one ought to expect them to be small in real optical fibers. Hence, Assuming  $\eta_1$  and  $\eta_2$  are very small, we may say the integral  $\int_0^z (\eta_2 - \eta_1)$  is also small. Therefore we can argue that (as it can be derived that the second order derivative of  $f$  at those  $z_j$  points is also 0)  $z_j$ 's are all critical points of  $f$  and consequently  $f$ ,  $P_1$  and  $P_2$  are periodic with period  $\frac{\pi j}{\Lambda_1 \Delta \beta}$  (may not be shortest). In the next section I consider a simplified system with no active gain and a suitable sinusoidal perturbation to the fiber refractive index to theoretically predict the results we have from LPBG theory.

### 7.3 Simulation Results

This section now numerically simulates a fiber waveguide with the artificial LPBG throughout the fiber:  $\Pi(z, t)$ , described in the previous section. Sometimes the active gain is re-introduced, just to demonstrate that it doesn't really affect the mode coupling. In this section simulations are done using the scalar CMT model 2.54 over a 0.5 m long Yb-doped fiber that is actually manufactured by a business called Nufern unless stated otherwise. At the beginning of the fiber we seed all the power in the fundamental mode. We simulate two cases using Yb-doped Nufern fiber whose specs are given in Table 4.1, in both cases we use the Bragg grating function (7.2a) as a perturbation to the refractive index. Loss and Raman

gain are not considered in these simulations. The fiber cross-section is non-dimensionalized by scaling by the fiber cladding radius. i.e. in the non-dimensionalized geometry, fiber cladding radius is 1 and the fiber core radius is 1/16. In the first case, the perturbation to the refractive index profile is radially symmetric. Also  $\Delta\beta = (\beta_1 - \beta_2)$ . Consequently in table 7.1 we can clearly see coupling between modes  $LP_{01}$  and  $LP_{02}$ . Other modes remained unaltered. In the second case the refractive index is perturbed asymmetrically. Here we only perturbed a circular region in the fiber core, given by  $(x - \frac{1}{32})^2 + (y - \frac{1}{32})^2 = (\frac{1}{48})^2$ . Table 7.2 shows results in the asymmetric case. Here we fixed  $\Delta\beta = (\beta_{01} - \beta_{11})$  to get coupling between  $LP_{01}$  and two independent  $LP_{11}$  modes that are effectively a rotation of the other, and will be labeled  $LP_{11a}$  and  $LP_{11b}$  modes. We do the same thing for  $LP_{21}$  modes. In the case where we have included gain in the simulation, we do see amplification in mode power levels.

As expected, the gain does not directly affect the mode coupling in terms of its periodicity (meaning rate of coupling) nor its direction of coupling. Even though it appears that each mode is growing (being amplified) at the same rate, this is not exactly true. Their rate of growth/amplification depends on their overlap with the gain region, which is slightly different for different LP modes (though is the same for different orientations/rotations of the same LP mode). To further investigate, in the following section I experiment with different grating functions ( $\Pi$ ), employed to different grating regions.

#### **7.4 Experiments with different grating functions and perturbation regions**

In this section we will continue exploring different grating functions and perturbation regions, but with some new objectives in mind. When TMI occurs, we observe chaotic power transfer between modes. If we can find a grating which stabilizes an ongoing TMI then that

Table 7.1: Mode coupling due to symmetric perturbation

Description	Figure
Including gain	
Without gain	

Table 7.2: Mode coupling due to asymmetric perturbation

Description	Figure
Including gain	<p style="text-align: center;">Power in each mode</p>
Without gain	<p style="text-align: center;">Power in each mode</p>

may serve an alternative solution to prevent the instability. In other words, if the fiber amplifier was already chaotically exchanging energy between its guided modes (e.g., the TMI), then we would like to design an artificial grating that forces HOM energy back into the FM to the greatest extent possible. Hence, we are looking for cases with the property that, irrespective of the position in the fiber, the grating would always cause the fundamental mode to gain power and never lose power. Consequently, all the higher order modes should lose power irrespective of the position in the fiber and never gain power.

We have already seen that it is possible to exchange power between any particular two modes by tweaking  $\Delta\beta$  in the grating function and varying the perturbation region. Here, instead of any two modes we want all of the higher order modes to send its power to the fundamental mode. We start by considering the following function,

$$\Pi(z,t) = \delta n_0 \sum_j a_j \sin(\Delta_j \beta z)$$

where  $\Delta_j \beta$  is the  $j^{th}$   $\Delta\beta$  from the set of all  $\Delta\beta$ s. For different perturbation regions, we varied the coefficients  $a_j$  from 0-10 with 10 data-points. We then reduce the range 0-10 and increase data points, for example 100 data points in the range 0-1, depending on the output. The code is also checking the following,

- Recognize the cases where the final fundamental mode power yield is maximum.
- At which z-point (smallest) the fundamental mode reaches its maximum power. This will be useful to optimize the perturbed fiber length.

In order to satisfy all the properties stated above, for different perturbation regions, the optimized coefficients of the sine functions won't be the same. We have presented results that are closest to our requirement. The code discards a possible grating if any of the above



stated properties is not satisfied. In each simulation the program considers two initial power distributions. In one case the power is equally distributed among all the modes, while in the other case FM contains 60% of the total power and the rest of the power is equally distributed among the rest of the modes. Since the TMI process is a chaotic process, to serve our purpose, we need a grating that satisfies all the above stated properties for any initial conditions. The other parameters are same as in Table 4.1. Following are the three examples of gratings from our simulation output, which are the closest to what we are looking for.

**Annulus:** This is the first output from our fiber amplifier model satisfying the requirements stated in the previous sections. The grating region is an annulus. Following are the description of the grating region as well as the grating function:

- Center:  $(0.5r_{\text{core}}, 0.2r_{\text{core}})$ ; Inner radius:  $0.97r_{\text{core}}$ .
- Region:  $\sqrt{(x - 0.5r_{\text{core}})^2 + (y - 0.2r_{\text{core}})^2} > 0.97r_{\text{core}}$
- Grating Function:

$$\begin{aligned} \Pi(z, t) = & \delta n_0 \left( 0.05 \sin(\Delta\beta_{01,11_a} z) + 0.42 \sin(\Delta\beta_{01,11_b} z) \right. \\ & \left. + 0.14 \sin(\Delta\beta_{01,21_a} z) + 6.09 \sin(\Delta\beta_{01,21_b} z) + 2.23 \sin(\Delta\beta_{01,02} z) \right) \end{aligned}$$

The subscript of the  $\Delta\beta$  shows the LP subscripts of the chosen modes. We observed that the value of  $\delta n_0$  can also be optimized by measuring the maximum power achieved by the fundamental mode in a single simulation, keeping the other initial conditions same. Table 7.3 refers to a small part of the data where  $P_{\text{FM}}$  reaches its maximum value for various  $\delta n_0$  values. We set  $\delta n_0 = 1.82 \cdot 10^{-4}$ . Table 7.4 showing

$\delta n_0 \cdot 10^4$	$\max(P_{\text{FM}})[\text{W}]$
1.78	17.3736
1.79	17.3783
1.80	17.3818
1.81	17.3839
<b>1.82</b>	<b>17.3848</b>
1.83	17.3844
1.84	17.3827
1.85	17.3797
1.86	17.3755

Table 7.3: The change in FM output power is shown as the value of  $\delta n_0$  changes, the grating region here is an annulus

Input FM seed([W])	$\max(P_{\text{FM}})[\text{W}]$	Distance into the fiber [mm]
0	13.2406	0.5567
20%	17.5247	0.4709
40%	18.9736	0.3472
60%	20.7403	0.2793
80%	22.7284	0.2135

Table 7.4: The table shows at what distance the fundamental mode reaches its maximum power as we change the initial input seed power injected in the FM, the grating region here is an annulus

for different FM mode initial seed power, at which point of the fiber  $\max(P_{\text{FM}})$  is reached. Here 1 mode beat length =  $\frac{2\pi}{\Delta\beta_{01,02}} \approx 1.1876$  mm.

**Ellipse<sup>c</sup>:** Here **Ellipse<sup>c</sup>** denotes the complement of an elliptic region inside the fibercore. The details of the ellipse and the grating function is following:

- Center:  $(0.5r_{\text{core}}, 0.21r_{\text{core}})$ ; major axis:  $0.95r_{\text{core}}$ ; minor axis:  $1.1r_{\text{core}}$
- Region:  $\frac{(x - 0.5r_{\text{core}})^2}{(0.95r_{\text{core}})^2} + \frac{(y - 0.2r_{\text{core}})^2}{(1.1r_{\text{core}})^2} > 1$

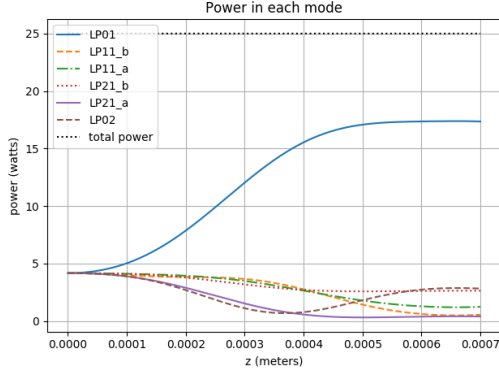


Figure 7.1: Initial seed equally distributed.

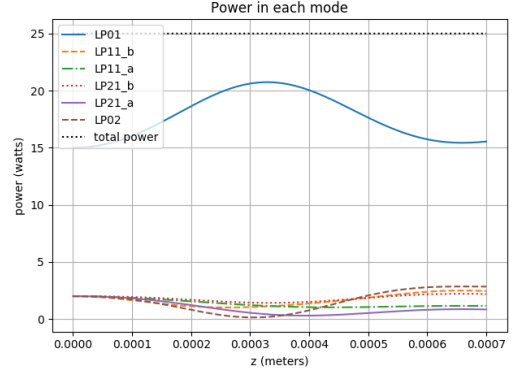


Figure 7.2: FM receives 60% of the seed power.

- Grating Function:

$$\begin{aligned} \Pi(z, t) = & \delta n_0 \left( 0.01 \sin(\Delta\beta_{11_b, 21_b} z) + 0.1 \sin(\Delta\beta_{11_a, 21_b} z) \right. \\ & \left. + 0.05 \sin(\Delta\beta_{01, 21_a} z) + 6.09 \sin(\Delta\beta_{01, 21_b} z) + 2.23 \sin(\Delta\beta_{01, 02} z) \right) \end{aligned}$$

Table 7.5 refers to a small part of the data where  $P_{FM}$  reaches its maximum value for various  $\delta n_0$  values. We set  $\delta n_0 = 1.97e - 4$ . Table 7.6 showing for different FM mode initial seed power, at which point of the fiber  $\max(P_{FM})$  is reached. Here 1 mode beat length =  $\frac{2\pi}{\Delta\beta_{01,02}} = 1.1876$  mm.

**Hyperbola<sup>c</sup>:** Here **Hyperbola<sup>c</sup>** denotes the complement of an hyperbolic region inside the fiber-core. The details of the hyperbola and the grating function is following:

- Center:  $(0.61r_{core}, 0.2r_{core})$ ; major axis:  $0.7r_{core}$ ; minor axis:  $5.8r_{core}$
- Region:  $\frac{(x - 0.61r_{core})^2}{(0.7r_{core})^2} - \frac{(y - 0.2r_{core})^2}{(5.8r_{core})^2} > 1$

$\delta n_0 * 10^4$	$max(P_{FM})W$
1.92	17.8372
1.93	17.8377
1.94	17.8381
1.95	17.8383
1.96	17.8384
<b>1.97</b>	<b>17.8385</b>
1.98	17.8384
1.99	17.8381
2.00	17.8378
2.01	17.8374
2.02	17.8369

Table 7.5: The change in FM output power is shown as the value of  $\delta n_0$  changes, the grating region here is the complement of an elliptic region inside the fibercore

input FM seed(W)	$max(P_{FM})W$	reached at(mode beat lengths)
0	14.1872	0.5507
20%	17.8385	0.4250
40%	19.3482	0.3332
60%	21.0556	0.2714
80%	22.9142	0.2115

Table 7.6: The table shows at what distance the fundamental mode reaches its maximum power as we change the initial input seed power injected in the FM, the grating region here is the complement of an elliptic region inside the fibercore

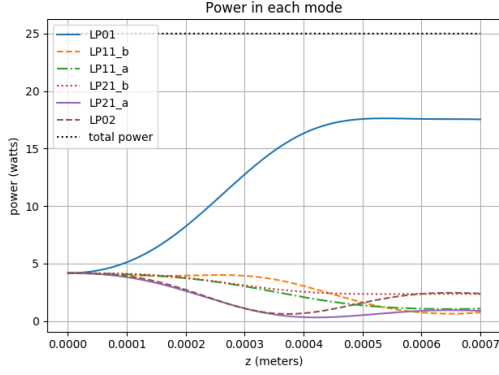


Figure 7.3: Initial seed equally distributed.

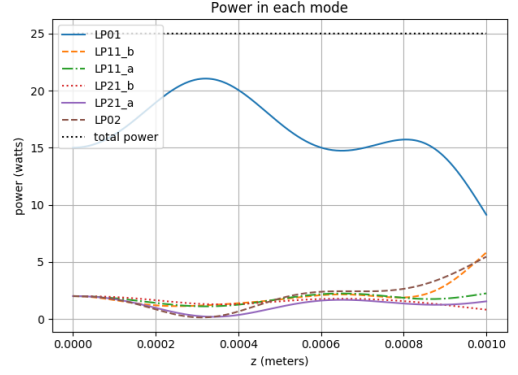


Figure 7.4: FM receives 60% of the seed power.

input FM seed(W)	$\max(P_{FM})W$	reached at(mode beat lengths)
0	15.8351	0.6385
20%	15.0481	0.3073
40%	15.8729	0.2374
60%	18.2025	0.1796
80%	21.3813	0.1317

Table 7.7: The table shows at what distance the fundamental mode reaches its maximum power as we change the initial input seed power injected in the FM, the grating region here is the complement of a hyperbolic region inside the fibercore

- Grating Function:

$$\begin{aligned} \Pi(z, t) = & \delta n_0 \left( 0.2 \sin(\Delta\beta_{11_b, 21_b} z) + 0.1 \sin(\Delta\beta_{11_a, 21_b} z) \right. \\ & \left. + 0.1 \sin(\Delta\beta_{01, 21_a} z) + 2.5 \sin(\Delta\beta_{01, 21_b} z) + 7.8 \sin(\Delta\beta_{01, 02} z) \right) \end{aligned}$$

We optimize the output FM power with  $\delta n_0$  in similar fashion and we set  $2.05 \cdot 10^{-4}$ .

where 1 mode beat length =  $\frac{2\pi}{\Delta\beta_{01,02}} = 1.1876$  mm.

As a conclusion, I say that even if the main purpose of this chapter is to numerically come up with a grating that has the potential to convert the chaotic TMI process into a

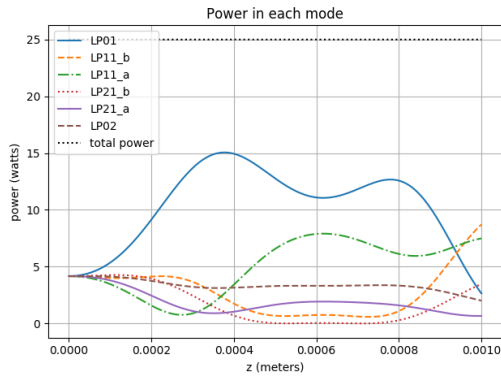


Figure 7.5: Initial seed equally distributed.

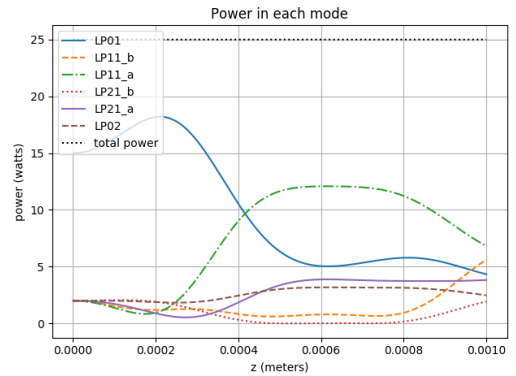


Figure 7.6: FM receives 60% of the seed power.

steady FM beam, the experiments did not give good approximations for the required grating. However, results from section 7.4 do show a lot of promise. Figures 7.1 through 7.6 show mode-wise the power profiles along the longitudinal length of the fiber, for two different initial seed conditions and for the three grating regions received from the simulation after initial optimizations. The chapter can serve as the initial work of a potential future project where it gives researchers opportunity to take this work further.

## Chapter 8

### Conclusion

Following are the conclusions that we draw:

- From chapter 4 we conclude that for power-level computations equivalent fibers are good candidates. Also, Figure 4.4 clearly indicates that excessively short equivalent fiber lengths are not recommendable. TMI. However, more research is needed in this area.
- In chapter 5 we show the onset of TMI and various relative modal instability power thresholds under different scenarios.
- In chapter 6 the numerical simulation effort provides important quantification of the complex performance trade-space for high-power continuous-wave Tm-doped fiber laser amplifiers operating in the 2.1-2.2  $\mu\text{m}$  wavelength regime. Our studies have included the effects of changing the total dopant concentration in the amplifier, the seeding conditions (including both the total seed power and tone-to-signal seed ratios), the amplifier configuration (single- or two-tone), the magnitude of the bulk Raman gain coefficient, the coil of the fiber (straight or circularly bent), and the signal wavelength. These important amplifier characteristics include the anticipated

amplifier lengths of 95% pump absorption, the guided core mode-bend-losses under different thermal loads, the signal amplification efficiencies, the signal output powers, the expected conditions for the onset of ASE and the onset of the TMI (chapter 5), and the predicted maximum temperatures throughout the fiber.

- Finally, Chapter 7 derives an autonomous system of power for a simplified fiber amplifier system. Through experiments we also conclude that it is possible to construct a grating that has the capability to mitigate

All of these calculations are done under somewhat idealized conditions, but are indicative of what can be anticipated in real amplifiers. Our results provide relative magnitudes and trends that allow other researchers to identify potentially important parameter ranges to quantify their amplifier performance under various configurations.

## **8.1 Future work**

As this dissertation attempts to answer many question regarding fiber amplifier research, there are still many unanswered question that has the potential to extend the work in this dissertation. Following are a few pointers:

1. Throughout the dissertation we have used a straight fiber modes. In the field of fiber amplifier, bent fibers are of particular interest as these fibers are mostly used in environments where its surrounded in a spool of a particular radius. So, as a next step we can try to compute the bent modes in a step-index fiber and do the propagation studies.
2. Also, in this dissertation we use a step-index fiber. Although, other types of fibers, for example hollow-core fibers or microstructure fibers are also extremely important



and has many applications. Here, we can try to compute the modes in those fiber geometry (with or without bending) and do the propagation studies.

3. Finally for tmi mitigation chapter 7 provides potential solutions in terms of artificial refractive index grating applied to specific regions in the core. The solutions look promising but not applicable. More research in this area can crack the root cause behind TMI.

## References

- [1] S. D. AGGER AND J. H. POVLSEN, *Emission and absorption cross section of thulium doped silica fibers*, Optics Express, 14 (2006), pp. 50–57.
- [2] G. P. AGRAWAL, *Nonlinear Fiber Optics*, Academic Press (Elsevier), The Boulevard, Langford Lane, Kidlington, Oxford OX5 1GB, UK, fifth ed., 2013.
- [3] G. M. AMDAHL, *Validity of the single processor approach to achieving large scale computing capabilities*, in Proceedings of the April 18-20, 1967, Spring Joint Computer Conference, AFIPS '67 (Spring), New York, NY, USA, 1967, Association for Computing Machinery, p. 483–485.
- [4] B. ANDERSON, A. FLORES, J. GROSEK, AND I. DAJANI, *High power tm-doped all-fiber amplifier at 2130 nm*, in CLEO: Science and Innovations, Optical Society of America, 2017, pp. SM1L–3.
- [5] O. ANTIPOV, M. KUZNETSOV, D. ALEKSEEV, AND V. TYRTYSHNYY, *Influence of a backward reflection on low-threshold mode instability in  $yb^{3+}$ -doped few-mode fiber amplifiers*, Optics Express, 24 (2016), pp. 14871–14879.
- [6] A. BERK, P. CONFORTI, AND F. HAWES, *An accelerated line-by-line option for modtran combining on-the-fly generation of line center absorption within 0.1 cm-1 bins and pre-computed line tails*, in Algorithms and Technologies for Multispectral,

Hyperspectral, and Ultraspectral Imagery XXI, vol. 9472, International Society for Optics and Photonics, 2015, p. 947217.

- [7] A. BERK, P. CONFORTI, R. KENNETT, T. PERKINS, F. HAWES, AND J. VAN DEN BOSCH, *Modtran® 6: A major upgrade of the modtran® radiative transfer code*, in 2014 6th Workshop on Hyperspectral Image and Signal Processing: Evolution in Remote Sensing (WHISPERS), IEEE, 2014, pp. 1–4.
- [8] T. E. O. E. BRITANNICA, *Electric susceptibility*. <https://www.britannica.com/science/electric-susceptibility>, October 2016.
- [9] F. CARDARELLI, *Materials handbook*, Springer, 2018.
- [10] J. CHESNOY, *EDFA Blooming: the fall of the barricades*, Submarine Telecoms Forum, 102 (2018), pp. 50–55.
- [11] I. DAJANI, C. ZERINGUE, T. J. BRONDER, T. SHAY, A. GAVRIELIDES, AND C. ROBIN, *A theoretical treatment of two approaches to sbs mitigation with two-tone amplification*, Optics Express, 16 (2008), pp. 14233–14247.
- [12] V. DISTLER, F. MÖLLER, M. STRECKER, G. PALMA-VEGA, T. WALBAUM, AND T. SCHREIBER, *Transverse mode instability in a passive fiber induced by stimulated raman scattering*, Optics Express, 28 (2020), pp. 22819–22828.
- [13] D. DRAKE, J. GOPALAKRISHNAN, T. GOSWAMI, AND J. GROSEK, *Simulation of optical fiber amplifier gain using equivalent short fibers*, Computer Methods in Applied Mechanics and Engineering, 360 (2020), p. 112698.

- [14] T. EIDAM, S. HANF, E. SEISE, T. V. ANDERSEN, T. GABLER, C. WIRTH, T. SCHREIBER, J. LIMPert, AND A. TÜNNERMANN, *Femtosecond fiber cpa system emitting 830 w average output power*, Optics letters, 35 (2010), pp. 94–96.
- [15] T. EIDAM, C. WIRTH, C. JAUREGUI, F. STUTZKI, F. JANSEN, H. OTTO, O. SCHMIDT, T. SCHREIBER, J. LIMPert, AND A. TÜNNERMANN, *Experimental observations of the threshold-like onset of mode instabilities in high power fiber amplifiers*. optics express, 19(14):13218–13224, 2011., Optics Express, 19 (2011), pp. 13218–13224.
- [16] C. GAIDA, M. GEBHARDT, T. HEUERMANN, Z. WANG, F. STUTZKI, C. JAUREGUI, AND J. LIMPert, *Observation of transverse-mode instabilities in a thulium-doped fiber amplifier*, in Fiber Lasers XVI: Technology and Systems, vol. 10897, International Society for Optics and Photonics, 2019, p. 1089702.
- [17] J. GOPALAKRISHNAN, T. GOSWAMI, AND J. GROSEK, *Techniques for modeling fiber laser amplifiers*, in Scientific Computing in Electrical Engineering, G. Nicosia and V. Romano, eds., vol. 32 of Mathematics in Industry, Proceedings of The 12th International Conference on Scientific Computing in Electrical Engineering” ( SC EE), Taormina, Sicily, Italy, Springer, 2020, pp. 45–54.
- [18] J. GOPALAKRISHNAN, L. GRUBISIC, J. S. OVALL, AND B. PARKER, *Analysis of FEAST spectral approximations using the DPG discretization*, Comput. Methods Appl. Math., 19 (2019), pp. 251–266.
- [19] T. GOSWAMI, J. GROSEK, AND J. GOPALAKRISHNAN, *Simulations of single- and two-tone tm-doped optical fiber laser amplifiers*, Optics Express, 29 (2021), pp. 12599–12615.

- [20] G. GOULD, *Laser physics and principles*, Sataloff's Comprehensive Textbook of Otolaryngology: Head & Neck Surgery: Laryngology, 4 (2015), p. 429.
- [21] R. GOULD, *A coupled mode description of the backward-wave oscillator and the kempfner dip condition*, IRE Transactions on Electron Devices, 2 (1955), pp. 37–42.
- [22] J. GROSEK, *Coupled mode theory fiber amplifier model technical report*, February 2021.
- [23] J. GROSEK, S. NADERI, B. OLIKER, R. LANE, I. DAJANI, AND T. MADDEN, *Laser simulation at the air force research laboratory*, in XXI International Symposium on High Power Laser Systems and Applications, International Society for Optics and Photonics, 2017, p. 102540N.
- [24] J. L. GUSTAFSON, *Reevaluating amdahl's law*, Commun. ACM, 31 (1988), p. 532–533.
- [25] N. HAARLAMMERT, O. DE VRIES, A. LIEM, A. KLINER, T. PESCHEL, T. SCHREIBER, R. EBERHARDT, AND A. TÜNNERMANN, *Build up and decay of mode instability in a high power fiber amplifier*, Optics express, 20 (2012), pp. 13274–13283.
- [26] H. A. HAUS, *Electron beam waves in microwave tubes*, (1958).
- [27] S. HENNEKING, J. GROSEK, AND L. DEMKOWICZ, *Model and computational advancements to full vectorial maxwell model for studying fiber amplifiers*, Computers & Mathematics with Applications, 85 (2021), pp. 30–41.
- [28] S. S. INC., *Modtran® web app*. [http://modtran.spectral.com/modtran\\_home](http://modtran.spectral.com/modtran_home), 2020.

- [29] S. D. JACKSON, *Cross relaxation and energy transfer upconversion processes relevant to the functioning of  $2\mu\text{m}$   $\text{Tm}^{3+}$ -doped silica fibre lasers*, Optics Communications, 230 (2004), pp. 197–203.
- [30] S. D. JACKSON AND T. A. KING, *Theoretical modeling of  $\text{tm}$ -doped silica fiber lasers*, J. Lightwave Technol., 17 (1999), p. 948.
- [31] C. JAUREGUI, J. LIMPERT, AND A. TÜNNERMANN, *High-power fibre lasers*, Nature Photonics, 7 (2013), pp. 861–867.
- [32] C. JAUREGUI, H.-J. OTTO, F. STUTZKI, J. LIMPERT, AND A. TÜNNERMANN, *Simplified modelling the mode instability threshold of high power fiber amplifiers in the presence of photodarkening*, Optics Express, 23 (2015), pp. 20203–20218.
- [33] C. JAUREGUI, C. STIHLER, AND J. LIMPERT, *Transverse mode instability*, Advances in Optics and Photonics, 12 (2020), pp. 429–484.
- [34] C. JAUREGUI, C. STIHLER, AND J. LIMPERT, *Transverse mode instability*, Advances in Optics and Photonics, 12 (2020), pp. 429–484.
- [35] H. KOGELNIK, *2. theory of dielectric waveguides*, in Integrated optics, Springer, 1975, pp. 13–81.
- [36] J. A. KONG, *Electromagnetic Wave Theory*, EMW Publishing, 2008.
- [37] J. P. KOPLOW, D. A. KLINER, AND L. GOLDBERG, *Single-mode operation of a coiled multimode fiber amplifier*, Optics letters, 25 (2000), pp. 442–444.
- [38] D. MARCUSE, *Coupled mode theory of round optical fibers*, Bell System Technical Journal, 52 (1973), pp. 817–842.

- [39] B. MARY, *How fiber optics was invented*. <https://www.thoughtco.com/>, 2020.
- [40] T. S. MCCOMB, *Power scaling of large mode area Thulium fiber lasers in various spectral and temporal regimes*, PhD thesis, University of Central Florida, 2009.
- [41] R. J. MEARS, L. REEKIE, I. JAUNCEY, AND D. N. PAYNE, *Low-noise erbium-doped fibre amplifier operating at 1.54  $\mu\text{m}$* , *Electronics Letters*, 23 (1987), pp. 1026–1028.
- [42] S. MILLER, *Coupled wave theory and waveguide applications*, *Bell System Technical Journal*, 33 (1954), pp. 661–719.
- [43] J. MINELLY, W. BARNES, R. LAMING, P. MORKEL, J. TOWNSEND, S. GRUBB, AND D. PAYNE, *Diode-array pumping of  $\text{Er}^{3+}/\text{Yb}^{3+}$ -co-doped fiber lasers and amplifiers*, *IEEE Photonics Technology Letters*, 5 (1993), pp. 301–303.
- [44] F. MÖLLER, V. DISTLER, T. SCHREIBER, R. EBERHARDT, AND A. TÜNNERMANN, *Manipulating the heat load distribution by laser gain competition in tm-limited fiber amplifiers*, in *Fiber Lasers XVII: Technology and Systems*, vol. 11260, International Society for Optics and Photonics, 2020, p. 1126019.
- [45] N. NADERI, A. FLORES, B. ANDERSON, AND I. DAJANI, *Beam combinable, kilowatt, all-fiber amplifier based on phase-modulated laser gain competition*, *Optics Letters*, 41 (2016), pp. 3964–3967.
- [46] S. NADERI, I. DAJANI, J. GROSEK, AND T. MADDEN, *Theoretical and numerical treatment of modal instability in high-power core and cladding-pumped raman fiber amplifiers*, *Optics express*, 24 (2016), pp. 16550–16565.

- [47] S. NADERI, I. DAJANI, T. MADDEN, AND C. ROBIN, *Investigations of modal instabilities in fiber amplifiers through detailed numerical simulations*, Optics Express, 21 (2013), pp. 16111–16129.
- [48] S. NAGARAJ, J. GROSEK, S. PETRIDES, L. DEMKOWICZ, AND J. MORA, *A 3D DPG Maxwell Approach to Nonlinear Raman Gain in Fiber Laser Amplifiers*, Journal of Computational Physics: X, 2 (2019), p. 100002.
- [49] M. NAKAZAWA, Y. KIMURA, AND K. SUZUKI, *Efficient  $er_3+$ -doped optical fiber amplifier pumped by a 1.48  $\mu\text{m}$  ingaasp laser diode*, Applied physics letters, 54 (1989), pp. 295–297.
- [50] R. PASCHOTTA, *fiber amplifiers' in the encyclopedia of laser physics and technology*. wiley-vch, isbn 978-3-527-40828-3, (2008).
- [51] H. PASK, R. CARMAN, D. HANNA, A. TROPPER, C. MACKECHNIE, P. BARBER, AND J. DAWES, *Ytterbium-doped silica fiber lasers: versatile sources for the 1-1.2  $\mu\text{m}$  region*, IEEE Journal of Selected Topics in Quantum Electronics, 1 (1995), pp. 2–13.
- [52] J. R. PIERCE, *Coupling of modes of propagation*, Journal of Applied Physics, 25 (1954), pp. 179–183.
- [53] G. A. REIDER, *Photonics: An introduction*, Springer, Switzerland, 2016.
- [54] S. SCHELKUNOFF, *Conversion of maxwell's equations into generalized telegraphist's equations*, Bell System Technical Journal, 34 (1955), pp. 995–1043.



- [55] R. SCHERMER AND J. COLE, *Improved bend loss formula verified for optical fiber by simulation and experiment*, IEEE Journal of Quantum Electronics, 43 (2007), pp. 899–909.
- [56] J. SCHÖBERL, *NETGEN an advancing front 2D/3D-mesh generator based on abstract rules*, Computing & Visualization in Science, 1 (1997), pp. 41–52.
- [57] ———, *Ngsolve website*. <https://ngsolve.org/>, 2019.
- [58] N. SIMAKOV, A. HEMMING, W. A. CLARKSON, J. HAUB, AND A. CARTER, *A cladding-pumped, tunable holmium doped fiber laser*, Optics Express, 21 (2013), pp. 28415–28422.
- [59] A. V. SMITH AND J. J. SMITH, *Mode instability in high power fiber amplifiers*, Optics Express, 19 (2011), pp. 10180–10192.
- [60] A. V. SMITH AND J. J. SMITH, *Increasing mode instability thresholds of fiber amplifiers by gain saturation*, Optics express, 21 (2013), pp. 15168–15182.
- [61] ———, *Steady-periodic method for modeling mode instability in fiber amplifiers*, Optics express, 21 (2013), pp. 2606–2623.
- [62] ———, *Mode instability thresholds for tm-doped fiber amplifiers pumped at 790 nm*, Optics express, 24 (2016), pp. 975–992.
- [63] A. W. SNYDER, *Coupled-mode theory for optical fibers*, JOSA, 62 (1972), pp. 1267–1277.
- [64] J. VERDEYEN, *Laser Electronics*, Prentice Hall, New Jersey, 3rd ed., 1995.

- [65] B. M. WALSH AND N. P. BARNES, *Comparison of tm: Zblan and tm: silica fiber lasers; spectroscopy and tunable pulsed laser operation around 1.9  $\mu\text{m}$* , Applied Physics B, 78 (2004), pp. 325–333.
- [66] B. G. WARD, *Modeling of transient modal instability in fiber amplifiers*, Optics Express, 21 (2013), pp. 12053–12067.
- [67] P. WESSELS, P. ADEL, M. AUERBACH, D. WANDT, AND C. FALLNICH, *Novel suppression scheme for brillouin scattering*, Optics Express, 12 (2004), pp. 4443–4448.
- [68] A. YARIV, *Coupled-mode theory for guided-wave optics*, IEEE Journal of Quantum Electronics, 9 (1973), pp. 919–933.
- [69] C. ZERINGUE, I. DAJANI, C. LU, A. LOBAD, AND C. VERGIEN, *Experimental verification of two-tone amplification in single frequency fiber amplifiers*, in Nonlinear Optics: Materials, Fund. and App., OSA, 2009, p. PDPA2.